EXPERIMENTAL INVESTIGATION OF FAILURE MECHANISM IN
CROSS-PLY AND FABRIC CURVED COMPOSITE LAMINATES

A THESIS SUBMITTED TO
THE GRADUATE SCHOOL OF NATURAL AND APPLIED SCIENCES
OF
MIDDLE EAST TECHNICAL UNIVERSITY

BY

AHMET ÇEVİK

IN PARTIAL FULFILLMENT OF THE REQUIREMENTS
FOR
THE DEGREE OF MASTER OF SCIENCE
IN
AEROSPACE ENGINEERING

AUGUST 2021

Approval of the thesis:

EXPERIMENTAL INVESTIGATION OF FAILURE MECHANISM IN CROSS-PLY AND FABRIC CURVED COMPOSITE LAMINATES

submitted by **AHMET ÇEVİK** in partial fulfillment of the requirements for the degree of **Master of Science** in **Aerospace Engineering, Middle East Technical University** by,

Prof. Dr. Halil Kalıpçılar
Dean, Graduate School of **Natural and Applied Sciences**   _____

Prof. Dr. İsmail Hakkı Tuncer
Head of the Department, **Aerospace Engineering**   _____

Prof. Dr. Demirkan Çöker
Supervisor, **Aerospace Engineering, METU**   _____

Examining Committee Members:

Prof. Dr. Altan Kayran
Aerospace Engineering, METU   _____

Prof. Dr. Demirkan Çöker
Aerospace Engineering, METU   _____

Prof. Dr. Kemal Levend Parnas
Mechanical Engineering, TED   _____

Assoc. Prof. Dr. Tuncay Yalçınkaya
Aerospace Engineering, METU   _____

Asst. Prof. Dr. Ali Javili
Mechanical Engineering, Bilkent University   _____

Date: 16.08.2021

I hereby declare that all information in this document has been obtained and presented in accordance with academic rules and ethical conduct. I also declare that, as required by these rules and conduct, I have fully cited and referenced all material and results that are not original to this work.

Name Last name : Ahmet Çevik

Signature :

ABSTRACT

EXPERIMENTAL INVESTIGATION OF FAILURE MECHANISM IN CROSS-PLY AND FABRIC CURVED COMPOSITE LAMINATES

Çevik, Ahmet
Master of Science, Aerospace Engineering
Supervisor: Prof. Dr. Demirkan Çöker

August 2021, 129 pages

Laminated curved-shape composite parts which are used in the spar and ribs in aircraft and wind turbine blades are subjected to high interlaminar tensile and shear stresses. These stresses cause delamination and subsequent reduction in load-carrying capacity. In this study, failure mechanism of cross-ply and fabric curved composite laminates under pure transverse loading are examined experimentally using an in-house designed test fixture. Stress field over the curved beam is obtained with finite element analyses (FEA) and analytic solution where multilayered theory is used. Dynamic delamination of the cross-ply and fabric curved specimens is recorded with a high-speed camera where the failure sequence is captured and the crack tip speeds are calculated. For the cross-ply laminates, von Mises strain field is obtained with digital image correlation (DIC) method where the strain fields are found to agree well with elastic FEA up to a specific loading at which a population of matrix cracks nucleate. Detailed fractography of the tested specimens is carried out with digital microscope. Finite element analysis with 2D Hashin Failure criteria is also successfully predict the radial cracks observed in the micrographs of cross-ply curved composite laminates. However, the meandering crack path could not be properly predicted with 2D Hashin Failure Criteria. In fabric curved composite

laminates, the failure is observed to occur due to inter-ply and intra-ply crack growth. In fabric laminates, the crack tip travels in a fluctuating manner at speeds reaching intersonic speeds whereas in cross-ply laminates the crack tip speed reaches about Rayleigh wave speed.

Keywords: Curved Composite, Delamination, Failure Mechanism, Fractography, Crack Tip Speed

ÖZ

DOKUMA VE ÇAPRAZ-KATLI BÜKÜMLÜ KOMPOZİT YAPILARDAKİ HASARIN DENEYSEL YÖNTEMLERLE İNCELENMESİ

Çevik, Ahmet
Yüksek Lisans, Havacılık ve Uzay Mühendisliği
Tez Yöneticisi: Prof. Dr. Demirkan Çöker

Ağustos 2021, 129 sayfa

Uçakların ve rüzgar türbini kanatçıklarının kaburga ve kirişlerinde kullanılan katmanlı bükümlü şekle sahip kompozit yapılar yüksek laminalar arası çekme ve kesme gerilimlerine maruz kalmaktadır. Bu gerilimler delaminasyona ve sonrasında yapıların yük taşıma kapasitelerini kaybetmelerine neden olmaktadır. Bu çalışmada, enine yük altındaki çapraz-katlı ve dokuma bükümlü kompozit yapılarda meydana gelen hasar mekanizması özel tasarlanan test fikstürü kullanılarak deneysel olarak incelenmiştir. Bükümlü laminalar üzerindeki gerilim alanı sonlu elemanlar analizi ve çok-katmanlı kompozit teorisinin kullanıldığı analitik çözüm ile elde edilmiştir. Çapraz-katlı ve dokuma bükümlü kompozit yapılarda görülen dinamik delaminasyon yüksek hızlı kamera kullanılarak kaydedilmiştir. Bu görüntülerde hasar oluşum sırası yakalanmış ve çatlak ucu ilerleme hızı hesaplanmıştır. Çapraz-katlı kompozit numunelerin üzerindeki von Mises gerinim alanı Dijital Görüntü Korelasyon yöntemi ve elastic sonlu elemanlar analizi kullanılarak elde edilmiştir. Bu gerilim alanlarının matris çatlaklarının yoğunlaştığı yüklemeye kadar uyum sağladığı gözlemlenmiştir. Testlerde kullanılan numuneler üzerinde dijital mikroskop kullanılarak detaylı fraktografi analizi yapılmıştır. Çapraz-katlı bükümlü

kompozit yapılarda görülen radyal çatlaklar, iki boyutlu Hashin hasar kriteri ile başarılı bir şekilde tahmin edilmiştir. Ancak kıvrımlı çatlak ucu ilerleyişi tahmin edilememiştir. Dokuma bükümlü kompozit yapılarda hasarın katmanlar arasında ve katman içerisinde oluştuğu gözlemlenmiştir. Dokuma laminalarda çatlak ucu hızının dalgalı bir seyir izlediği ve intersonik hızlara ulaştığı gözlemlenirken çapraz katlı numunelerde Rayleigh dalga hızına yaklaştığı gözlemlenmiştir.

Anahtar Kelimeler: Bükümlü Kompozit, Delaminasyon, Hasar Mekanizması, Fraktografi, Çatlak Ucu İlerleme Hızı

To A Happier Year

ACKNOWLEDGEMENTS

TABLE OF CONTENTS

LIST OF TABLES

TABLES

LIST OF FIGURES

FIGURES

CHAPTER 1

INTRODUCTION

Composites materials consist of two or more components, namely fibers (carbon, aramid, glass) and matrices (epoxy, vinyl ester, polyester). Fibers are the main load-carrying members while matrices bind fibers together to create the medium, that enables load transfer between fibers. For example, steel-reinforced concrete is a composite material where the steel bars act as fiber and concrete acts as matrix. Composite materials can be designed to satisfy the requirements by combining different fibers and matrices. Carbon fiber-reinforced epoxy is used in aerospace applications due to its high fatigue resistance [1]. Kevlar reinforced epoxy is used in military applications due to its high impact resistance [2], and glass fibers with polymer matrices are used in many areas due to their higher durability, electrical resistivity, acid corrosion resistance, etc. [3]. In addition to combining different matrices and fibers, composite materials are also manufactured by stacking with different orientations to obtain desired strength and stiffness, as shown in Figure 1.1.
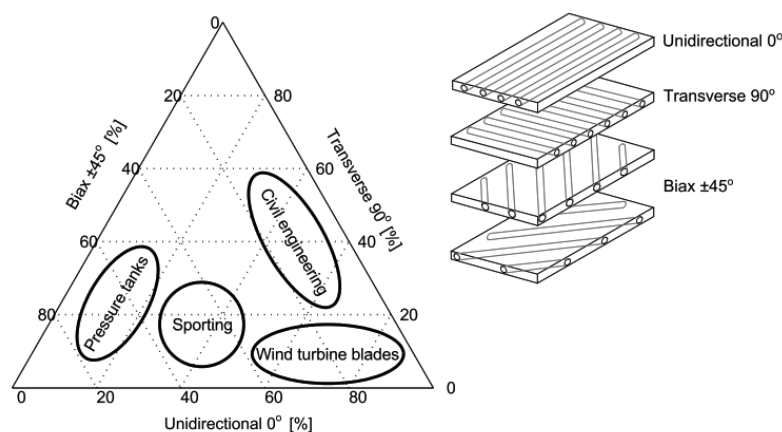
Figure 1.1. Stacking of the composite plies with different orientation [4]

As shown in Figure 1.2, two other great advantages of composite materials are significantly higher specific stiffness and specific strength compared to metals & metallic alloys. These properties make the composite materials desirable for weight-saving that is crucial in aerospace and wind power industries.

Consequently, as time progresses usage of the composites increases in aircrafts and wind turbine. Figure 1.3a show that after 2000, at least 20 % of the airplane components in some of the well-known aircrafts are made of composites, and Figure 1.3b show that composite materials replace metallic components over the years in a series of aircrafts.
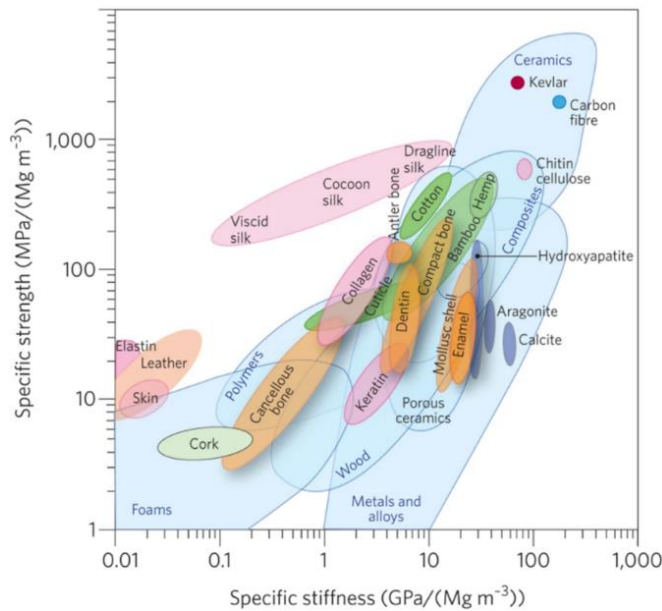
Figure 1.2. Ashby chart which shows the specific stiffness and strength of the materials [5]

(a)   (b)

2
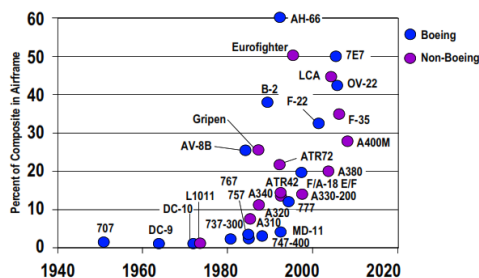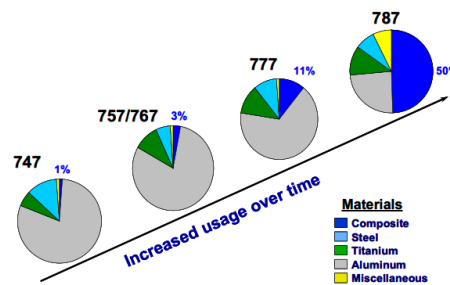
Figure 1.3. (a) Increase in the percent of composite used in the aircraft and (b) The percent of the material type used in the Boeing aircrafts.

In the aerospace and wind power industries, composite materials are used in such as primary load-carrying structures. Thus, they are prone to failure if they are not designed well, and knowing the failure mechanism of the composite materials is vital for safe design. In Figure 1.4, the main failure modes observed in the composite materials are shown. Fiber failure is the most severe mode since it leads to the total failure of the structure. However, delamination usually occurs before the fiber failure occurs [6]. Delamination and matrix cracking are the common failure modes observed in composite materials. Matrix cracking normally does not lead to the total failure of the structure, and induces delamination. Delamination is a highly crucial failure mode since it leads to the reduction in the stiffness and strength of the structure [7][8].
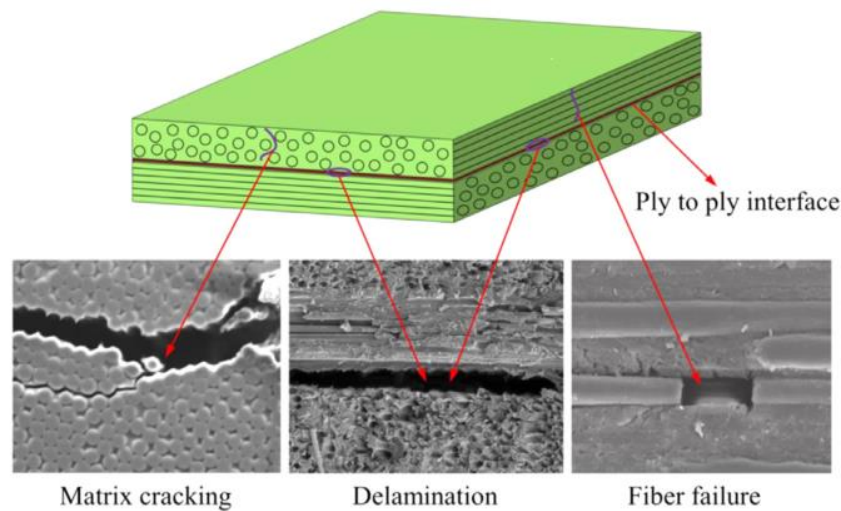
Figure 1.4. Failure modes observed in the composite materials: Matrix cracking, delamination and fiber failure [9]

Recent technologies in the manufacturing methods of composite materials enable production of complex shape structures. One of these complex shape structures is the curved shaped sub-components from which aircraft spar, ribs and wind turbine blades are constructed, as shown in Figure 1.5. These curved structures are prone to

delamination failure mode since high interlaminar tensile and shear stresses arise in their curved region.
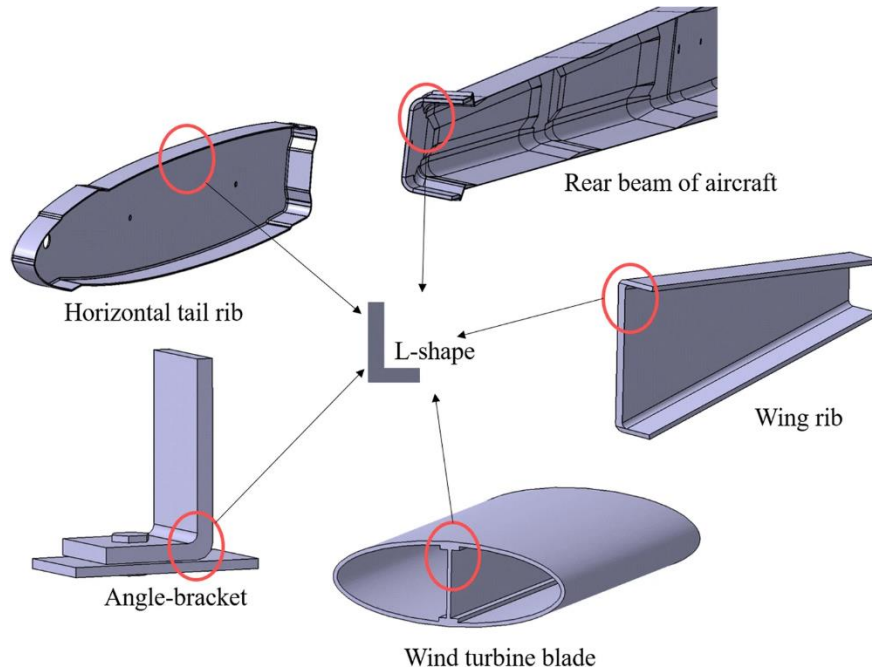
Figure 1.5. Curved sub-components in wing turbine blade or aircraft wing [10]

In this study, experiments are conducted to investigate the failure mechanism of cross-ply and fabric curved composite laminates under pure transverse loading. Experiments of cross-ply and fabric curved composite specimens are recorded with high-speed camera, and crack tip speed are calculated. For cross-ply curved composite laminates, digital image correlation method is also used in some experiments. By using digital image correlation method, in-situ von Mises strain field is calculated and compared that obtained finite element analysis. For both cross-ply and fabric curved composite laminate, the detailed fractography is carried out. The post-mortem micrographs of the failure pattern of the specimen's curved region and arms are examined in detail. The microscopic observations of cross-ply and fabric curved composite laminates are supported by conducting finite element analysis and investigating theoretical and numerical studies in the literature.

CHAPTER 2

LITERATURE SURVEY

In this section, previous experimental and numerical studies about the curved beam will be given chronologically.

Very early study about curved beams was made by Chang and Springer [11]. They investigated the effect of the geometry (inner radius, angle of the curve), load direction and stacking sequence on the strength of the curved beam by developing finite element code to find strains and stresses in each ply. To determine the strength of curved beam, they used Tsai-Hill failure criterion for in-plane failure mode (matrix failure) and Chang-and-Springer failure criterion for out-of-plane failure mode (delamination failure). As understood from the name of delamination failure criteria, it is proposed by the authors, and it is in the form of

$$\left(\frac{\sigma_r}{Y}\right)^2 + \left(\frac{\tau_{rt}}{S}\right)^2 = 1$$

where σ_r and τ_{rt} are radial and shear stress, and Y and R are the radial and shear strength. For five different stacking sequences, the change of the strength with increasing the inner radius to thickness ratio is plotted as shown Figure 2.1a-e. For each stacking sequence, effect of 3 different curve angle (60°, 90°, and 120°) and load direction on the strength is also presented. Load type is called as inward and outward as regard to that it decreases or increases the curve angle, respectively. For all stacking sequence, strength of the curved beam under outward load is lower than that under inward load. For the outward load, delamination failure mode is observed in all stacking sequence. For the inward load, however, delamination failure is observed for only small ratios of inner radius to thickness. In the higher ratios, in-plane failure mode is observed. Effect of the moment length arm and stacking sequence on the strength of curved beam is shown in Figure 2.2a-b, respectively.

Strength of the curved beam decreases as the moment arm length increases, and placing ninety-degree-ply on the middle of the thickness of curved beam improves the strength of the curved beam.

Two studies were performed by Sun and Kelly to investigate the failure in curved composite laminates [12][13]. In the first study [12], the failure load of the curved composite laminates was predicted experimentally and numerically. Schematic of the test setup used in the experiments shown in Figure 2.3a. Experiments were conducted with curved composite laminates having 3 different cross-ply stacking sequence: layup H $[0/90_3/0_2/90_3/0]_s$, layup I $[0_3/90/0_3/90/0/90]_s$ and layup J $[0_3/90_3/0_2/90_3/0]_s$. Layup H and J were chosen to observe matrix failure mode while layup I was chosen to observe delamination failure mode. To calculate the failure load numerically, Tsai-Hill and combined Tsai Hill/Maximum radial stress criteria were used to predict the failure load due to matrix crack and delamination, respectively.
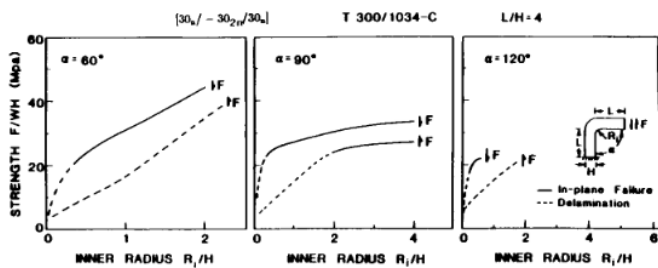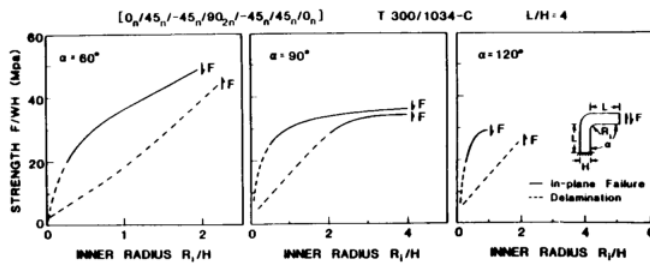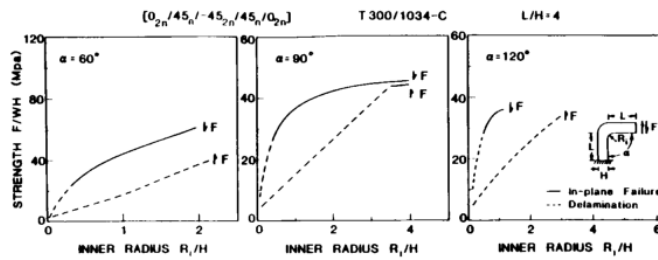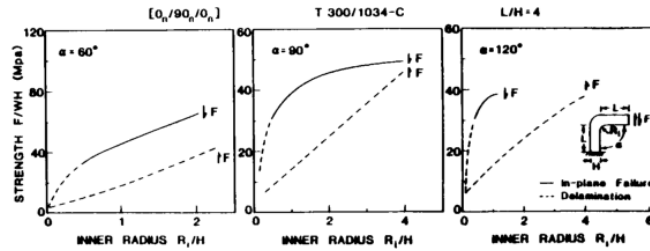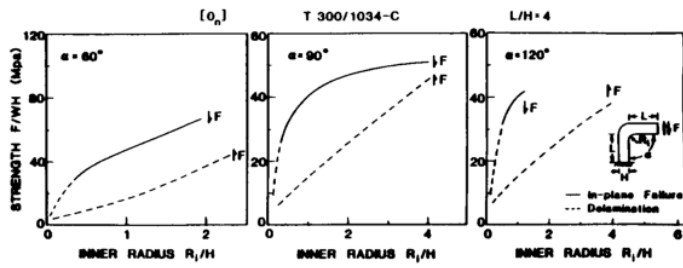
Figure 2.1. Strength versus Inner radius to thickness ratio for 5 different stacking sequence: (a) $[0_n]$, (b) $[0_n/90_n/0_n]$, (c) $[0_{2n}/45_n/-45_{2n}/45_n/0_{2n}]$, (d) $[0_n/45_n/-45_n/90_{2n}/-45_n/45_n/0_n]$, (e) $[30_n/-30_{2n}/30_n/]$
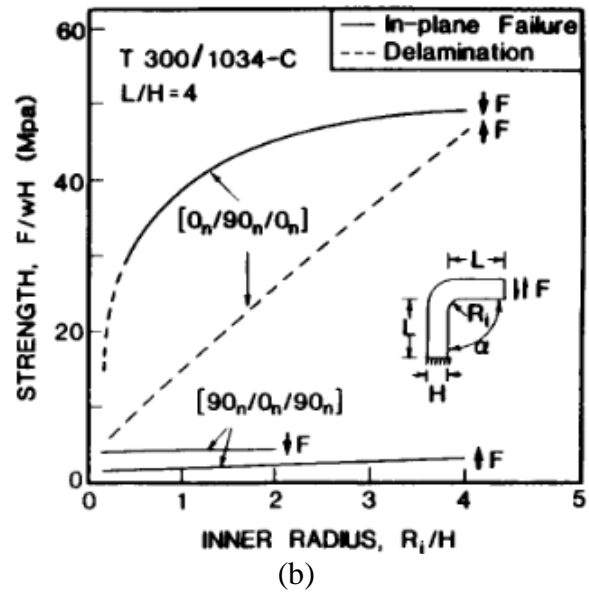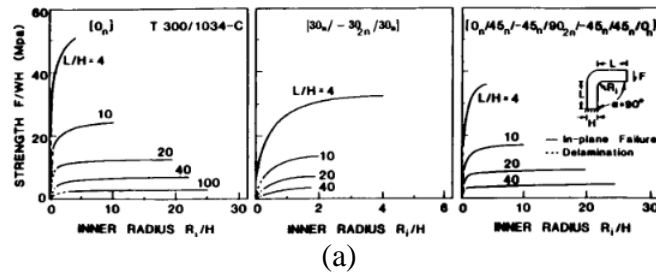
Figure 2.2. Effect of (a) the moment arm length and (b) stacking sequence on curved beam strength

In layup H, radial matrix cracks, shown in Figure 2.3b, were observed in the first ninety-degree-oriented grouped plies and these cracks were attributed to high tangential tensile stresses due to bending of the specimen. The results of the Hill criterion agreed very well with the experimental results in terms of failure load and failure mode. They concluded that i) due to the curvature, high interlaminar tensile stresses act on the curved region of the specimen, and it leads to the delamination, ii) matrix cracks does not lead to the loss of load carrying capacity of the specimen, but delamination induced by these cracks result in total failure of the specimen.

8
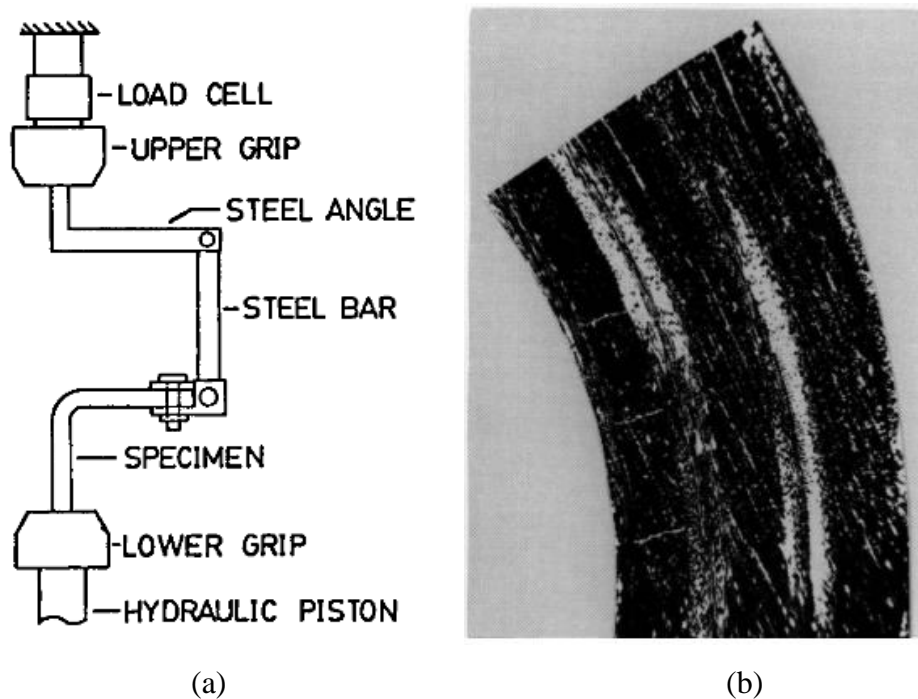
<div align="center">(a)   (b)</div>

<div align="center">Figure 2.3. Schematic of the experimental setup</div>

In the second study carried out by Sun and Kelly [13], propagation of the delamination is investigated by calculating strain energy release rate (SERR) with crack closure integral technique. The radial matrix crack observed in layup H and J can propagate in four possible branches shown in Figure 2.4a. SERR was calculated by extending crack a small amount for each branch. The branch direction 2 gave the maximum SERR, which means that the delamination will propagate in that direction. For the delamination propagated in that direction, change of SERR with delamination crack length was obtained as shown in Figure 2.4b. Same procedure is applied for the direction of propagation of delamination observed in lay-up I, shown in Figure 2.4c, and SERR versus delamination crack length was again obtained as shown in Figure 2.4d. From the trend of the SERR versus Delamination crack length graphs, they concluded that delamination propagation in curved composite laminates is unstable since SERR values increases with increasing delamination length, and crack is arrested when SERR value decreases to below critical value which is sufficient to propagate delamination.

<div align="center">9</div>
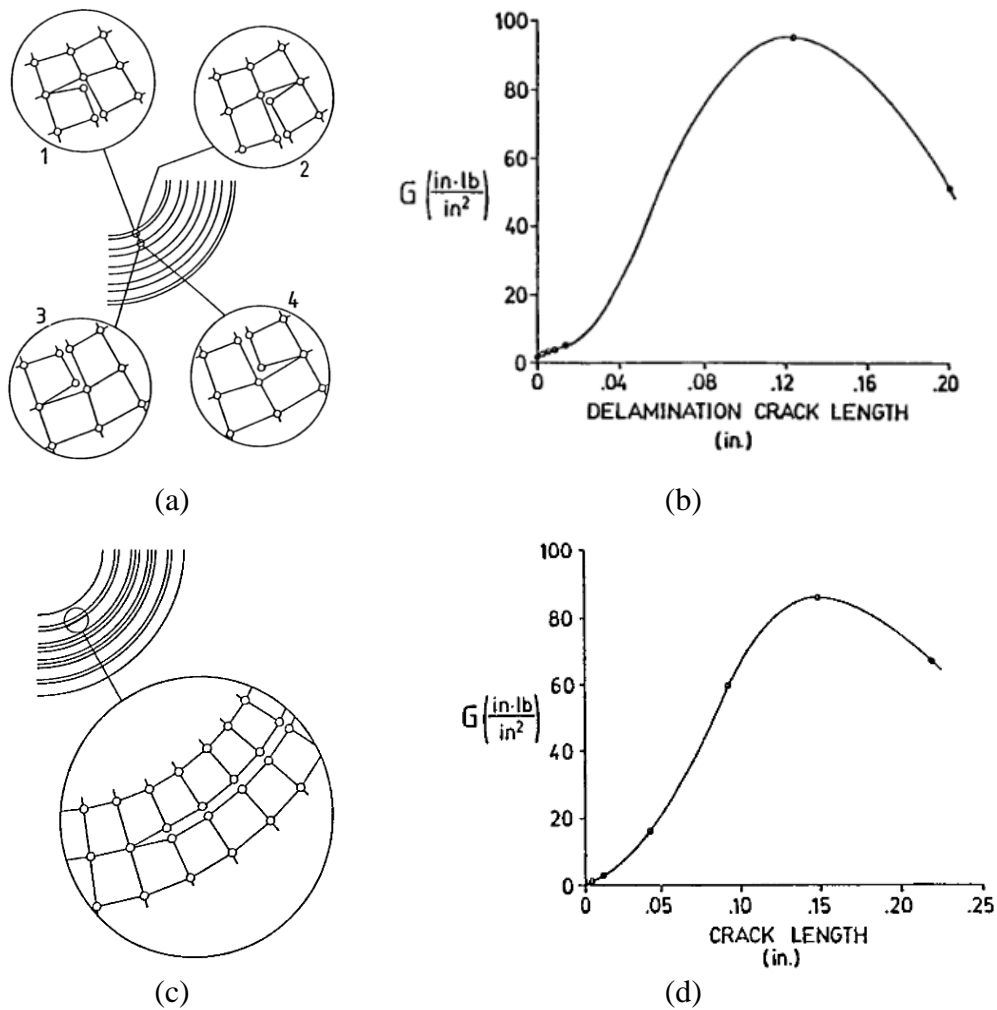
Figure 2.4. (a) Possible branch direction for a radial matrix crack (b) Graph of the SERR vs Crack length of the delamination induced by matrix crack (c) Crack tips for delamination and (b) Graph of the SERR vs Delamination crack length

Martin investigated the failure in unidirectional curved composite laminate both experimentally and numerically [14]. To observe the interlaminar tensile failure, unidirectional curved composite laminates were used. Experiments were conducted with setup shown in Figure 2.5a, and failure sequence observed in curved composite laminate is shown in Figure 2.5b, 1st delamination occurred in the 46 % of the thickness, then 2nd delamination occurred in the 23 % of the thickness. By using the analytic solution method, the location where maximum radial stress occurs is found, and it is observed that the first delamination occurs in the interface which is the closest to the location of the maximum radial stress. Through the thickness, radial

10

stress distribution for a curved laminate with an initial delamination is obtained with finite element analysis shown in Figure 2.5c. It is observed that 2nd delamination is also triggered from the radial stress which reaches approximately same magnitude with the radial stress leading to the 1st delamination.
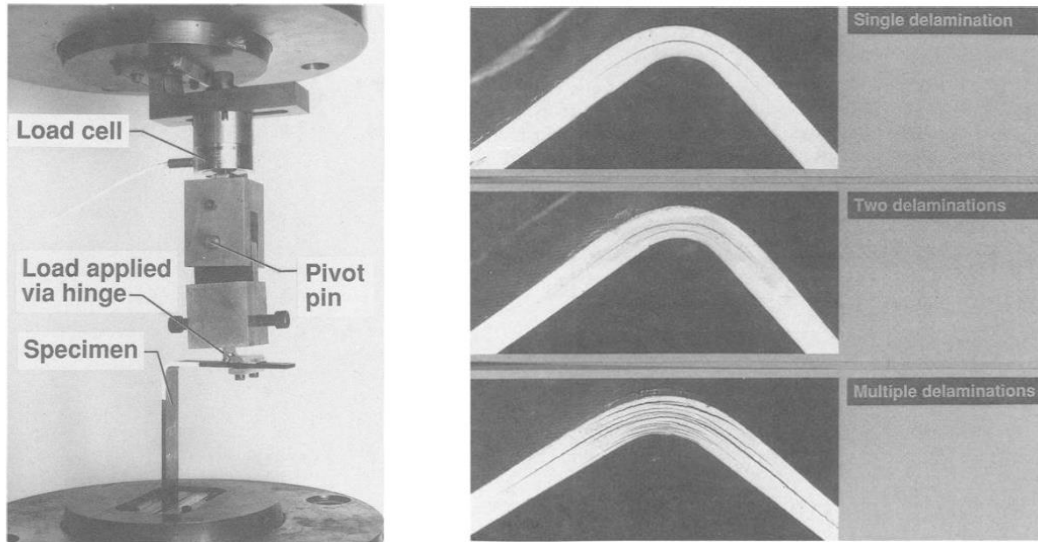
(a)

(b)
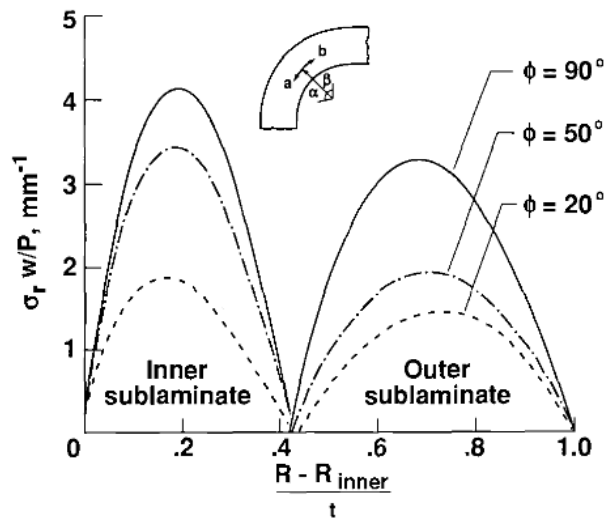
(c)

Figure 2.5. (a) Test setup (b) Failure sequence in unidirectional curved laminate (c) radial stress distribution through the thickness

By using virtual crack closure technique, strain energy release rate is obtained for the propagation of two crack front, which is shown in Figure 2.6a. This graph shows

11

that the delamination grows in both directions simultaneously. By using Figure 2.6a, Strain energy release for total delamination length is obtained as shown Figure 2.6b. This plot shows that the propagation of delamination is unstable while the crack reaches $\phi = 60°$ where the curved region ends. After that point, delamination grows in the stable manner. From the ratio of the mode I strain energy release rate to the critical strain energy release rate Figure 2.6c shows, it is concluded that propagation in two crack fronts is mode-I dominated.
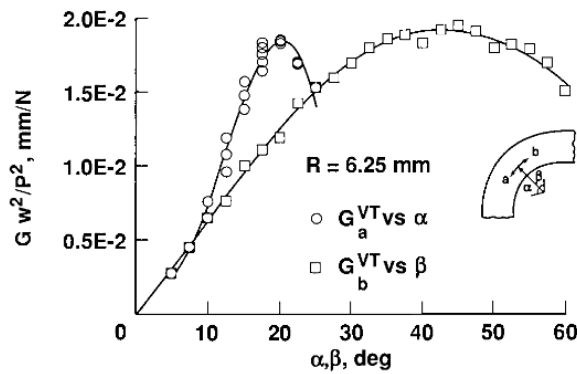
FIG. 15—G_a *versus* α *and* G_b *versus* β.

(a)
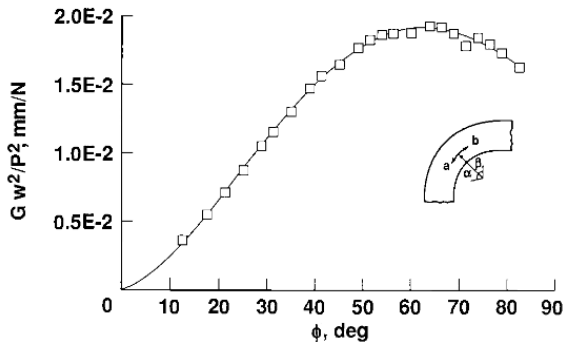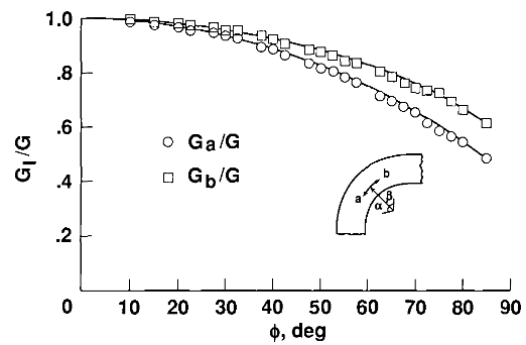
(b)   (d)

Figure 2.6. (a) Crack length versus Normalized strain energy release rate (SERR) for both crack fronts (b) Normalized equivalent SERR for delamination (c) ratio of Mode I energy release rate to equivalent SERR

Martin and Jackson investigated the failure in curved composite laminates having a stacking sequence of $[0_4/90_3/0_5]_s$ to predict delamination onset and propagation [15].

Experimental setup is same with that used in [14]. Static and fatigue experiments were carried out. In Figure 2.7, failure observed in the tested specimen is shown and matrix crack is observed.
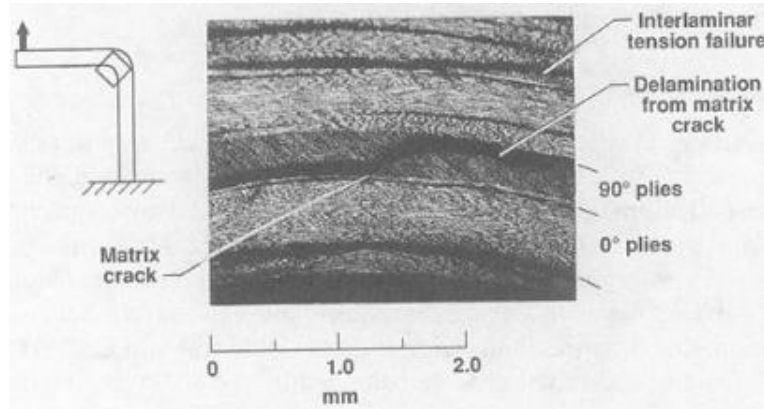
Figure 2.7. Failure modes observed in the tested specimen

For the four possible branch direction of the matrix crack strain energy release rate is calculated with virtual crack closure technique, and its change with the crack length grow is shown in Figure 2.8. Higher strain energy release rate is obtained for the crack growth in the direction of b1. Thus, the matrix crack propagates through the direction of b1 then through the direction a2 which gives the higher strain energy release rate after the direction b1.
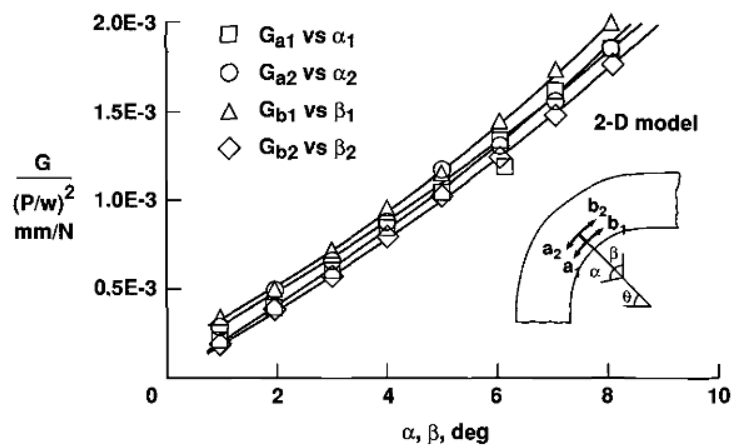
Figure 2.8. Strain energy release rate versus crack length growth for the possible crack branches

The failure of the single-L joint with adhesive between the curvature and the base plate under bending was investigated by Feih and Shercliff [16]. Effect of the bending moment arm (61 mm and 70 mm), stacking sequence and radius of curvature on the failure strength of the L-piece was investigated. Single-L joint specimen and schematic of applied loading are as shown Figure 2.9a-b, respectively. 2D finite element model was created with ABAQUS. Fiber and matrix failure were predicted using Hashin Criteria, and UMAT code was implemented in ABAQUS to carry out progressive damage analysis with constant degradation variables. In addition to the fiber and matrix failure, onset of delamination was predicted using Tong-Norris Criterion which is a strength-based failure criterion. As shown in Figure 2.9c, tensile matrix crack followed by compressive matrix crack was observed in the simulations. Location of the matrix cracks is seen in Figure 2.9d, tensile matrix crack occurred in the inner 45° ply while the compressive matrix crack occurred in the outer 45° ply. Delamination occurred in the interface between the second 0° ply and -45° ply. For both 70 mm moment arm and 61 mm moment arm, delamination failure load was overestimated by %17. This discrepancy was attributed to the residual stresses that occurred during the manufacturing. By decreasing fiber strength by 15%, Tong-Norris criteria was calibrated. They found that failure strength decreased as radius of the L-piece decreases. As for effect of stacking sequence, it is observed that placement of the 90° ply on the middle of the specimen improves the failure strength. In addition, effect of combined tensile and bending moment displacement on the failure strength of L-piece joint was analyzed, and it was shown that failure strength increases in the presence of combined loading.
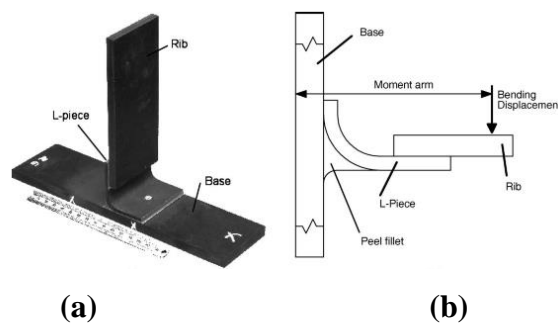
(a)   (b)
Figure 2.9. (a) Single L-joint (b) Schematic of the test setup

14
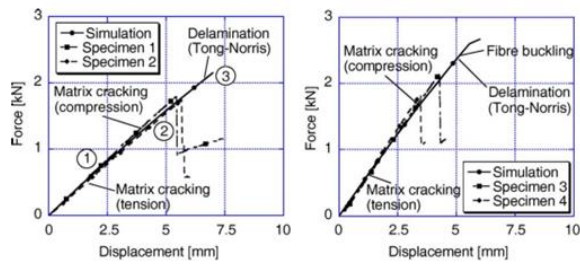
(a)
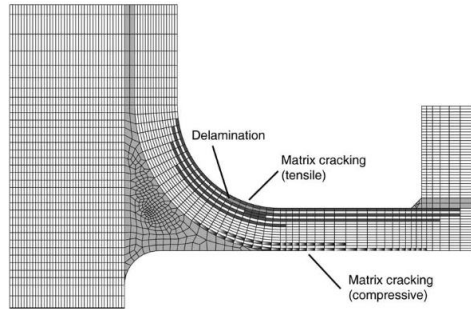
(b)

Figure 2.10. (a) The prediction of the delamination with Tong-Norris criterion and (b) Failure modes observed in finite element analysis

Computational and experimental investigation of the delamination onset and delamination growth of L-shaped CFRP composite laminates were carried out by Wimmer et al [17]. Stacking sequence was chosen as $[0_3/90_3/0_3/90_3/0_3]_s$ to observe delamination failure mode. For prediction of the delamination onset, finite element model (or specimen) without initial delamination was used. Using puck criteria, delamination initiation curve, solid line shown in Figure 2.11a, was obtained, then using VCCT, delamination propagation curve, dashed line in Figure 2.11a, was obtained. Intersection point of these curves were called delamination emergence load (2.34 mm) and critical initial delamination size (0.6 mm). Using delamination emergence load and critical delamination size, load displacement curve of L-shaped curved beam was obtained as shown in Figure 2.11b. FEA model of the L-shaped laminate was loaded up to the delamination emergence load (point 1 shown in Figure 2.11b) then critical initial delamination size was introduced into the FE model. It is observed that load reduced to point 2 shown in Figure 2.11. Delamination grew in an unstable manner from point 1 to 3. Additional delamination on the outer curved region of L-shaped beam occurred (point 4 shown in Figure 2.11b). For delamination

15

onset case, comparison of the numerical load displacement curve with the experimental ones is shown in Figure 2.11c. Unstable crack growth and 2nd delamination in outer curved region were also observed in experiments. Numerical results, however, overpredicted the experimental results in terms of failure load and stiffness of the L-shaped laminate. This discrepancy was attributed to the non-constant thickness and slipping of specimens.

(a)

(b)

(c)
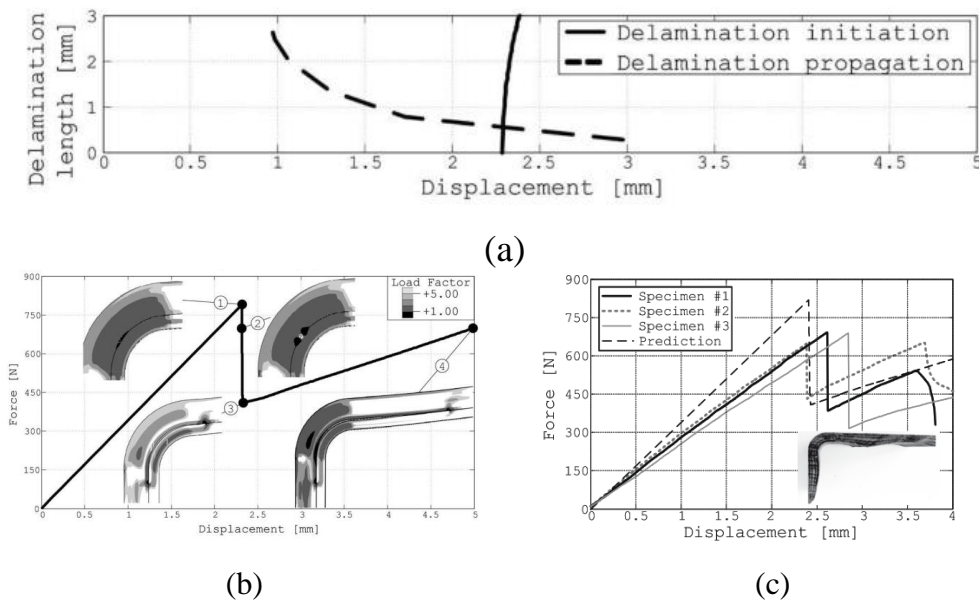
Figure 2.11. (a) Delamination initiation and delamination propagation curve (b) Load-displacement curved obtained from finite element analysis (c) comparison of load displacement curve obtained from experiment and finite element analysis

To simulate the delamination growth, semi-analytical approach developed by the authors was implemented in ABAQUS. Quadratic criterion for mixed mode fracture was used in the approach. FE models having a different initial delamination size (1 mm, 3 mm and 5 mm) were created. Load displacement curve of all models is shown in Figure 2.12a. Unstable delamination growth was observed in the analysis of initial delamination size of 1 mm while delamination growth is stable in the analysis of delamination size of 3 and 5 mm. Snap back behavior theoretically possible occurred in the analysis of 1 mm delamination size. For delamination growth case, experiments were carried on specimens only having delamination size of 3 mm. Comparison of the numerical load displacement curve with the experimental ones is

shown in Figure 2.12b. Initial stiffness of three specimens agree with the prediction. Structural response of specimen 5 was also in good agreement with the prediction in terms of failure load and growth stability. Overpredicting of the failure displacement and failure load in specimen 4 and 6 is attributed to the slipping of the specimen and creating blunt delamination front. In addition, delamination kinking observed in experiment matched with the direction analytically predicted.

a   b
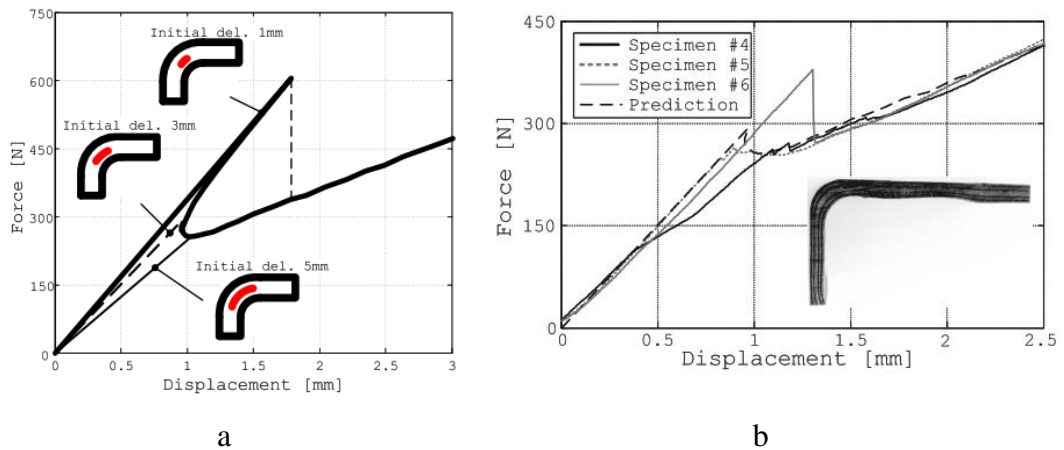
Figure 2.12. (a) Load displacement curves obtained from the models with different initial crack length (b) comparison of load displacement curves obtained from experiment and finite element analysis with a 3 mm initial crack length

Gozluklu and Coker [18] investigated the propagation of dynamic delamination in unidirectional curved composite laminates, with initial crack, under end normal load. 2D Explicit finite element analysis was carried out with cohesive zone model to simulate the propagation of delamination. After the curved beam is loaded implicitly to a certain displacement in the elastic part of the load-displacement curve, analysis continue explicitly. Propagation of delamination simultaneously over the both arms is shown in Figure 2.13.
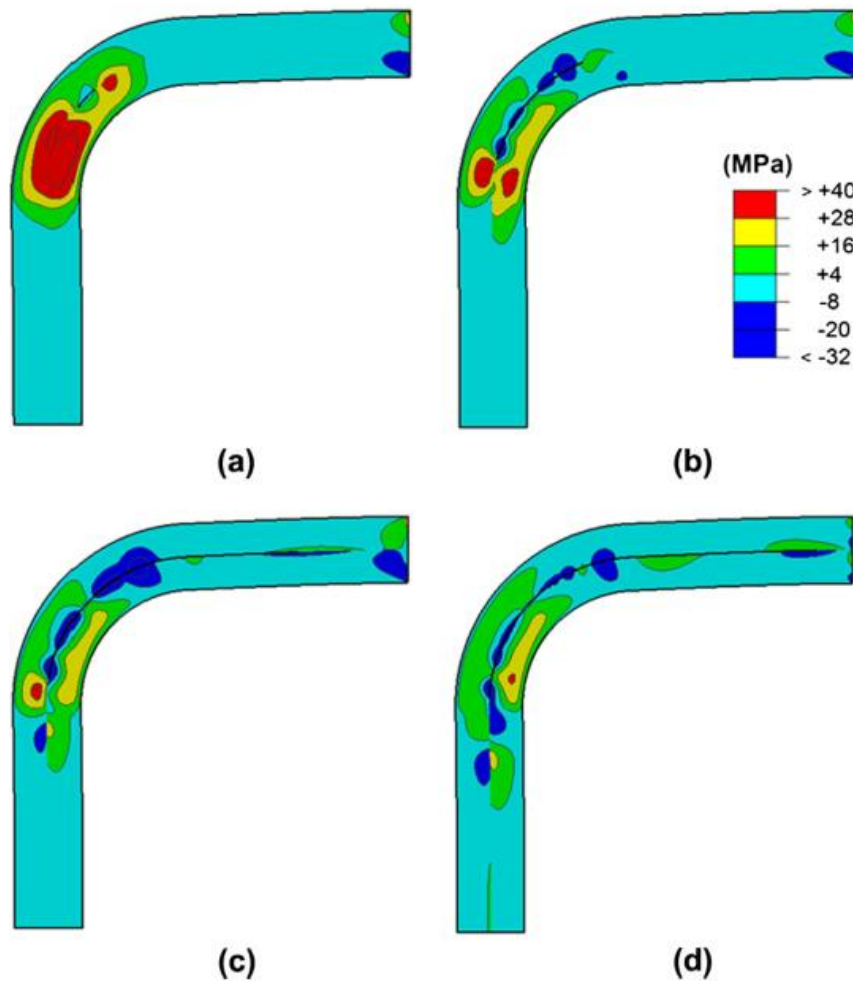
Figure 2.13. The propagation of the initial crack through both arms

In addition to the propagation of delamination, the effect of the thickness of the curved beam on the failure process is examined by keeping the inner radius of curved beam constant, its thickness is doubled, and finite element analysis was carried out. As shown in Figure 2.14, it is observed that the doubling the thickness of the curved beam leads to another crack which initiates in the transition region between the curve region and horizontal arm. This crack propagates through the curve region and horizontal arm, then coalesce with initial crack.

18
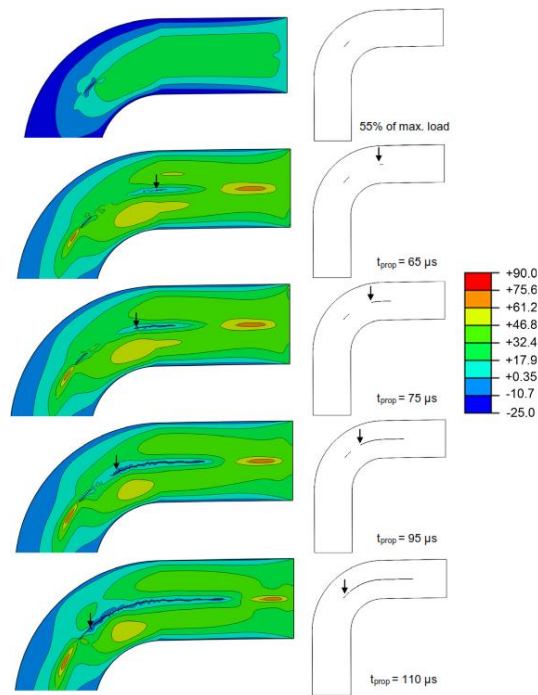
Figure 2.14. Failure sequence observed in the thicker curved composite laminate with an initial crack

Gozluklu et al. [19] experimentally and numerically investigated the intersonic delamination in fabric curved composite laminates, having a stacking sequence of $[0/90]_{6s}$, under static loading. Graphite/epoxy woven fabric laminates with was manufactured. By using the test fixture shown in Figure 2.15a, shear loading was applied to the horizontal arm of the curved laminated while vertical arm was clamped. To prevent the reaction on the vertical arm in the x direction, fixture is mounted to slide rail via linear ball bearings. By using the high-speed camera propagation of dynamic delamination is captured, and crack tip speed history is obtained. 2D explicit FEA was carried out to simulate the dynamic delamination with cohesive interface elements. Bilinear cohesive zone model proposed by Miu et al. was implemented via user-subroutine with Chang-Springer criterion for delamination onset and Benzeggagh and Kenane mixed-mode fracture criterion. Initiation and delamination in simulation and experiment can be seen in Figure 2.15b. In the experiment and simulation, delamination initiated from a point located 12° and 13° counterclockwise from center of curved region. In terms of location of the

observable crack tip (Left (L) and Right (R)), experiment and simulation were consistent. To calculate the crack tip speed from simulation, two different crack tips were used. First crack tip was chosen as observable crack tip where the damage term is one. Second crack tip was chosen point where the damage term is 0.6. Under quasi-static loading, crack tips propagating through the vertical and horizontal arm reach a speed of about 4000 m/s which is faster than shear wave speed. The shear Mach waves emanating from the crack tip where damage term is 0.6 at the vertical and horizontal arm and reflection of the waves from the wall of arm is shown in Figure 2.15. Moreover, oblique angle of the shear Mach wave increase with decreasing crack tip speed.

(a)

(b)

(c)

(d)
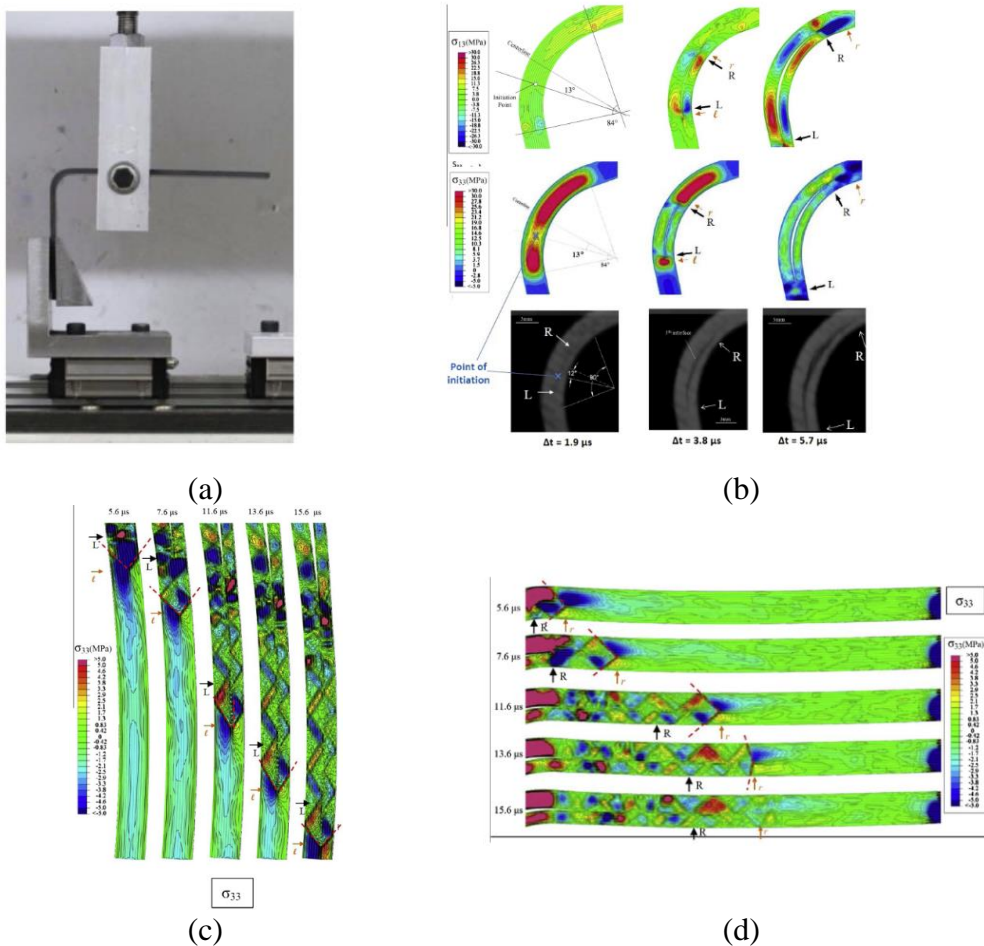
Figure 2.15. (a) Novel experimental setup designed (b) Comparison finite element result with numerical results in terms of crack initiation and propagation (c-d) shear Mach waves emanating from the crack tip where damage parameter is 0.6 at vertical and horizontal arm.

Tasdemir and Coker [20] experimentally investigated the static and fatigue damage mechanism of cross-ply curved composite laminates having two different layup configurations. These configurations are $[0_3/90_3/0_3]_s$ and $[0_3/90_3/0_3/90_3/0_3]_s$ which are called as thin and thick laminates, respectively. Experimental fixture shown in Figure 2.16a is designed and manufactured to apply three types of load: end shear load, end normal load and bending moment. In thin cross-ply curved composite laminates, delamination induced by matrix cracks in the 1st 90° grouped plies, shown in the Figure 2.17a, are observed both under static and fatigue loading. Under static loading, straight matrix crack reaches the upper 0/90 interface by making sharp 45-50° kink. In fatigue experiments, however, matrix crack reaches the 0/90 interface by making meandering path following the manufacturing defects. In the thick cross-ply curved composite laminates, damage is observed to occur in the form of straight matrix crack in the 1st 90° grouped plies under static loading while meandering matrix crack in the 2nd 90° grouped plies under fatigue loading shown in the Figure 2.17b. Investigating the difference in the failure location under static loading and fatigue loading, it is observed that, the failure in cross-ply laminates occurs in where failure index according to the Tsai-Wu criteria is maximum under static loading while it occurs in which the radial stresses is maximum under fatigue loading.
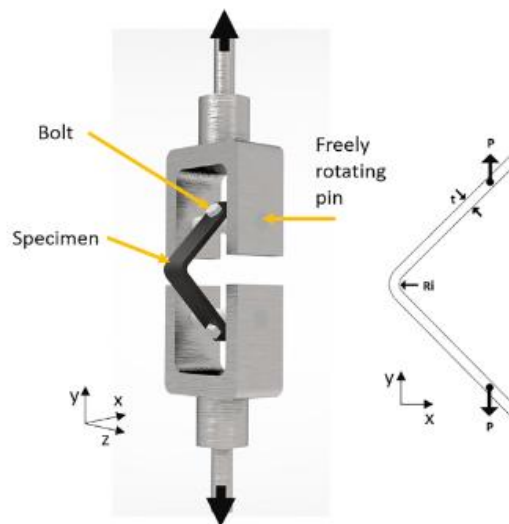
Figure 2.16. Experimental fixture designed.

(a)

(b)
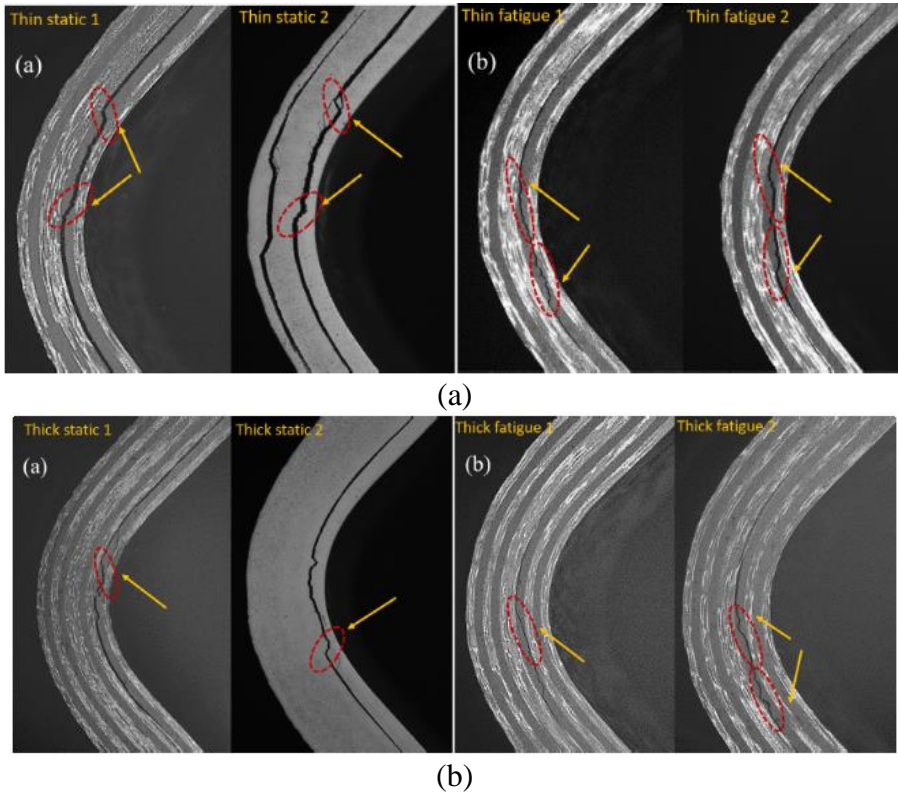
Figure 2.17. (a) damage pattern observed in thin laminates under static and fatigue loading (b) damage pattern observed in thick laminates under static and fatigue loading

CHAPTER 3

METHOD

In this study, experiments are conducted with cross-ply and fabric curved composite laminates under pure transverse loading, and finite element analyses are carried out to find the stress field over the curved beam to understand the failure of the curved composite laminates better. In this chapter, methodologies used in the experiments and finite element analysis are explained.

3.1 Experimental Method

3.1.1 Material

Unidirectional and fabric specimens are manufactured with Hexply AS4/8552 UD prepreg and Hexply AS4/8552 5 Harness Satin (HS) prepreg, respectively. Hexply 8552 epoxy has good impact resistance and damage tolerance for aerospace applications [21], and HexTow AS4 is continuous carbon fiber having high strength and strain [22]. The representative view of these materials is shown in Figure 3.1.
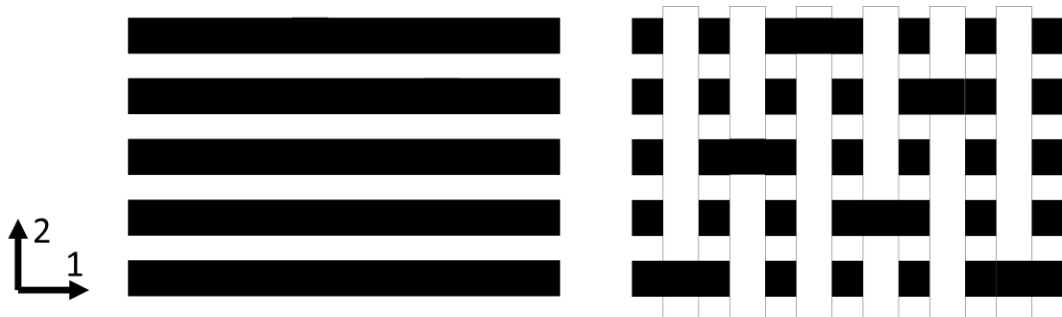
Figure 3.1. Representative view of unidirectional (left) and 5 HS weave prepregs (right)

The properties of these materials are given in Table 3.1 and Table 3.2

Table 3.1 Material properties of Hexply AS4/8552 UD prepreg [23]

E_{11} (GPa)	$E_{22}=E_{33}$ (GPa)	$v_{12}=v_{13}$	v_{23}	$G_{12}=G_{13}$ (GPa)	G_{23} (GPa)	ρ (kg/m^3)	t_p (mm)	G_{Ic} (N/mm)
135	9.6	0.32	0.487	5.3	3.4	1580	0.188	0.28

Table 3.2 Material properties of Hexply AS4/8552 5 HS prepreg [24]

$E_{11}=E_{22}$ (GPa)	E_{33} (GPa)	v_{12}	$v_{13}=v_{23}$	G_{12} (GPa)	$G_{23}=G_{13}$ (GPa)	ρ (kg/m^3)	t_p (mm)
64	8.5	0.046	0.3	4.9	3.7	1570	0.28

The material strength for Hexply AS4/8552 UD prepreg and Hexply AS4/8552 5HS prepreg are given in Table 3.3 and Table 3.5.

Table 3.3 Material strength of Hexply AS4/8552 UD prepreg

S_{11}^t (MPa)	S_{11}^c (MPa)	$S_{22}^t = S_{33}^t$ (MPa)	$S_{22}^c = S_{33}^c$ (MPa)	$S_{12} = S_{13}$ (MPa)	S_{23} (MPa)
2207	1531	80.7	199.8	114	80

Table 3.4 Material strength of Hexply AS4/8552 5HS prepreg

S_{11}^t (MPa)	S_{11}^c (MPa)	S_{22}^t (MPa)	S_{33}^t (MPa)	$S_{22}^c = S_{33}^c$ (MPa)	S_{12} (MPa)	$S_{13} = S_{23}$ (MPa)
1800	-1350	75	53	-250	80	79

The wave speed of these materials is calculated by using the [25]

$$c_l^{\parallel} = \sqrt{\frac{c_{11}}{\rho}}, \qquad c_l^{\perp} = \sqrt{\frac{c_{22}}{\rho}}, \qquad c_s = \sqrt{\frac{c_{66}}{\rho}} \tag{3-1}$$

where $c_l^{||}$ is the longitudinal wave speed parallel to the fibers, $c_l^{\perp}$ is the longitudinal wave speed perpendicular to the fibers, and c_s is the shear wave speed. c_{11}, c_{22} and c_{66} are the stiffness matrix components. For an orthotropic material, the stress-strain relationship can be expressed as

$$\sigma_{ij} = c_{ij}\varepsilon_{ij}$$

$$
\begin{bmatrix} \sigma_1 \\ \sigma_2 \\ \sigma_3 \\ \tau_{23} \\ \tau_{31} \\ \tau_{12} \end{bmatrix} =
\begin{bmatrix}
c_{11} & c_{12} & c_{13} & 0 & 0 & 0 \\
c_{12} & c_{22} & c_{23} & 0 & 0 & 0 \\
c_{13} & c_{23} & c_{33} & 0 & 0 & 0 \\
0 & 0 & 0 & c_{44} & 0 & 0 \\
0 & 0 & 0 & 0 & c_{55} & 0 \\
0 & 0 & 0 & 0 & 0 & c_{66}
\end{bmatrix}
\begin{bmatrix} \varepsilon_1 \\ \varepsilon_2 \\ \varepsilon_3 \\ \gamma_{23} \\ \gamma_{31} \\ \gamma_{12} \end{bmatrix}
\tag{3-2}
$$

In transversely isotropic material, $c_{55} = c_{44}$ and $c_{66} = (c_{11} - c_{12})/2$. [26]. Stiffness matrix components, c_{ij}, can be expressed in terms of material properties;

$$c_{11} = \frac{1 - v_{23}v_{32}}{E_2 E_3 \Delta}, \qquad c_{22} = \frac{1 - v_{13}v_{31}}{E_1 E_3 \Delta}, \qquad c_{33} = \frac{1 - v_{12}v_{21}}{E_1 E_2 \Delta}$$

$$c_{12} = \frac{v_{21} + v_{31}v_{23}}{E_2 E_3 \Delta}, \quad c_{23} = \frac{v_{32} + v_{12}v_{31}}{E_1 E_3 \Delta}, \qquad c_{13} = \frac{v_{31} + v_{21}v_{32}}{E_2 E_3 \Delta} \tag{3-3}$$

$$c_{44} = G_{23}, \qquad c_{55} = G_{31}, \qquad c_{66} = G_{12}$$

In 2D plane stress case, σ_3, τ_{13} and τ_{23} will be zero, and the stress-strain relationship reduces to

$$
\begin{bmatrix} \sigma_1 \\ \sigma_2 \\ \tau_{12} \end{bmatrix} =
\begin{bmatrix}
c'_{11} & c'_{12} & 0 \\
c'_{12} & c'_{22} & 0 \\
0 & 0 & c'_{66}
\end{bmatrix}
\begin{bmatrix} \varepsilon_1 \\ \varepsilon_2 \\ \gamma_{12} \end{bmatrix}
\tag{3-4}
$$

where

$$c'_{11} = \frac{E_1}{1 - v_{12}v_{21}}, \qquad c'_{22} = \frac{E_2}{1 - v_{12}v_{21}}, \qquad c'_{12} = \frac{v_{21}E_1}{1 - v_{12}v_{21}},$$

$$c'_{66} = G_{12} \tag{3-5}$$

Rayleigh wave speed (c_R) can be found by solving the equation below [27]

$$4\sqrt{\left(1-\frac{c_R^2}{c_l{}^2}\right)\left(1-\frac{c_R^2}{c_s{}^2}\right)}-\left(2-\frac{c_R^2}{c_s{}^2}\right)^2=0 \tag{3-6}$$

This equation gives the one real solution where the Poisson's ratio v, is in the range of $0 < v < 0.5$. Rayleigh wave speed parallel and perpendicular to the fibers are calculated by inserting $c_l^{||}$ and $c_l^{\perp}$ into the equation, respectively.

For the materials Hexply AS4/8552 UD and Hexply AS4/8552 5HS, wave speeds are given in Table 3.5 and Table 3.6.

Table 3.5 Characteristic wave speeds of material Hexply AS4/8552 UD

	$c_d^{||}$ (m/s)	$c_d^{\perp}$ (m/s)	c_s (m/s)	$c_R^{||}$ (m/s)	$c_R^{\perp}$ (m/s)
Plane-stress	9277	2474	1831	1745	1562
Plane-strain	9377	2852	1831	1745	1652

Table 3.6 Characteristic wave speeds of material Hexply AS4/8552 5HS

	$c_d^{||}$ (m/s)	$c_d^{\perp}$ (m/s)	c_s (m/s)	$c_R^{||}$ (m/s)	$c_R^{\perp}$ (m/s)
Plane-stress	6391	6391	1767	1678	1678
Plane-strain	6434	6434	1767	1678	1678

3.1.2   Specimens

Experiments are conducted with specimens having a stacking sequence of unidirectional $[(90/0)_4, \overline{90}]_s$ and fabric $[(45/0)_7/45/45/0/45]$. The stacking sequence of the fabric specimens is chosen to be similar to that currently used in commercial airplanes. Sample specimens and microscopic views of their stacking sequences are given in Figure 3.2.
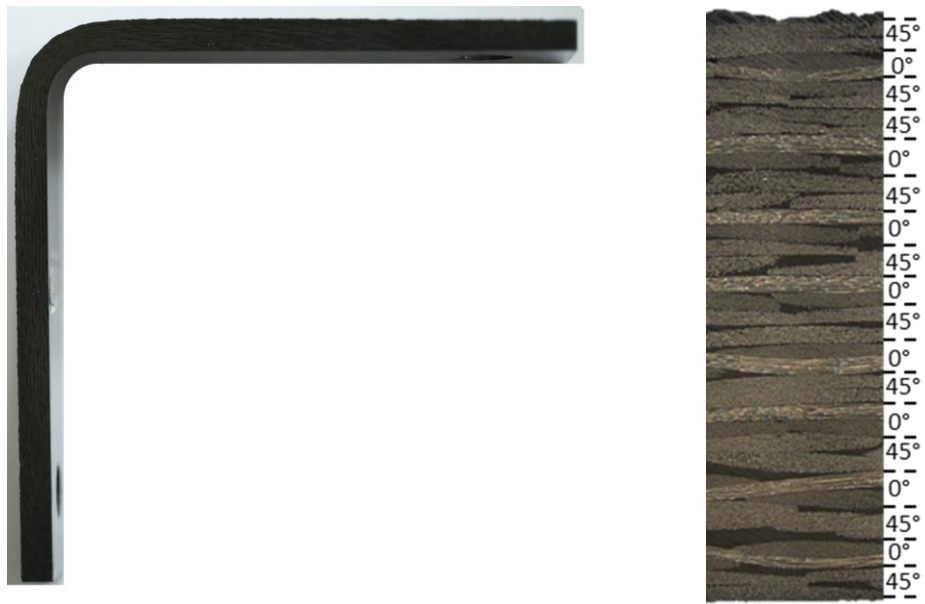
(a)

(b)

Figure 3.2. Sample specimens and microscopic views of their stacking sequences:
(a) Fabric specimen, (b) cross-ply specimen

3.1.2.1 Manufacturing

Specimens are cut from manufactured curved composite plates. Hand layup technique with vacuum bagging is used to manufacture both unidirectional and fabric curved composite plates. Details of the manufacturing process are as follows;

i)   Prepregs are laid up on the Aluminum male tool in the desired order

ii)   Then release film and breather fabric are laid on the prepregs, and all layup is clamped with vacuum bagging.

iii) After the vacuum bagging, the tool is sent to the autoclave for curing cycle.

iv)   In autoclave, the pressure is increased to 6.9 bar at the room temperature, at that pressure temperature is increased to 180° with a rate of 0.5-3 °C/min, resins cured at these conditions for 3 hours, then the temperature is decreased with a rate of 0.5-3 °C/min when the pressure is gradually decreased. The process last 10 hours in total.

v)   After the autoclave process, manufactured curved composite plates are cut into specimens.

More details about the manufacturing process can be found in [20] [28]. In the next section, the geometry of the specimens will be mentioned.

3.1.2.2   Geometry and Laminate Properties

The geometry of the curved specimens is shown in Figure 3.3. L_1 and L_2 are arm length, w is width, t is thickness and r_i is inner radius. Specimen dimensions are given in Table 3.7. These dimensions are nominal. Dimensions of each specimen are measured before the experiment.
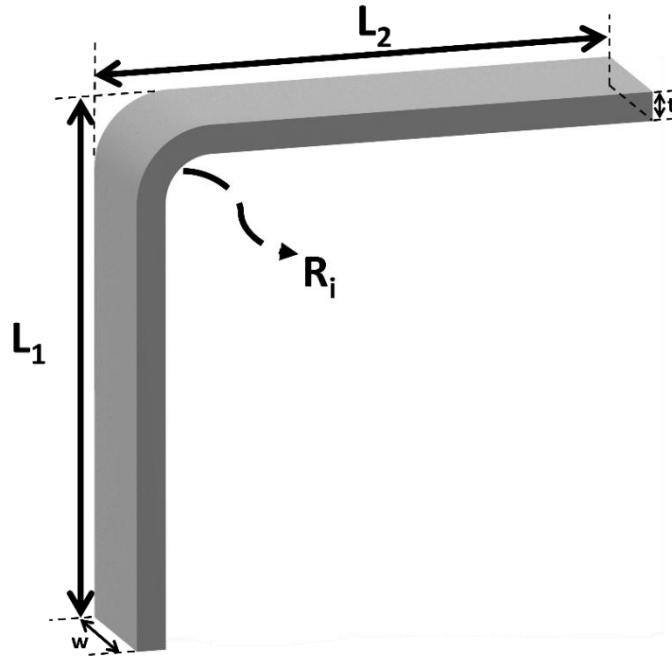
Figure 3.3. Geometry of the curved beam specimen

Table 3.7 Dimensions of the specimens

	L₁ (mm)	L₂ (mm)	Rᵢ (mm)	w (mm)	t (mm)
$[(90/0)_4, \overline{90}]_s$	90	150	10	30	3.196
$[(45/0)_7/45/45/0/45]$	90	90	8	25	5.04

Using classical lamination theory (CLT), general laminate properties of each stacking sequence are calculated. According to CLT, constitutive equation of a laminate is expressed as

$$\begin{bmatrix} N_x \\ N_y \\ N_{xy} \\ M_x \\ M_y \\ M_{xy} \end{bmatrix} = \begin{bmatrix} A_{11} & A_{12} & A_{16} & B_{11} & B_{12} & B_{16} \\ A_{12} & A_{22} & A_{26} & B_{12} & B_{22} & B_{26} \\ A_{16} & A_{26} & A_{66} & B_{16} & B_{26} & B_{66} \\ B_{11} & B_{12} & B_{16} & D_{11} & D_{12} & D_{16} \\ B_{12} & B_{22} & B_{26} & D_{12} & D_{22} & D_{26} \\ B_{16} & B_{26} & B_{66} & D_{16} & D_{26} & D_{66} \end{bmatrix} \begin{bmatrix} \varepsilon_x^0 \\ \varepsilon_y^0 \\ \gamma_{xy}^0 \\ \kappa_x \\ \kappa_y \\ \kappa_{xy} \end{bmatrix}$$
(3-7)

or

$$\begin{bmatrix} N \\ M \end{bmatrix} = \begin{bmatrix} A & B \\ B & D \end{bmatrix} \begin{bmatrix} \varepsilon^0 \\ \kappa \end{bmatrix}$$

(3-8)

where

A is the extensional stiffness matrix,

B is the extensional-bending coupling matrix,

D is the bending stiffness matrix.

For symmetric laminates, matrix [B] will be zero, and only matrix [A] is required to obtain laminate properties. Thus, the laminate properties depend on only the matrix [A] and can be calculated by using the equations [29]

$$E_x = \frac{A_{11}}{h} + \frac{A_{12}}{h}\left(\frac{A_{26}A_{16} - A_{12}A_{66}}{A_{22}A_{66} - A_{26}^2}\right) + \frac{A_{16}}{h}\left(\frac{-A_{16}}{A_{66}} + \frac{A_{26}A_{12}A_{66} - A_{26}^2 A_{16}}{A_{22}A_{66}^2 - A_{26}^2 A_{66}}\right)$$

(3-9)

$$E_y = \frac{A_{22}}{h} + \frac{A_{12}}{h}\left(\frac{A_{16}A_{26} - A_{12}A_{66}}{A_{11}A_{66} - A_{16}^2}\right) + \frac{A_{26}}{h}\left(\frac{-A_{26}}{A_{66}} + \frac{A_{16}A_{12}A_{66} - A_{16}^2 A_{26}}{A_{11}A_{66}^2 - A_{16}^2 A_{66}}\right)$$

(3-10)

$$G_{xy} = \frac{A_{66}}{h} - \frac{1}{h}\frac{A_{26}^2}{A_{22}} + \frac{1}{h}\frac{2A_{12}A_{16}A_{26}A_{22} - A_{12}^2 A_{26}^2 - A_{16}^2 A_{22}^2}{A_{11}A_{22}^2 - A_{12}^2 A_{22}}$$

(3-11)

$$v_{xy} = \frac{A_{12} - \dfrac{A_{16}A_{26}}{A_{66}}}{A_{22} - \dfrac{A_{26}^2}{A_{66}}}$$

(3-12)

$$v_{yx} = \frac{\dfrac{A_{16}A_{26}}{A_{66}} - A_{12}}{\dfrac{A_{16}^2}{A_{66}} - A_{11}}$$

(3-13)

where h is the ply thickness.

For unsymmetric laminates, laminate properties depend on all the stiffness matrices [A], [B] and [D] and equations will be

$$
E_x = \frac{\begin{vmatrix} A_{11} & A_{12} & A_{16} & B_{11} & B_{12} & B_{16} \\ A_{12} & A_{22} & A_{26} & B_{12} & B_{22} & B_{26} \\ A_{16} & A_{26} & A_{66} & B_{16} & B_{26} & B_{66} \\ B_{11} & B_{12} & B_{16} & D_{11} & D_{12} & D_{16} \\ B_{12} & B_{22} & B_{26} & D_{12} & D_{22} & D_{26} \\ B_{16} & B_{26} & B_{66} & D_{16} & D_{26} & D_{66} \end{vmatrix}}{\begin{vmatrix} A_{22} & A_{26} & B_{12} & B_{22} & B_{26} \\ A_{26} & A_{66} & B_{16} & B_{26} & B_{66} \\ B_{12} & B_{16} & D_{11} & D_{12} & D_{16} \\ B_{22} & B_{26} & D_{12} & D_{22} & D_{26} \\ B_{26} & B_{66} & D_{16} & D_{26} & D_{66} \end{vmatrix}} \left(\frac{1}{h}\right) \tag{3-14}
$$

$$
E_y = \frac{\begin{vmatrix} A_{11} & A_{12} & A_{16} & B_{11} & B_{12} & B_{16} \\ A_{12} & A_{22} & A_{26} & B_{12} & B_{22} & B_{26} \\ A_{16} & A_{26} & A_{66} & B_{16} & B_{26} & B_{66} \\ B_{11} & B_{12} & B_{16} & D_{11} & D_{12} & D_{16} \\ B_{12} & B_{22} & B_{26} & D_{12} & D_{22} & D_{26} \\ B_{16} & B_{26} & B_{66} & D_{16} & D_{26} & D_{66} \end{vmatrix}}{\begin{vmatrix} A_{11} & A_{16} & B_{11} & B_{12} & B_{16} \\ A_{16} & A_{66} & B_{16} & B_{26} & B_{66} \\ B_{11} & B_{16} & D_{11} & D_{12} & D_{16} \\ B_{12} & B_{26} & D_{12} & D_{22} & D_{26} \\ B_{16} & B_{66} & D_{16} & D_{26} & D_{66} \end{vmatrix}} \left(\frac{1}{h}\right) \tag{3-15}
$$

$$
G_{xy} = \frac{\begin{vmatrix} A_{11} & A_{12} & A_{16} & B_{11} & B_{12} & B_{16} \\ A_{12} & A_{22} & A_{26} & B_{12} & B_{22} & B_{26} \\ A_{16} & A_{26} & A_{66} & B_{16} & B_{26} & B_{66} \\ B_{11} & B_{12} & B_{16} & D_{11} & D_{12} & D_{16} \\ B_{12} & B_{22} & B_{26} & D_{12} & D_{22} & D_{26} \\ B_{16} & B_{26} & B_{66} & D_{16} & D_{26} & D_{66} \end{vmatrix}}{\begin{vmatrix} A_{11} & A_{12} & B_{11} & B_{12} & B_{16} \\ A_{12} & A_{22} & B_{12} & B_{22} & B_{26} \\ B_{11} & B_{12} & D_{11} & D_{12} & D_{16} \\ B_{12} & B_{22} & D_{12} & D_{22} & D_{26} \\ B_{16} & B_{26} & D_{16} & D_{26} & D_{66} \end{vmatrix}} \left(\frac{1}{h}\right) \tag{3-16}
$$

$$v_{xy} = \cfrac{-\begin{vmatrix} A_{12} & A_{26} & B_{12} & B_{22} & B_{26} \\ A_{16} & A_{66} & B_{16} & B_{26} & B_{66} \\ B_{11} & B_{16} & D_{11} & D_{12} & D_{16} \\ B_{12} & B_{26} & D_{12} & D_{22} & D_{26} \\ B_{16} & B_{66} & D_{16} & D_{26} & D_{66} \end{vmatrix}}{\begin{vmatrix} A_{22} & A_{26} & B_{12} & B_{22} & B_{26} \\ A_{26} & A_{66} & B_{16} & B_{26} & B_{66} \\ B_{12} & B_{16} & D_{11} & D_{12} & D_{16} \\ B_{22} & B_{26} & D_{12} & D_{22} & D_{26} \\ B_{26} & B_{66} & D_{16} & D_{26} & D_{66} \end{vmatrix}} \tag{3-17}$$

$$v_{yx} = \cfrac{\begin{vmatrix} A_{12} & A_{16} & B_{11} & B_{12} & B_{16} \\ A_{16} & A_{66} & B_{16} & B_{26} & B_{66} \\ B_{12} & B_{16} & D_{11} & D_{12} & D_{16} \\ B_{22} & B_{26} & D_{12} & D_{22} & D_{26} \\ B_{16} & B_{66} & D_{16} & D_{26} & D_{66} \end{vmatrix}}{\begin{vmatrix} A_{11} & A_{16} & B_{12} & B_{22} & B_{26} \\ A_{16} & A_{66} & B_{16} & B_{26} & B_{66} \\ B_{11} & B_{16} & D_{11} & D_{12} & D_{16} \\ B_{12} & B_{26} & D_{12} & D_{22} & D_{26} \\ B_{16} & B_{66} & D_{16} & D_{26} & D_{66} \end{vmatrix}} \left(\frac{1}{h}\right) = \frac{E_y}{E_x} v_{xy} \tag{3-18}$$

Laminate properties of each specimen are given in Table 3.8.

Table 3.8 Laminate properties of each stacking sequences

	E_x (GPa)	E_y (GPa)	G_{xy} (GPa)	v_{xy}	v_{yx}
$[(90/0)_4, \overline{90}]_s$	68.99	76.41	5.3	0.0404	0.0448
$[(45/0)_7/45/45/0/45]$	38.5	38.5	16.57	0.35	0.35

3.1.2.3   Specimen Preparation

To make a precise observation during the experiment, coarse and fine grinding is accomplished for each specimen by using abrasive grinding papers having a grid size of 400, 800, 1000, 2000 and 4000. The machine disc is adjusted to 300 rpm. Each grinding stage lasted for four minutes in total, and the rotation direction of the machine disc is reversed in every one minute.

Before and after the experiments, specimens are examined with Huvitz HDS-5800 digital microscope. Sample micrographs taken from the specimen Fabric 2 before and after the grinding process can be seen in Figure 3.4.
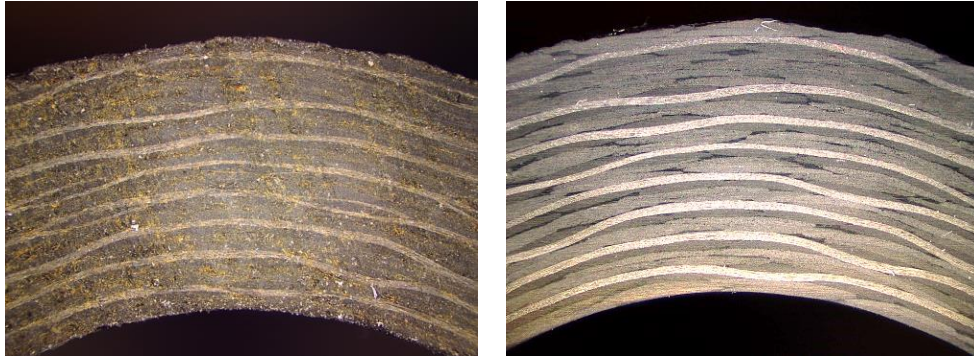
Figure 3.4. Curved region of the specimen before (left) and after (right) grinding process

In the experiments high-speed camera was used for the crack tip speed calculation and digital image correlation method. For crack tip speed calculation, the specimen surface was covered with white spray to make the crack tip visible. For digital image correlation method, unique speckle pattern over the specimen surface is needed. Thus, black paint is sprayed with airbrush to the specimen surface which was already painted with white spray.

3.1.3 Test Matrix

Test matrix is given in Table 3.9. The experiments with specimen numbers 90/0-1, 90/0-2, 90/0-3 and 90/0-5 were conducted by Uyar [28]. These experiments were recorded with high capture rate to obtain propagation of dynamic delamination in detail and calculate the crack tip speed history. The experiments with specimen numbers 90/0-6, 90/0-8 and 90/0-9 were conducted for this thesis. In the experiments 90/0-6 and 90/0-8, digital image correlation (DIC) method was used to obtain in-situ strain field. Capture rate was adjusted to 20,000 and 15,000 to obtain images having high resolution for the DIC method. In the experiment 90/0-9, dynamic delamination

is captured using high speed camera with 420k fps. For the fabric specimens, three experiments were conducted with a high speed images recorded at 420,000 fps.

Table 3.9 Test Matrix for cross-ply and fabric curved laminates showing specimen number and high speed camera information (*tests conducted by Uyar [28])

Layups	Specimen	Capture Rate	Resolution	DIC
$[(0/90)_4, \overline{90}]$	90/0-1*	465,000	64×88	No
	90/0-2*	465,000	64×88	No
	90/0-3*	465,000	64×88	No
	90/0-5*	420,000	64×96	No
	90/0-6	20,000	512×680	Yes
	90/0-8	15,000	768× 648	Yes
	90/0-9	420,000	64×96	No
$[(45/0)_7, 45/45/0/45]$	Fabric 1	420,000	64×96	No
	Fabric 2	420,000	64×96	No
	Fabric 3	420,000	64×96	No

3.1.4 Experimental Setup and Procedure

To investigate the failure of curved composite laminates under pure transverse loading, an in-house designed test fixture, shown in Figure 3.5, is used. The support plate is mounted on the rail guideway, which can move on linear rail, and the vertical arm of the curved specimen is clamped between the squeezing plate and the support plate with a bolt. The horizontal arm of the curved specimen is mounted on the freely rotating pin on the loading fixture, connected to the machine grip with bolt and nut. The loading fixture is fixed in the direction of the movement of the linear guideway. As the displacement applied on the horizontal arm increases, the loading fixture pull the vertical arm to itself. Due to the sliding movement of linear guideway on the linear rail and the pin's rotation, the load parallel to the horizontal arm is prevented,

and only the load which is transverse to the horizontal arm (pure transverse loading) is applied on the specimen.
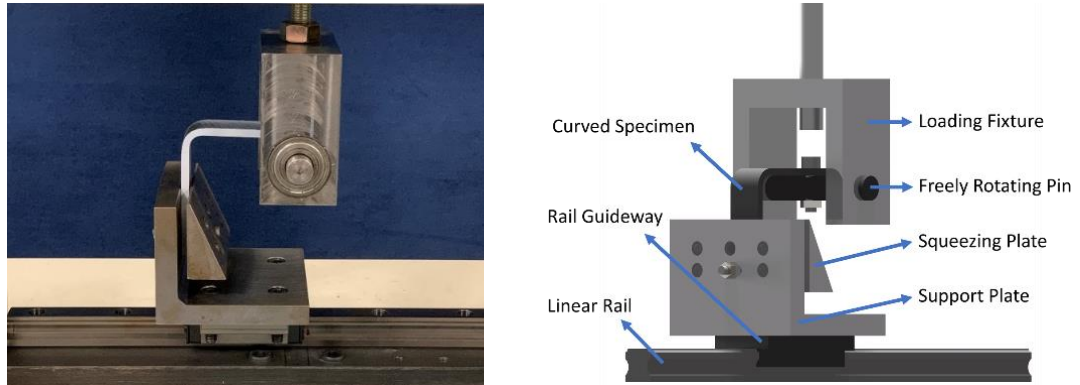
Figure 3.5. (Left) Novel test fixture designed for pure transverse loading and (Right) CAD Drawing of fixture

The experimental setup is shown in Figure 3.6. Experiments are conducted with 10 kN Shimadzu Electromechanical Test Frame. In all experiments, Photron SA5 High-speed Camera is used. In Uyar's experiments, the high-speed camera is adjusted at 420k-465k fps with a resolution of 64×96 pixels and 64×88 pixels to capture the dynamic failure. The camera trigger is adjusted to center mode where the camera saves the images from 1-2 second before and after when the trigger is pulled. In our experiments with fabric laminates, test speed is chosen as 2 mm/min. The high-speed camera images are taken with a resolution of 64×96 pixels at 420k fps by using 50 mm lens, and the camera is positioned 81,3 cm far from the specimen surface. As for our experiments with cross-ply laminates, in two experiments, in-situ strain field is obtained just before the failure event by using digital image correlation method. The high-speed camera images are taken by using 100 mm lens with 62.5 mm distance ring, and camera is positioned 41.5 cm far from the specimen surface. Before the experiment started, the image of the specimen is taken as the reference image. After the experiment started, the deformed images of the specimen are taken at every 10 seconds until the failure event. In the experiment 90/0-6, test speed is chosen as 2 mm/min and the failure event is captured at 20k fps with a resolution of 512×680 pixels. In that experiment, the movement of the specimen between the snapshots are

too large. This large movement of the specimen might lead to the high strain which makes the post-process with digital image correlation method difficult. Thus, the test speed of the specimen 90/0-8 decreases to 1 mm/min. The upper part of the specimen 90-0/6 is also out of the frame toward the end of the experiment. Thus, in the experiment 90/0-8, the resolution of the images increased by decreasing capture rate. In the experiment 90/0-9, high-speed camera is used to observe the propagation of dynamic delamination frame-by-frame. High-speed camera images are taken by using 50 mm lens with a resolution of 64×96 at 420k fps, and camera is positioned 81.5 cm far from the specimen surface.

For the post-process of DIC images, Ncorr, open source 2D Digital Image Correlation program, is used [30]. Subset radius is chosen as 20 pixels, and subset field is created in the region of interest (curved region of the specimen) with a 1 pixel overlapping. Displacement field is obtained by correlating subsets in the reference image with the deformed image. Strain field is calculated with a strain radius of 6 pixels by using displacement field. Subset radius and strain radius is chosen so that the noisy displacement and strain data can be eliminated.
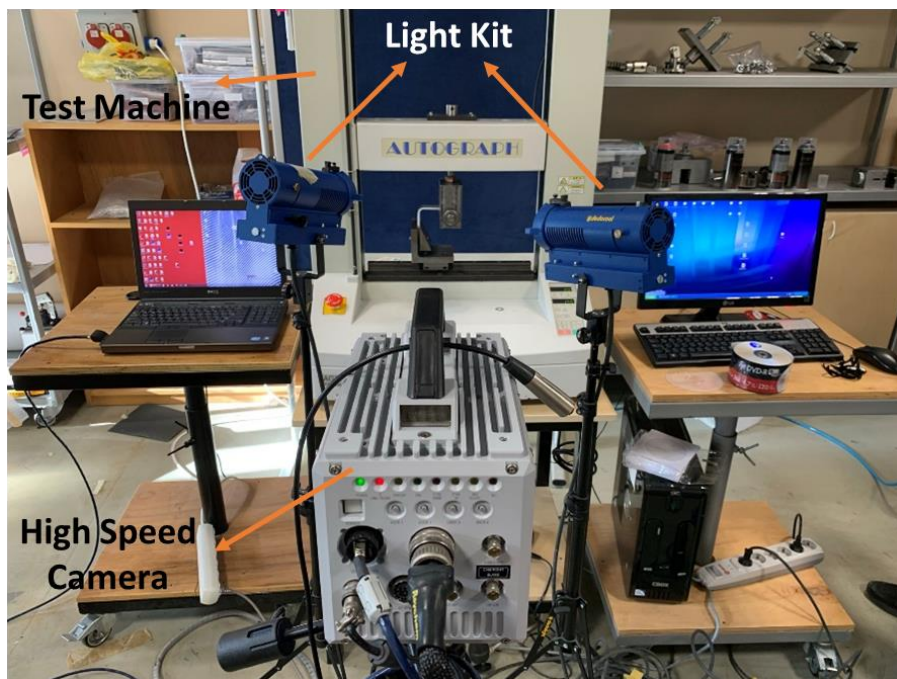
Figure 3.6. Experimental setup used in the experiments

3.2   Finite Element Method

For better understanding of the failure observed in the experiments, 2D Finite element analysis is carried out with ABAQUS\Standard. Considering the red box shown in Figure 3.7a, 2D finite element model shown in Figure 3.7b is created. According to the experimental setup, the length L_1 and L_2 are equal to 40 mm for cross-ply laminates and 27 and 67 mm for fabric laminates, respectively. To simulate loading condition reasonably, reference point is created in the bottom point of end line of the horizontal arm. This reference point is kinematically coupled with the right edge of the horizontal arm via Interaction Module in ABAQUS. Then displacement boundary condition is applied to the reference point. In the finite element model, the bottom edge of vertical arm should be free in the x-direction while the reference point is fixed in the x-direction according to the experimental boundary conditions. However, in our finite element model, these two conditions are interchanged. It means that the vertical arm is fixed while the reference point is free. This is because the relative distance between the reference point and the bottom edge of the vertical arm is important. Thus, our finite element boundary conditions also simulate the pure transverse loading.

a   b
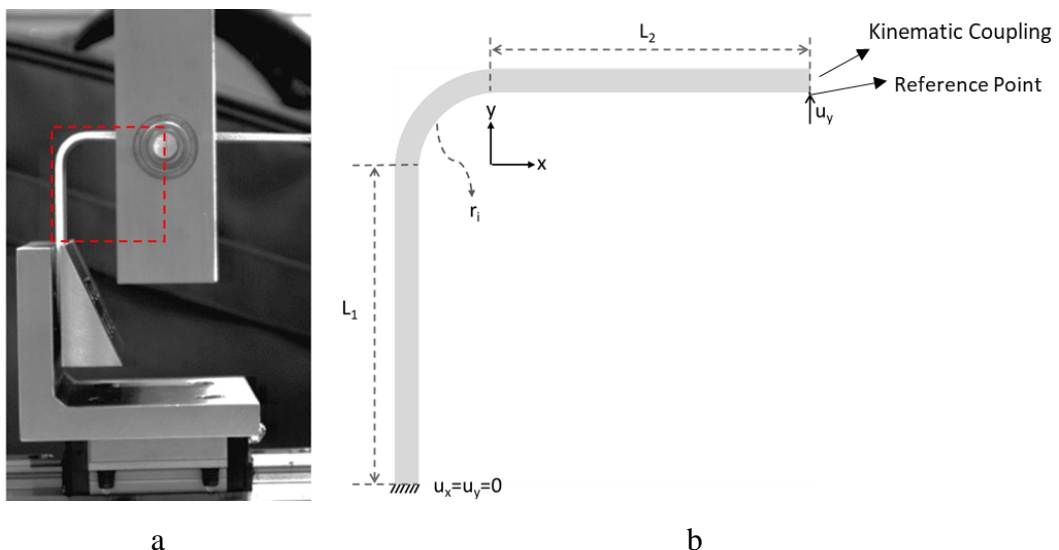
Figure 3.7. a) Experimental boundary conditions and b) 2D finite element model generated

Each ply is meshed with 2, 3, 4 and 5 elements for the mesh convergence study. As the number of mesh in which each ply is modeled increases, the mesh number of each arm and the curved region also increases proportionally. Stress distribution and load-displacement curves are compared, and it is observed that the result is approximately the same in all mesh refinement. Thus, 2 mesh per ply is used in the finite element analyses to save from the computational time. The meshed curved region is shown in Figure 3.8a-b for cross-ply and fabric curved beam, respectively. In both curved region and arms, 2 elements per ply are used. The number of mesh in tangential direction in the curved region and the arms is determined so that the elements can have an aspect ratio of 1:1. In the finite element model of cross-ply specimens, 5 elements per 3° for the curved region and 350 elements for the arms are used. In the finite element model of fabric specimens, 3 element per 3° for the curved region and 148-295 elements for the vertical and horizontal arm, respectively, is used. In the finite element model of fabric specimens 4-node bilinear plane strain quadrilateral elements with reduced integration method known as CPE4R in ABAQUS library is used for the element type. In the finite element model of cross-ply specimens, 2D Hashin Module provided by ABAQUS is used. Hashin criteria gives result for the element type with plane stress formulation. Thus, the element type is chosen as 4-node bilinear plane stress quadrilateral elements with reduced integration method (CPS4R) for the finite element model of cross-ply specimens.

89.5 µm
100 µm
5 elements per 3°
2 element per ply

(a)

140 µm
140 µm
2 element per ply
3 elements per 3°
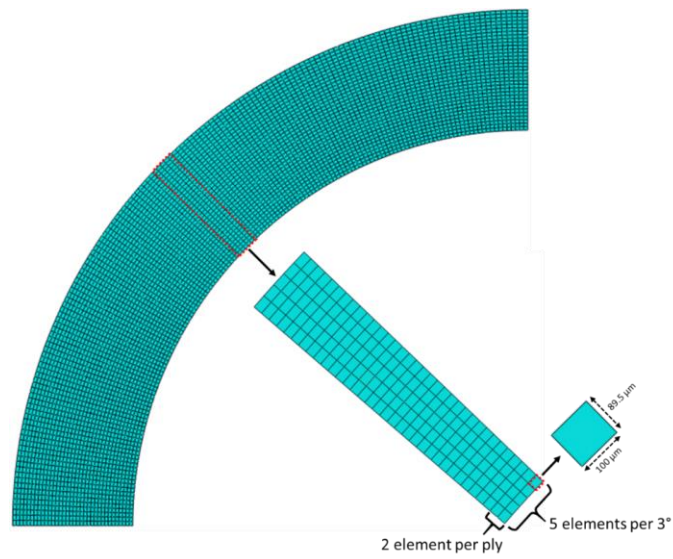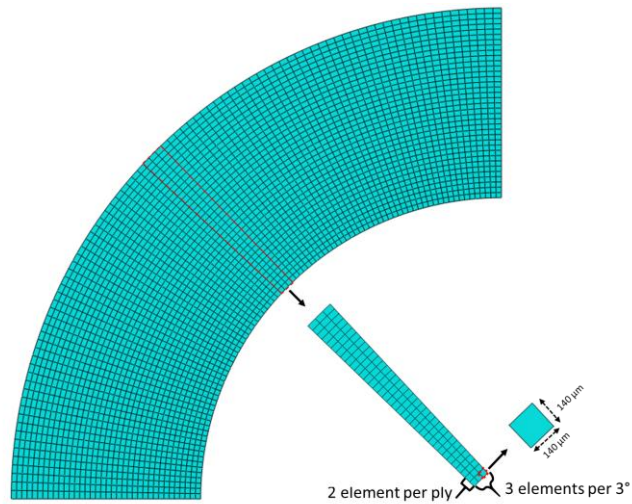
(b)

Figure 3.8. Mesh refinement in the curved region for (a) cross-ply and (b) fabric curved specimens

In addition to the models created with experimental boundary conditions, only the curved region is also modelled considering the boundary conditions with which the analytic stress field is derived. Load applied to the arm of the curved beam is transformed to the upper end of the curved region and creates a shear load and bending moment. This shear load and bending moment is applied to the curved region separately. Then the stress created by these loads are superimposed.

In addition to obtaining the stress field over the curved beam, Hashin Damage model is used to capture the tensile matrix cracks observed in the cross-ply curved composite specimens.

Hashin Failure criteria distinguish the fiber and matrix failure both in compression and tensile load. In our case, only the tensile matrix failure is crucial. This is because the high tensile stresses act on the inner region of the curvature.

In progressive Hashin failure criteria, initiation criteria for the tensile matrix crack is as follows:

Matrix Tension in 3-direction ($\sigma_{33} \geq 0$):

$$F_{m22}^t = \left(\frac{\sigma_{22}}{S_{22}^T}\right)^2 + \left(\frac{\tau_{23}}{S_T}\right)^2 \tag{3-19}$$

Matrix Tension in 3-direction ($\sigma_{33} \geq 0$):

$$F_{m33}^t = \left(\frac{\sigma_{33}}{S_{33}^T}\right)^2 + \left(\frac{\tau_{23}}{S_T}\right)^2 \tag{3-20}$$

σ_{22}^T and σ_{33}^T are stresses in the transverse direction to the fiber and thickness direction, respectively, and S_{22}^T and S_{33}^T are the material strength corresponding to these stresses, respectively. τ_{23} is the transverse shear stress, and S_T is the material strength corresponding to the transverse shear strength.

Damage evolution with the linear softening response for Hashin Damage Criteria is shown in Figure 3.9. σ_{eq}^0 and δ_{eq}^0 is the displacement and stress at which the initiation criterion is met and the damage starts. These parameters σ_{eq}^0 and δ_{eq}^0 are defined by the elastic stiffness and strength of the material. G_c is the dissipated fracture energy during the complete failure and equals the area of the triangular given in Figure 3.9. For the tensile matrix failure, it equals Mode I fracture energy which is 0.28 N/mm for our material. δ_{eq}^f is the displacement at which the elements are completely damaged. It depends on the G_c and σ_{eq}^0 and can be calculated by using the formula:

$2G_c/\sigma_{eq}^0$. Point B describes any point on the linear softening curve AC, and the damage parameter at point B can be calculated with

$$d = \frac{\delta_{eq}^f\left(\delta_{eq} - \delta_{eq}^0\right)}{\delta_{eq}\left(\delta_{eq}^f - \delta_{eq}^0\right)} \tag{3-21}$$

where

$$\delta_{eq_2} = L^c\sqrt{\langle\varepsilon_{22}\rangle^2 + \varepsilon_{23}^2}\; for\; 2-direction \tag{3-22}$$

$$\delta_{eq_3} = L^c\sqrt{\langle\varepsilon_{33}\rangle^2 + \varepsilon_{23}^2}\; for\; 3-direction \tag{3-23}$$

L^c is the characteristic length which provides a constitutive law defined as stress-displacement relation, and calculated by ABAQUS. ε_{22} and ε_{33} are strains in the transverse direction to the fiber and thickness direction, respectively. ε_{23} is the out-of-plane shear strain. Stress corresponding to displacement δ_{eq} is

$$\sigma_{eq_2} = \frac{\langle\sigma_{22}\rangle\langle\varepsilon_{22}\rangle + \tau_{23}\varepsilon_{23}}{\delta_{eq_2}/L_c} \tag{3-24}$$

$$\sigma_{eq_3} = \frac{\langle\sigma_{33}\rangle\langle\varepsilon_{33}\rangle + \tau_{23}\varepsilon_{23}}{\delta_{eq_3}/L_c} \tag{3-25}$$
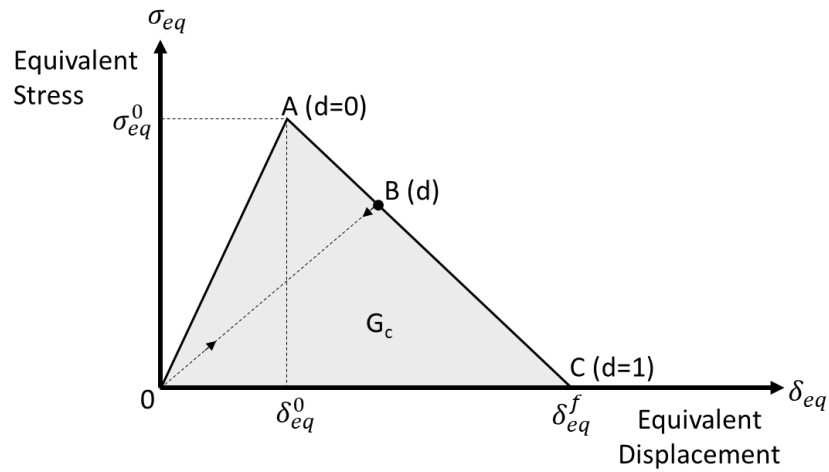
Figure 3.9. Damage Evolution in Progressive Hashin Damage [31]

41

3.3   Analytical Method

Ko and Jackson [32] proposed an analytic solution for the stress filed over the multilayered curved beam. By developing MATLAB code for the solution proposed by them, the stress field over the curved beam is obtained. The code is validated with finite element analysis, and comparison of result obtained from the analytic solution with finite element results are given in APPENDIX A.   Timoshenko [33] and Lekhnitskii [34] was also proposed a solution for the stress field in the curved beam, and the methodology used by Ko & Jackson is related with that used by Timoshenko and Lekhnitskii. Thus, the derivation of the analytic stress field solution proposed by Timoshenko, Lekhnitskii and Ko & Jackson is given in detail.

Ko & Jackson derived the stress field for two different types of load: the pure bending moment and end shear load. In addition to these types of load, the stress distribution over the curved beam under end normal load was derived by following Ko and Jackson's methodology.

In all proposed solutions, the Airy Stress Function method is used to derive the stresses over the beam. Stress and strain equations in terms of airy stress function are given below

Stress equations:

$$\sigma_r = \frac{1}{r}\frac{d\phi}{dr} + \frac{1}{r^2}\frac{d^2\phi}{d\theta^2} \tag{3-26}$$

$$\sigma_\theta = \frac{d^2\phi}{dr^2} \tag{3-27}$$

$$\tau_{r\theta} = -\frac{d}{dr}\left(\frac{1}{r}\frac{d\phi}{d\theta}\right) \tag{3-28}$$

Strain equations:

$$\varepsilon_r = \frac{du_r}{dr} = \frac{1}{E_r}\sigma_r - \frac{v_{\theta r}}{E_\theta}\sigma_\theta \tag{3-29}$$

42

$$\varepsilon_\theta = \frac{u_r}{r} + \frac{du_\theta}{rd\theta} = -\frac{v_{r\theta}}{E_r}\sigma_r + \frac{1}{E_\theta}\sigma_\theta \qquad (3\text{-}30)$$

$$\gamma_{r\theta} = \frac{du}{rd\theta} + \frac{du_\theta}{dr} - \frac{u_\theta}{r} = \frac{1}{G_{r\theta}}\tau_{r\theta} \qquad (3\text{-}31)$$

3.3.1   Timoshenko's Curved Beam Solution

Timoshenko [33] found the stress distribution over an isotropic curved beam. To estimate the airy stress function giving the stress field over the curved beam, the compatibility equation is written in polar coordinates and solved for each load case; pure bending moment and shear load. The compatibility equation in polar coordinate is expressed as

$$\left(\frac{d^2}{dr^2} + \frac{1}{r}\frac{d}{dr} + \frac{1}{r^2}\frac{d^2}{d\theta^2}\right)\left(\frac{d^2\phi}{dr^2} + \frac{1}{r}\frac{d\phi}{dr} + \frac{1}{r^2}\frac{d^2\phi}{d\theta^2}\right) = 0 \qquad (3\text{-}32)$$

Pure Bending Moment Case:

The curved beam under pure bending moment is shown in Figure 3.10. Bending moment (M) is applied to each end. r_i and r_o are the inner and outer radii of the curved beam, respectively.
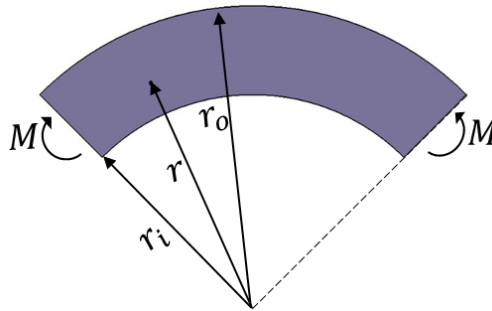
Figure 3.10. Curved beam under pure bending moment

The bending moment will be constant at each cross-section over the beam, and stress distribution does not depend on angle θ. Thus, the compatibility equation reduces to

$$\left(\frac{d^2}{dr^2} + \frac{1}{r}\frac{d}{dr}\right)\left(\frac{d^2\phi}{dr^2} + \frac{1}{r}\frac{d\phi}{dr}\right) = 0 \qquad (3\text{-}33)$$

The general solution of that differential equation will be

$$\phi = C_1 + C_2 \ln r + C_3 r^2 + C_4 r^2 \ln r \qquad (3\text{-}34)$$

Constants (C_1, C_2, C_3 and C_4) can be found by using the boundary conditions (BC) below

    i)   Radial stress in the inner and outer radii is zero;

$$\sigma_r(r_i) = 0 \text{ and } \sigma_r(r_o) = 0 \qquad \textbf{BC 1}$$

    ii)   Sum of the normal forces at the ends is zero while they create a total moment $-M$;

$$\int_{r_i}^{r_o} \sigma_\theta \, dr = 0 \text{ and } \int_{r_i}^{r_o} \sigma_\theta r \, dr = -M \qquad \textbf{BC 2}$$

    iii)   Shear stress is zero at the boundary;

$$\tau_{r\theta} = 0 \qquad \textbf{BC 3}$$

After finding the constants and inserting them into the stress equations σ_r, σ_θ and $\tau_{r\theta}$, the stress field over the curved beam under pure bending moment is obtained as

$$\sigma_r = -\frac{4M}{N}\left(\frac{r_o^2 r_i^2}{r^2}\ln\left(\frac{r_o}{r_i}\right) + r_o^2 \ln\left(\frac{r}{r_o}\right) + r_i^2 \ln\left(\frac{r_i}{r}\right)\right) \qquad (3\text{-}35)$$

$$\sigma_\theta = -\frac{4M}{N}\left(-\frac{r_o^2 r_i^2}{r^2}\ln\left(\frac{r_o}{r_i}\right) + r_o^2 \ln\left(\frac{r}{r_o}\right) + r_i^2 \ln\left(\frac{r_i}{r}\right) + r_o^2 - r_i^2\right) \qquad (3\text{-}36)$$

$$\tau_r\theta = 0 \qquad (3\text{-}37)$$

where

$$N = (r_i^2 - r_o^2)^2 - 4r_i^2 r_o^2 \left(\ln\left(\frac{r_o}{r_i}\right)\right)^2 \qquad (3\text{-}38)$$

Shear End Load Case:

The curved beam under shear load can be seen in Figure 3.11. The beam is clamped from the lower end while shear load V is applied to the upper end. r_i and r_o are inner and outer radii of the curved beam, respectively.
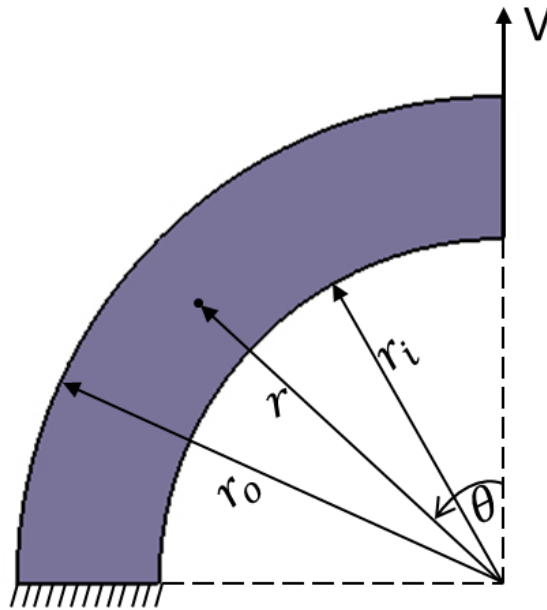
Figure 3.11. Curved beam under shear load

At each cross-section of the curved beam bending moment is proportional to $\sin\theta$, and the normal stress (or tangential stress in that case) is proportional to the bending moment based on mechanics of materials. Thus, in the curved beam under end shear load, tangential stress depends on $\sin\theta$, and this condition can be satisfied with the stress function ϕ which will be

$$\phi = f(r)\sin\theta \qquad (3\text{-}39)$$

When the stress function is inserted into the compatibility equation, the ordinary differential equation below is obtained

$$\left(\frac{d^2}{dr^2} + \frac{1}{r}\frac{d}{dr} - \frac{1}{r^2}\right)\left(\frac{d^2 f}{dr^2} + \frac{1}{r}\frac{df}{dr} - \frac{f}{r^2}\right) = 0 \tag{3-40}$$

The general solution of that ordinary differential equation will be

$$\phi = C_1 r^{-1} + C_2 r^3 + C_3 r + C_4 r \ln r \tag{3-41}$$

Constants C_1, C_2 C_3 and C_4 can be found by using the following boundary conditions:

(i)   Radial stresses at the inner and outer radii are zero

$$\sigma_r(r_i, \theta) = 0, \qquad \sigma_r(r_o, \theta) = 0 \qquad \textbf{BC 4}$$

(ii)   Sum of the shear stress at the upper end equals to the force V;

$$\int_{r_i}^{r_o} \tau_{r\theta} dr = V \qquad \textbf{BC 5}$$

(iii)   Shear stress at the inner and outer radii is zero

$$\tau_{r\theta}(r_i, \theta) = 0, \qquad \tau_{r,\theta}(r_o, \theta) = 0 \qquad \textbf{BC 6}$$

After finding the constants and inserting them into the stress equations σ_r, σ_θ and $\tau_{r\theta}$, the stress field over the curved beam under end shear load is obtained as

$$\sigma_r = \frac{V}{N}\left(r + \frac{r_i^2 r_o^2}{r^3} - \frac{r_i^2 + r_o^2}{r}\right)\sin\theta \tag{3-42}$$

$$\sigma_\theta = \frac{V}{N}\left(3r - \frac{r_i^2 r_o^2}{r^3} - \frac{r_i^2 + r_o^2}{r}\right)\sin\theta \tag{3-43}$$

$$\tau_r\theta = -\frac{V}{N}\left(r + \frac{r_i^2 r_o^2}{r^3} - \frac{r_i^2 + r_o^2}{r}\right)\cos\theta \tag{3-44}$$

where

$$N = r_i^2 - r_o^2 + (r_i^2 + r_o^2)\ln\left(\frac{r_o}{r_i}\right) \tag{3-45}$$

Normal End Load Case:

The curved beam under shear load can be seen in Figure 3.12. The beam is clamped from the lower end while normal load P is applied to the upper end. r_i and r_o are inner and outer radii of the curved beam, respectively.
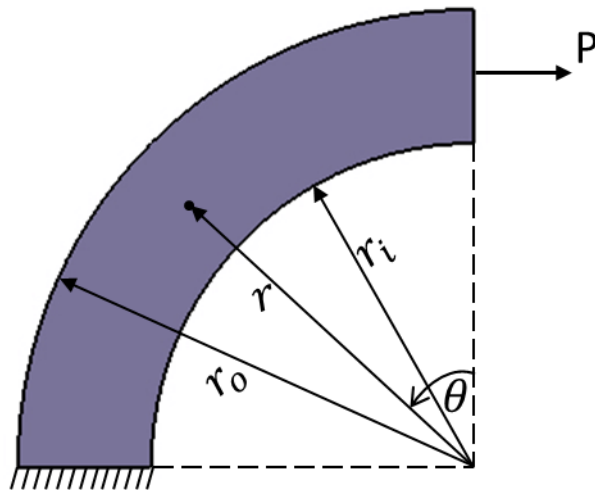
Figure 3.12. Curved beam under normal load

Timoshenko did not derive the stress expressions explicitly for that case but did explain how to obtain the stress field. Stress function ϕ in the form of

$$\phi = f(r) \cos \theta \tag{3-46}$$

gives the stresses on the curved beam under both normal end load P and bending moment M. By subtracting the solution of pure bending moment case from the solution obtained by that stress function, stresses for the curved beam under normal end load can be obtained.

3.3.2   Lekhnitskii's Curved Beam Solution

Lekhnitskii [34] derived the stress field over an anisotropic curved beam under pure bending moment, end shear load and end normal load.

Pure Bending Moment Case:

For an anisotropic curved beam, the compatibility equation in terms of airy stress function is written as

$$
\begin{aligned}
a_{22}\frac{d^4\phi}{dr^4} &- 2a_{26}\frac{1}{r}\frac{d^4\phi}{dr^3\,d\theta} + (2a_{12}+a_{66})\frac{1}{r^2}\frac{d^4\phi}{dr^2\,d\theta^2} - 2a_{16}\frac{1}{r^3}\frac{d^4\phi}{dr\,d\theta^3} \\
&+ a_{11}\frac{1}{r^4}\frac{d^4\phi}{d\theta^4} + 2a_{22}\frac{1}{r}\frac{d^3\phi}{dr^3} - (2a_{12}+a_{66})\frac{1}{r^3}\frac{d^3\phi}{dr\,d\theta^2} \\
&+ 2a_{16}\frac{1}{r^4}\frac{d^3\phi}{d\theta^3} - a_{11}\frac{1}{r^2}\frac{d^2\phi}{dr^2} - (2a_{16}+a_{26})\frac{1}{r^3}\frac{d^2\phi}{dr\,d\theta} \\
&+ (2a_{11}+2a_{12}+a_{66})\frac{1}{r^4}\frac{d^2\phi}{d\theta^2} + a_{11}\frac{1}{r^3}\frac{d\phi}{dr} \\
&+ 2(a_{16}+a_{26})\frac{1}{r^4}\frac{d\phi}{d\theta} = 0
\end{aligned}
\tag{3-47}
$$

In pure bending case, airy stress function F does not depend on θ. Thus, the compatibility equation reduces to

$$
a_{22}\frac{d^4\phi}{dr^4} + 2a_{22}\frac{1}{r}\frac{d^3\phi}{dr^3} - a_{11}\frac{1}{r^2}\frac{d^2\phi}{dr^2} + a_{11}\frac{1}{r^3}\frac{d\phi}{dr} = 0
\tag{3-48}
$$

and general solution of this ordinary differential equation will be

$$
F(r) = C_1 + C_2 r^{1+\sqrt{a_{11}/a_{22}}} + C_3 r^{1-\sqrt{a_{11}/a_{22}}} + c_4 r^2
\tag{3-49}
$$

After finding the constants by using the same boundary conditions BC 1, BC 2 and BC 3 as Timoshenko's solution, stresses are obtained as

$$
\sigma_r = -\frac{M}{gr_o^2}\left[1 - \frac{1-c^{k+1}}{1-c^{2k}}\left(\frac{r}{b}\right)^{k-1} - \frac{1-c^{k-1}}{1-c^{2k}}\left(\frac{b}{r}\right)^{k+1}c^{k+1}\right]
\tag{3-50}
$$

$$
\sigma_\theta = -\frac{M}{gr_o^2}\left[1 - \frac{1-c^{k+1}}{1-c^{2k}}k\left(\frac{r}{b}\right)^{k-1} + \frac{1-c^{k-1}}{1-c^{2k}}k\left(\frac{b}{r}\right)^{k+1}c^{k-1}\right]
\tag{3-51}
$$

$$\tau_{r\theta} = 0 \qquad (3\text{-}52)$$

where

$$k = \sqrt{a_{11}/a_{22}} = \sqrt{E_\theta/E_r} \qquad (3\text{-}53)$$

$$c = r_i/r_o \qquad (3\text{-}54)$$

$$g = \frac{1-c^2}{2} - \frac{k}{k+1}\frac{(1-c^{k+1})^2}{1-c^{2k}} + \frac{kc^2}{k-1}\frac{(1-c^{k-1})^2}{1-c^{2k}} \qquad (3\text{-}55)$$

End Load Case:

The curved beam under end load, P, can be seen in Figure 3.13. α is the angle between the load P and its shear load component.
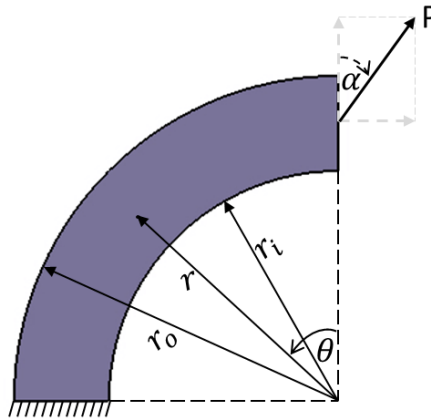
Figure 3.13. Curved beam under normal and shear load

For normal and shear load components of the end load P, stress functions $\phi_1(r)\cos\theta$ and $\phi_2(r)\sin\theta$[1] are proposed. Then, stresses created by the end load P are found by superimposing the solutions obtained from these airy stress functions.

---

[1] As it was said by Timoshenko's, that stress function gives the stress field result from end normal load and its coupled moment, not only end normal load.

To find the form of airy stress function, the compatibility equation used in pure bending moment case is rewritten for an orthotropic material

$$\frac{1}{E_\theta}\frac{d^4\phi}{dr^4} + \left(\frac{1}{G_{r\theta}} - \frac{2v_r}{E_r}\right)\frac{1}{r^2}\frac{d^4\phi}{dr^2 d\theta^2} + \frac{1}{E_r}\frac{1}{r^4}\frac{d^4\phi}{d\theta^4} + \frac{2}{E_\theta}\frac{1}{r}\frac{d^3\phi}{dr^3}$$

$$- \left(\frac{1}{G_{r\theta}} - \frac{2v_r}{E_r}\right)\frac{1}{r^3}\frac{d^3\phi}{drd\theta^2} - \frac{1}{E_r}\frac{1}{r^2}\frac{d^2\phi}{dr^2}$$

$$+ \left(2\frac{1-v_r}{E_r} + \frac{1}{G_{r\theta}}\right)\frac{1}{r^4}\frac{d^2\phi}{d\theta^2} + \frac{1}{E_r}\frac{1}{r^3}\frac{d\phi}{dr} = 0$$

(3-56)

The ordinary differential equation above is solved for each airy stress function, and the general solution is found as

$$\phi = \phi_1(r)\cos\theta + \phi_2(r)\sin\theta = (C_1 r + C_2 r^{1+B} + C_3 r^{1-B} +$$

$$C_4 r \ln r)\cos\theta + (C_1' r + C_2' r^{1+B} + C_3' r^{1-B} + C_4' r \ln r)\sin\theta$$

(3-57)

where

$$B = \sqrt{1 + \frac{E_\theta}{E_r}(1 - 2v_r) + \frac{E_\theta}{G_{r\theta}}}$$

(3-58)

The constants C_1, C_2, C_3 and C_4 are found by using the same boundary conditions **BC 4**, **BC 5** and **BC 6** as Timoshenko's solution. To find the constants C_1', C_2', C_3' and C_4', boundary condition at the end where load is applied is rewritten as

$$\int_{r_i}^{r_o} \sigma_\theta \, dr = P$$

(3-59)

and other boundary conditions are identical with **BC 4** and **BC 5** in the shear load case.

After finding the constants, stresses are obtained as

$$\sigma_r = \frac{P}{gr}\left[\left(\frac{r}{r_o}\right)^B + c^B\left(\frac{b}{r}\right)^B - 1 - c^B\right]\sin(\theta + \alpha)$$

(3-60)

$$\sigma_\theta = \frac{P}{gr}\left[(1+B)\left(\frac{r}{b}\right)^B + (1-B)\left(\frac{b}{r}\right)^B c^B - 1 - c^B\right]\sin(\theta + \alpha)$$

(3-61)

$$\tau_{r\theta} = -\frac{P}{gr}\left[\left(\frac{r}{b}\right)^B + (c^B)\left(\frac{b}{r}\right)^B - 1 - c^B\right]\cos(\theta + \alpha)$$ (3-62)

Where

$$c = r_i/r_o$$ (3-63)

$$g = \frac{2}{B}(1 - c^B) + (1 + c^B)\ln c$$ (3-64)

In the solution proposed by Lekhnitskii, k and B are the anisotropy parameters. These parameters give the correct stress field for the one-plied layup or the layup where all plies are oriented in the same direction.

3.3.3 Ko and Jackson's Curved Beam Solution

Ko and Jackson [32] applied Lekhnitskii's methodology to each layer of the multilayered curved beam by considering the interface boundary conditions (or continuity of stresses and displacements at the interfaces). As shown in Figure 3.14, stresses are derived for a semicircular curved beam under bending moment and end shear load. r_i and r_o are inner and outer radii of the curved beam, respectively.

Figure 3.15 shows the n-layered curved composite part. r^i indicates the radial locations. For $i = 0$ and $i = n$, radial locations are inner radius and outer radius, respectively, and other i values (1, ... n-1) show the interfaces between plies. As shown in Figure 3.15, stresses and displacements of plies are the same at the ith interface.
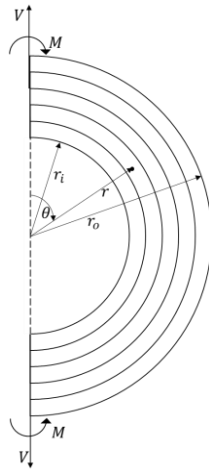
Figure 3.14. Curved beam under pure bending moment

$$\sigma_r^i\left(r^i,\theta\right) = \sigma_r^{i+1}\left(r^i,\theta\right)$$
$$\tau_{r\theta}^i\left(r^i,\theta\right) = \tau_{r\theta}^{i+1}\left(r^i,\theta\right)$$
$$u_r^i\left(r^i,\theta\right) = u_r^{i+1}\left(r^i,\theta\right)$$
$$u_\theta^i\left(r^i,\theta\right) = u_\theta^{i+1}\left(r^i,\theta\right)$$
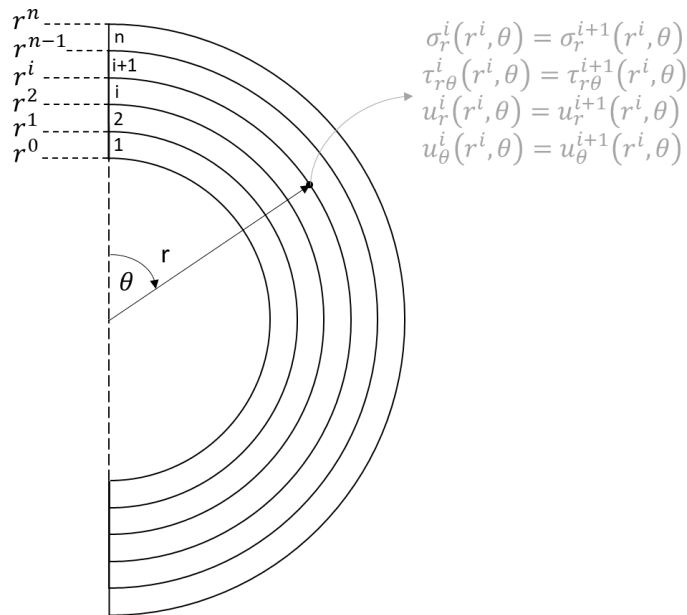
Figure 3.15. Boundary conditions and notations used in multilayered theory

Pure Bending Moment Case:

Stress function proposed by Lekhnitskii's, ϕ is used to obtain stresses

$$\phi(r) = C_1 + C_2 r^{1+k} + C_3 r^{1-k} + C_4 r^2 \tag{3-65}$$

where

$$k = \sqrt{a_{11}/a_{22}} = \sqrt{E_\theta/E_r} \tag{3-66}$$

For that stress function, constant C_1 will vanish from all stress and displacement equations, and these equations will depend on the constant, C_2, C_3 and C_4. For n-th layer curved beam, $n * 3$ unknowns must be found. The boundary conditions to find these $3n$ unknowns are

i)   For $i = 0$ and $i = n$, radial stress at the inner and outer radii are zero

$$\sigma_r(r_i) = 0, \quad \sigma_r(r_o) = 0 \qquad \textbf{BC 7}$$

ii)   For i=1, 2 … (n-1), at the interfaces, radial stress, radial displacement and tangential displacement of the adjacent plies are identical

$$\begin{aligned}
\sigma_r^i(r^i) &= \sigma_r^{i+1}(r^i) \\
u_r^i(r^i) &= u_r^{i+1}(r^i) \\
u_\theta^i(r^i) &= u_\theta^{i+1}(r^i)
\end{aligned} \qquad \textbf{BC 8}$$

iii)   Sum of the normal forces at the ends are zero while they create a total moment $-M$;

$$\sum_{i=1}^{n} \int_{r_{i-1}}^{r_i} (r - r_0)\sigma_\theta^i(r)dr = \sum_{i=1}^{n} \int_{r_{i-1}}^{r_i} r\sigma_\theta^i(r)dr = -M \qquad \textbf{BC 9}$$

where r_0 is the neutral axis of the curved beam.

By solving system of equations consisting of 3n equations, the constants C_2, C_3 and C_4 for each layer are found, and stresses are obtained.

End Shear Load Case:

For end shear load case, the stress function proposed by Lekhnitskii is used

$$F = (C_1 r + C_2 r^{1+B} + C_3 r^{1-B} + C_4 r \ln r) \sin \theta \tag{3-67}$$

where

$$B = \sqrt{1 + \frac{E_\theta}{E_r}(1 - 2v_{r\theta}) + \frac{E_\theta}{G_{r\theta}}} \qquad (3\text{-}68)$$

C_1 will vanish from all stress and displacement equations, and the boundary conditions used to find the $3n$ unknowns will be

i)   For $i = 0$ and $i = n$, radial stress and shear stress at the inner and outer radii are zero

$$\sigma_r(r_i, \theta) = 0 \text{ and } \tau_{r\theta}(r_i, \theta) = 0 \qquad \textbf{BC 10}$$
$$\sigma_r(r_o) = 0 \text{ and } \tau_{r\theta}(r_o, \theta) = 0$$

ii)   For i=1, 2 … (n-1), at the interfaces, radial stress, shear stress, radial displacement and tangential displacement of the adjacent plies are identical

$$\sigma_r^i(r^i, \theta) = \sigma_r^{i+1}(r^i, \theta) \text{ and } \tau_{r\theta}^i(r^i, \theta) = \tau_{r\theta}^{i+1}(r^i, \theta)$$
$$u_r^i(r^i, \theta) = u_r^{i+1}(r^i, \theta) \qquad \textbf{BC 11}$$
$$u_\theta^i(r^i, \theta) = u_\theta^{i+1}(r^i, \theta)$$

iii)   The sum of the shear forces at the ends equals to the -V;

$$\sum_{i=1}^{N} \int_{r_{i-1}}^{r_i} \tau_{r\theta}^i(r, 0)dr = -V \qquad \textbf{BC 12}$$

Radial stress and shear stress equations are identical to each other in terms of r. Thus, when one stress equation is satisfied, the other stress equation is also satisfied.

When the system of equation consisting of the boundary conditions above is solved, the constants C_2, C_3 and C_4 for each layer are found, and stresses are obtained.

3.3.4   Stress Distribution over the Curved Beam under End Normal Load

Stress distribution over the curved beam under end normal load shown in Figure 3.12 is derived by using the stress function ϕ proposed by Timoshenko

$$\phi = f(r) \cos \theta \qquad (3\text{-}69)$$

As it was mentioned in Chapter 3.3.1, this stress function gives the stress field created by end normal load P and its coupled moment M. Thus, stresses created by the couple moment are subtracted from the ones obtained by using stress function ϕ. The couple moment M is equal to

$$P\left(\frac{r_i + r_o}{2}\right) \qquad (3\text{-}70)$$

according to ESDU [35].

The constants C_1, C_2, C_3 and C_4 are found by using the same boundary conditions **BC 4**, **BC 5** and **BC 6** as Timoshenko's solution. To find the constants C_1', C_2', C_3' and C_4', boundary condition at the end where load is applied is rewritten as

The methodology used by Ko and Jackson is followed to derive the stresses. The boundary conditions **BC 10** and **BC 11** is used in conjunction with the below end normal load boundary condition

$$\sum_{i=1}^{N} \int_{r_{i-1}}^{r_i} \sigma_\theta^i(r, 0) dr = P \qquad (3\text{-}71)$$

CHAPTER 4

RESULTS FOR CROSS-PLY CURVED COMPOSITE LAMINATES

4.1 Experimental Results

Load-displacement curves obtained from the experiments are given in Figure 4.1. In the experiments 90/0-1, 90/0-3 and 90/0-5, multiple load drops are observed. In these experiments, one or two delamination occurs simultaneously at one load drop. After each load drop, the stiffness of the specimens decreases. In the experiment 90/0-6, 90/0-8 and 90/0-9, more than three delaminations occur simultaneously at one load drop. Thus, specimens lose their load carrying capacity at single load drop. The experiment of specimen 90/0-6 is stopped after the first failure. An additional delamination occurred before the specimen is not unloaded yet. In the experiments, crackling sounds are heard during the loading, and increases as the loading increases. In the experiment 90/0-9, high crackling sound which leads to small load drop is heard. Load-displacement data could not be taken from the experiment 90/0-2.

In all of the load-displacement curves, non-linear behavior is observed because excessive displacement which leads to increase in the angle of the curved region so much as shown in Figure 4.2. The load-displacement curve obtained from finite element analysis (FEA) is also drawn with the black dashed line. There is no load drop seen in FEA since delamination is not simulated in the analysis.

The failure loads and the displacement corresponding to the first failure load are given in Table 4.1. The specimens where multiple load drops are observed reach 76-82 % of their first failure load. The 3rd failure in specimen 90/0-3 occurs at 324 N, which exceeds the previous failure load of 318 N. High load drop of 321 N occurs in the specimen 90/0-1 after the 3rd failure. This high load drop is attributed to two delaminations occurring sequentially during the course of the load drop.
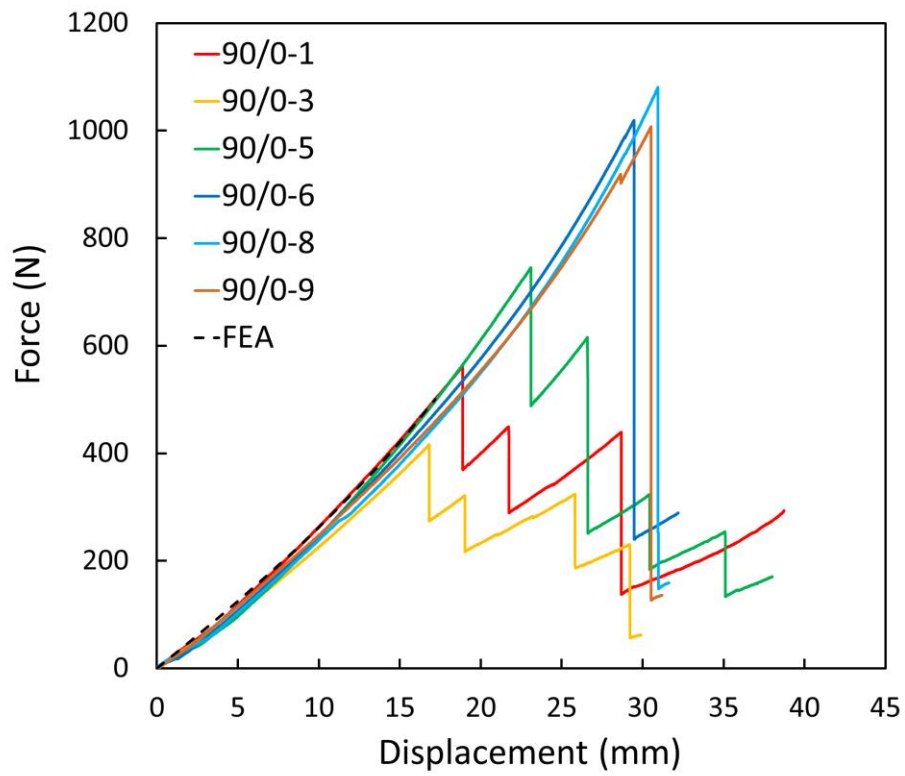
Figure 4.1. Load displacement curve obtained from experiments and finite element analysis (FEA).
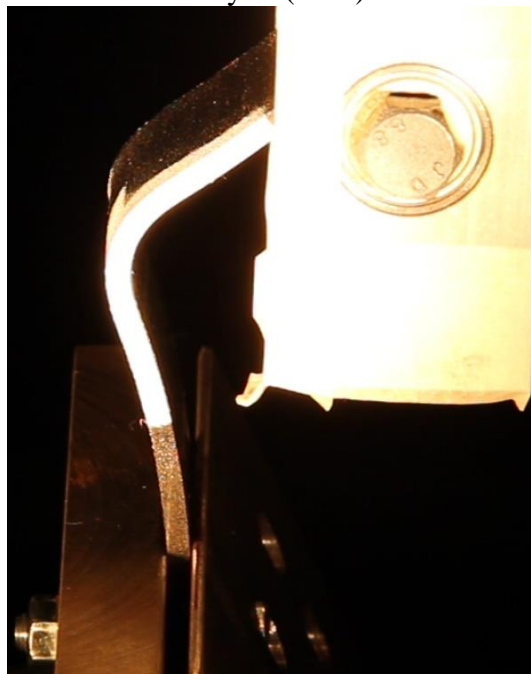
Figure 4.2. The image of the specimen 90/0-6 just before the failure.

The average of the first failure load of the specimen where multiple load drops occur is 574 N while that of the specimen where multiple delaminations occur in a single load drop is 967 N.

Table 4.1 Displacement ($\delta_{failure}$) corresponding to 1st failure load and failure loads of cross-ply curved composite laminates.

Specimen	$\delta_{failure}$ (mm)	1st Failure Load (N)	2nd Failure Load (N)	3rd Failure Load (N)	4th Failure Load (N)
90/0-1	18.9	562	450	439	
90/0-3	16.8	416	317	324	226
90/0-5	23.1	745	614	322	254
90/0-6	29.5	1020			
90/0-8	30.9	806			
90/0-9	31.0	1081			

4.1.1   In-situ High-speed Camera Images and The Crack Tip Speeds

In the specimen 90/0-5, multiple load drops are observed. High-speed camera images corresponding to these load drops are shown in Figure 4.3. After the first load drop, the experiment is paused, and high-speed camera images are taken. Then, the camera is readjusted for the 2nd load drop. The procedure repeated for each load drop. The radial black line in the images helps us to distinguish the angular position of the point where the crack nucleates. The 1st picture of each load drop shows just before the onset of crack nucleation. 2nd & 3rd pictures are taken the 4.76 μs & 9.52 μs after the crack nucleation. It is observed that the first failure occurs in the inner ply of the curved region, and subsequent failures occur in the outer plies in order as the displacement applied on the horizontal arm increases.
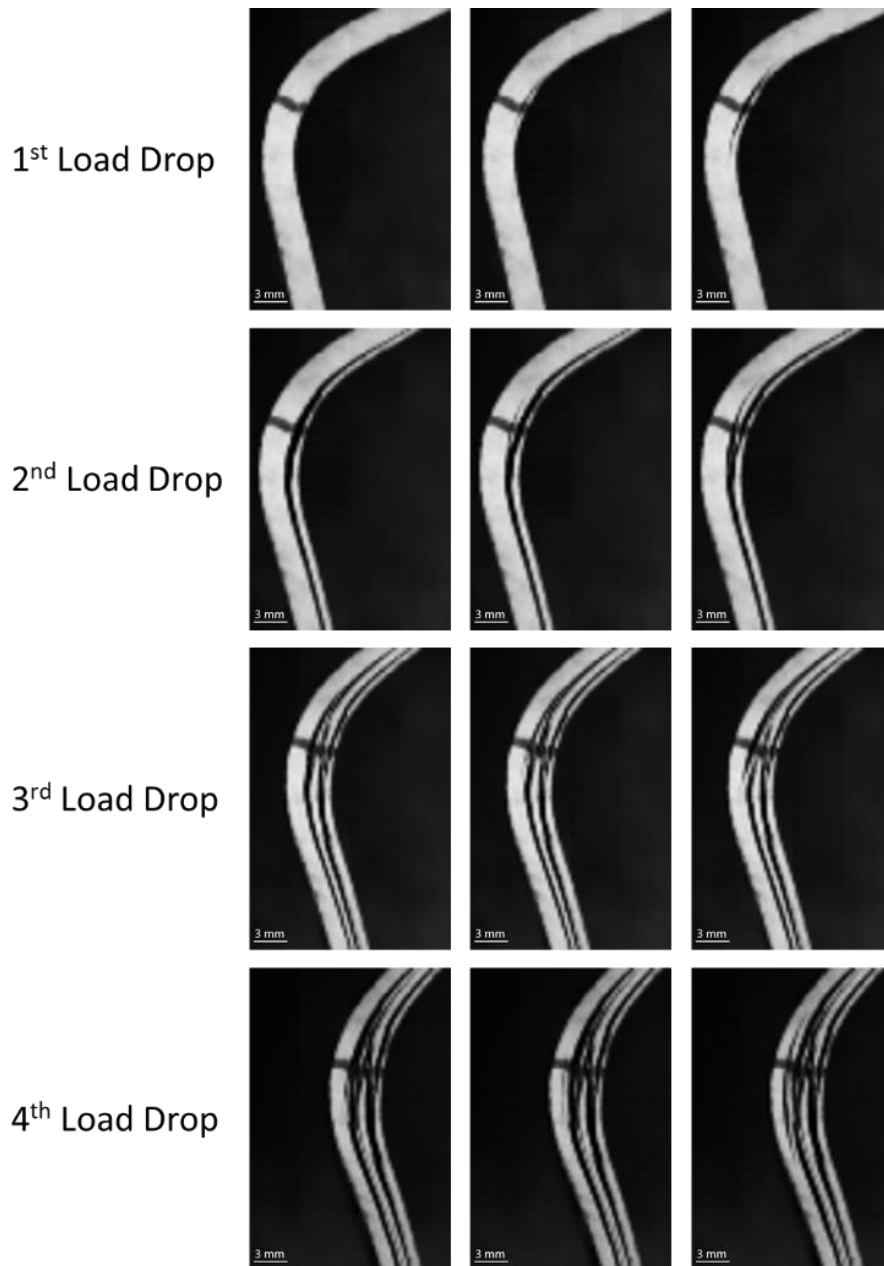
Figure 4.3. High-speed camera images corresponding to load drops observed in the cross-ply specimen 90/0-5.

In the specimen 90/0-9, four delaminations occur sequentially in a single load drop, and the high-speed camera images correspond to these delaminations are shown in Figure 4.4. The 1st pictures at each row of Figure 4.4 shows just before the onset of delamination. The 2nd, 3rd and 4th delaminations occur after 7.14 µs, 28.57 µs and 83.33 µs than the initiation of 1st delamination, respectively. As it was observed in

the experiment 90/0-5, the failure location moves from the inner side to the outer side of the curved region.
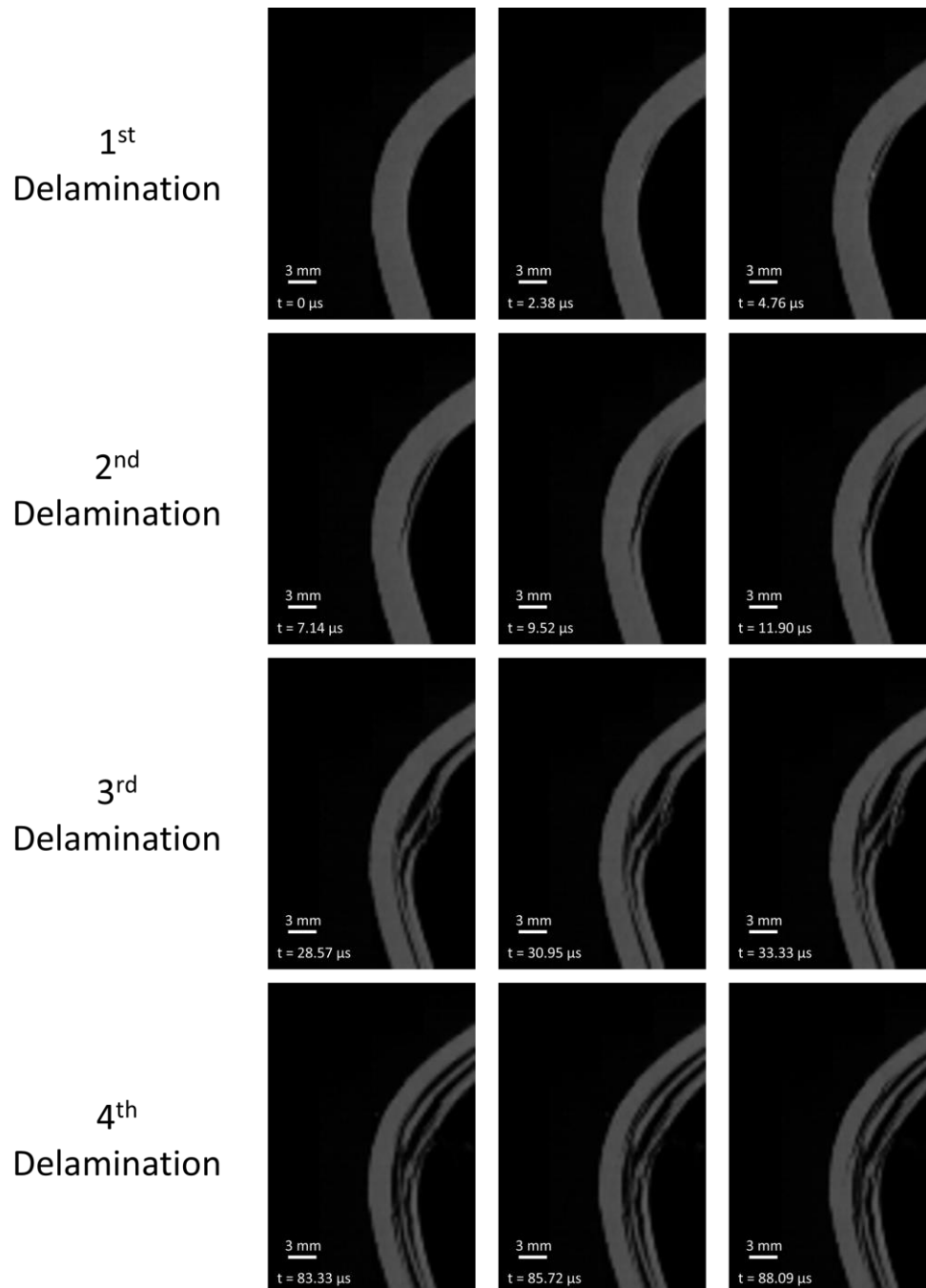
Figure 4.4. High-speed camera images corresponding to sequential delaminations occurring during the course of the load drop in the cross-ply specimen 90/0-9.

High-speed camera pictures obtained during the first load drop in specimen 90/0-5 are shown in Figure 4.5. In the experiment, the capture rate is 420,000 fps. The interframe time is 2.38 μs. In the first picture, failure is not yet started. The crack then initiates in the curved region and propagates through the vertical and horizontal arms. Crack tips are pointed out with red arrows.
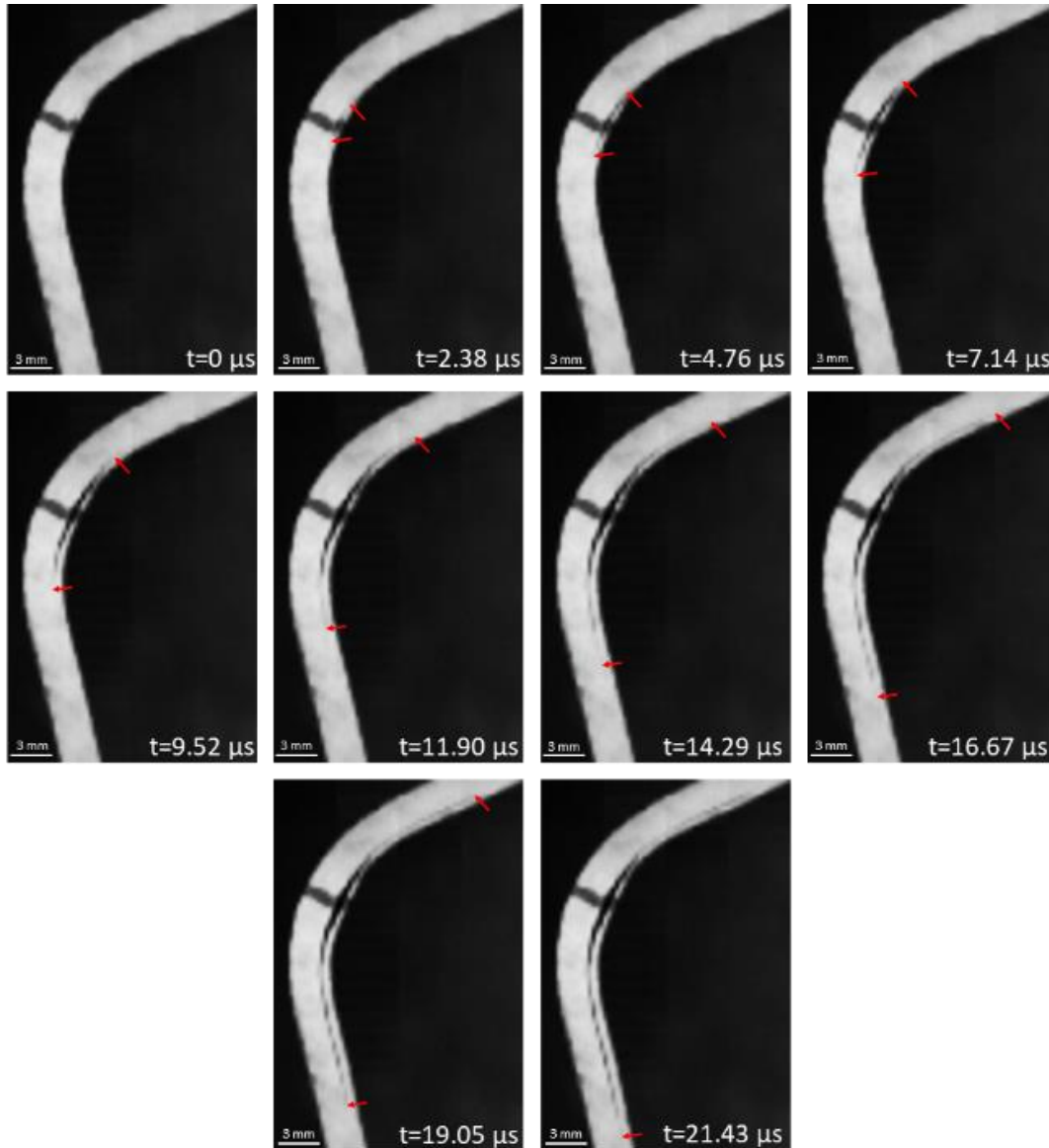
Figure 4.5. Propagation of the crack during the first load drop for the cross-ply specimen 90/0-5

The crack tip speeds are calculated with the high-speed camera images obtained during the first load drop. The crack nucleation point could not be captured. Thus, it is taken as the mid-point of the crack tips at t=2.38 μs. The crack tip positions are calculated in the unit of the pixel. Then by calibrating vertical arm length, the length of the pixels is found, and crack tip positions are converted to millimeters.

The crack tip position of the lower and upper crack tips are shown in Figure 4.6a-b, respectively. The crack tip speeds, shown in Figure 4.6c-d, are calculated by using the central difference method to the crack tip positions. The last speed data, however, is calculated by using the backward difference method.

The trend of upper crack tip speeds obtained in both experiments 90/0-2 and 90/0-5, are similar to each other. In these experiments, upper crack initiates with a speed of 905 m/s and 570 m/s, respectively. Then in both experiments, the crack slows down to 478 m/s within 4.76 μs and 8.60 μs, respectively. Afterwards, the crack accelerates and reaches the maximum speeds of 1363 m/s and 1104 m/s at the time of 15.05 μs and 11.90 μs. Then the crack tip speed starts to slow down, and this indicates the crack will probably be arrested in the horizontal arm. As for the lower crack tip, in both experiments 90/0-2 and 90/0-5, it initiates with a speed of around 525 m/s and propagates with that speed for 2.38 μs. Then the crack tip speeds up to 1147 m/s at the time of 8.60 μs in the experiment 90/0-2 and 1188 m/s at the time of 11.90 μs in the experiment 90/0-5. After that point, the trend of the crack tip speed in the experiments differentiates from each other. In the experiment 90/0-2, lower crack tip speed slows down by 120 m/s then speeds up to 1676 m/s, which is slightly more than Rayleigh wave speed, i.e., 1652 m/s. In the experiment 90/0-5, 1188 m/s is the maximum speed that crack tip reaches. Afterwards the crack tip speed slows down 830 m/s then speeds up to 1014 m/s.
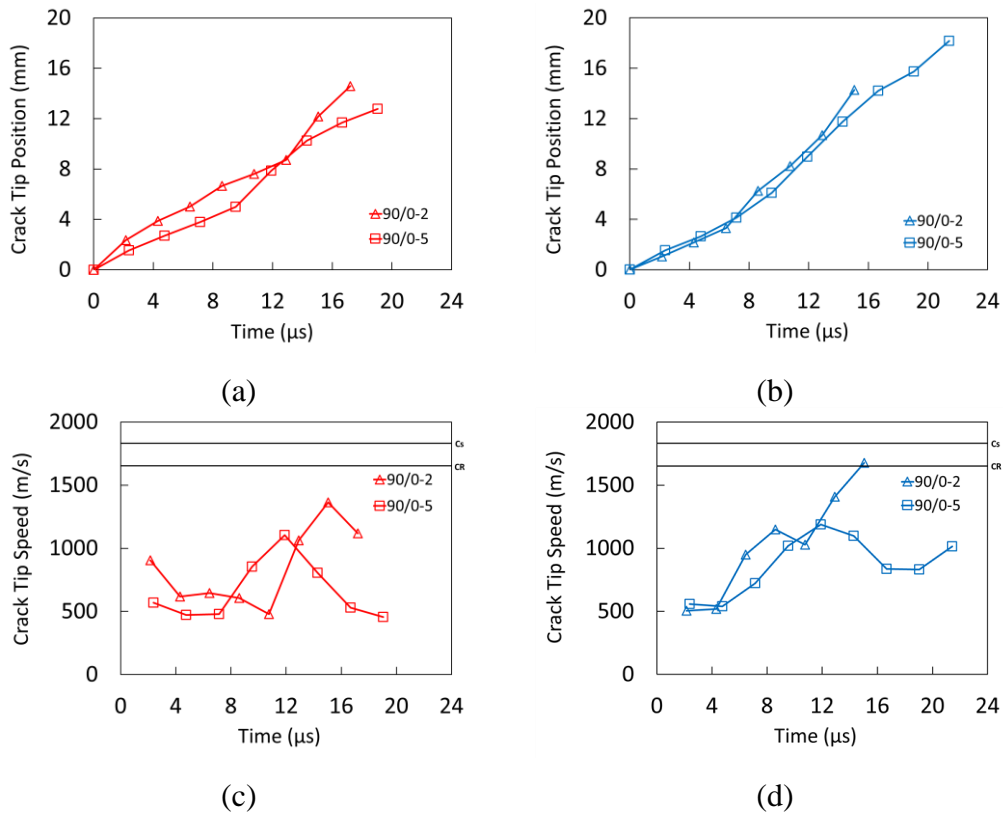
Figure 4.6. Crack tip position and speed history for cross-ply laminates: (a) upper crack tip position, (b) lower crack tip position, (c) upper crack tip speed, (d) lower crack tip speed

4.1.2   Digital Image Correlation Results

In the load-displacement curve of experiment 90/0-8, six displacement values are indicated as letters a, b, c, d, e and f as shown in Figure 4.7. Von Mises strain field, independent from the coordinate system, is calculated with digital image correlation method and is given in Figure 4.8. The letters of the figure correspond to the letters shown in load-displacement curve.

At the displacement of 6.7 mm (Figure 4.8a), light-blue spot (~6530 µstrain) is observed in the inner side of the curve region. As the displacement increases to 13.33 mm (Figure 4.8b), three more spots, two of them in the outer side of the curve region and one of them in the inner side of the curve region, are also observed. As the displacement increases, strain concentration at these spots is getting clearer. (Figure

64

4.8c-d). At the displacement value of 28.3 mm (Figure 4.8e), high strain concentration occurs at the lower spot in the inner side of the curved region as 22400 μstrain. Just before the failure (Figure 4.8f), higher strain concentration of 29500 μstrain occurs in the upper spot in the inner side of the curved region.
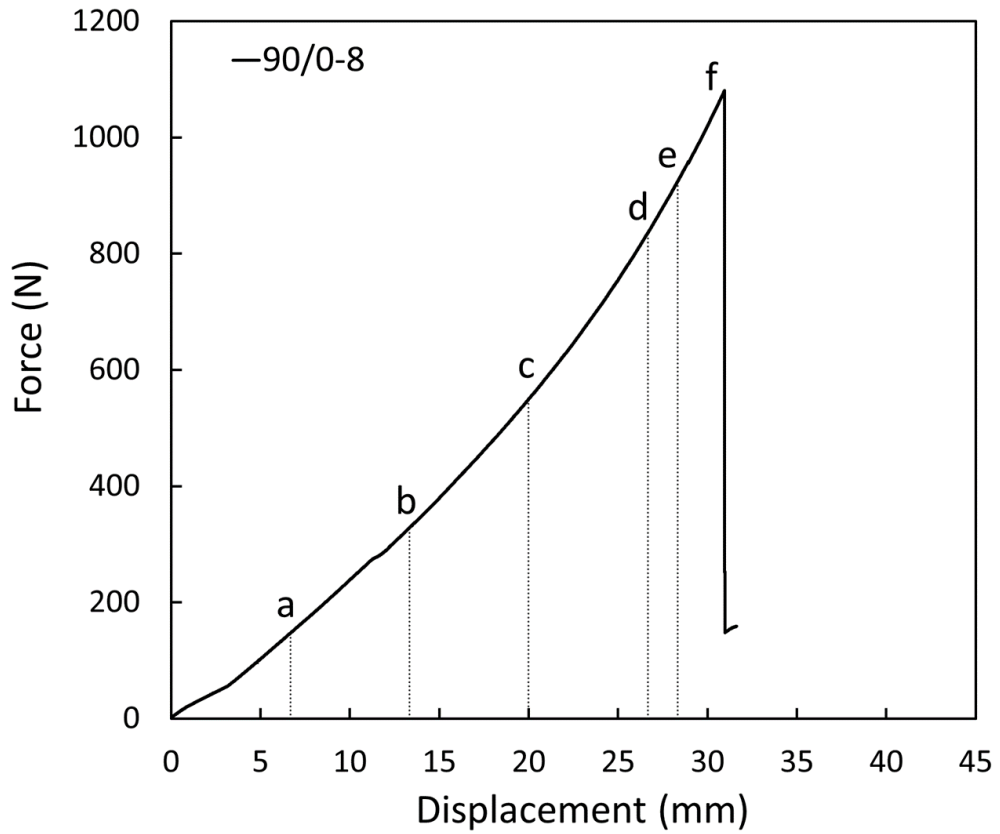
Figure 4.7. Six displacement values indicated at the load-displacement curve of experiment 90/0-8.
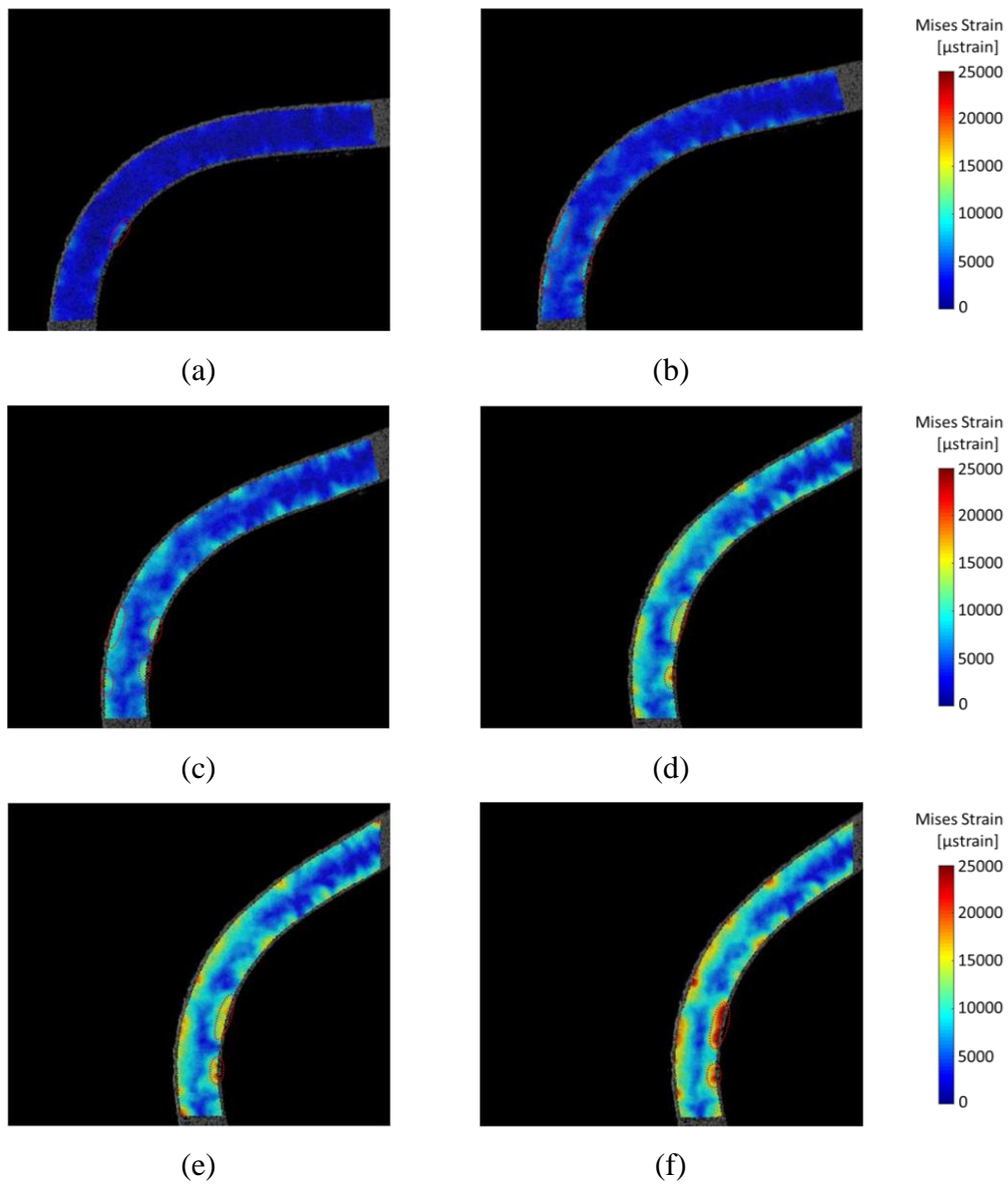
Figure 4.8. Von Mises strain field over the curved region of specimen 90/0-8 at six displacement values of (a) 6.67 mm, (b) 13.3 mm, (c) 20 mm, (d) 26.7 mm, (e) 28.3 mm and (f) 30.1 mm

In Figure 4.9a-b, von Mises strain field just before the failure (Figure 4.8f) and high-speed camera images just after the failure are given for the specimen 90/0-8. In the experiment, capture rate is 15000 fps. Thus, the initiation location of the dynamic delamination failure could not be captured with high speed camera. The red spots in

the inner side of the curve region shown in the von Mises strain field coincide approximately with the failure region.
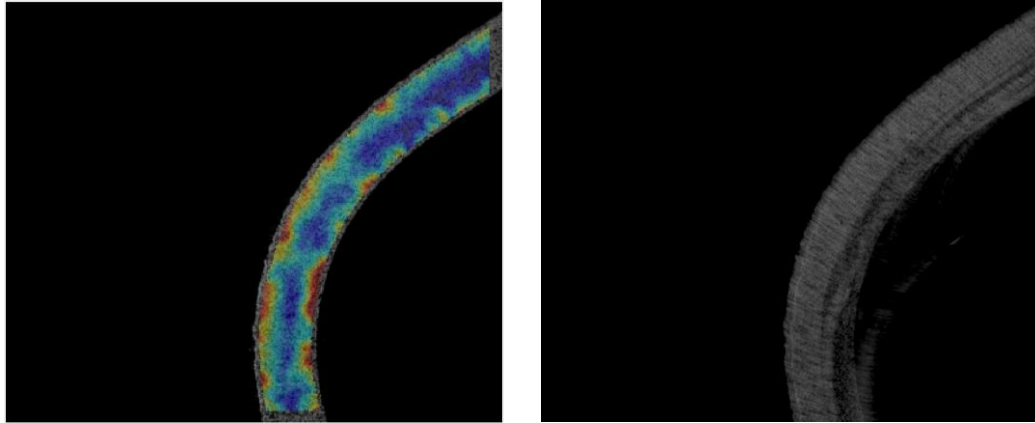
Figure 4.9. (a) von Mises strain field just before the failure and (b) High-speed camera images just after the failure

Von Mises strain distribution is taken from through-the-thickness section of θ=45°, shown in Figure 4.10, for six different displacement values. Comparison of these strain distribution is given in Figure 4.11. In the displacement value of 5 mm, the specimen is not loaded so much, and this might lead to the high noisy data in the digital image correlation method. Thus, the strain field at that displacement value misleads the general trend of the through-the-thickness von Mises strain distribution. Except for the strain field at the displacement of 5 mm, von Mises strain increases as the displacement increases. At all displacement values, von mises strain at the inner side is higher than that of the outer side, and strain decreases to the mid-section of thickness. Von Mises strain at the inner side increases from 0.012 mm/mm to 0.023 mm/mm as the displacement increase from 25 mm to 30 mm. This high strain increase can be attributed to strain concentration which leads to the failure of the specimen.
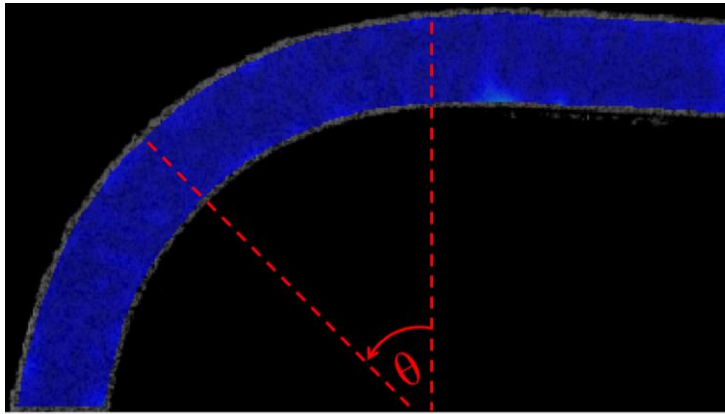
Figure 4.10. Through-the-thickness section where von Mises strains is obtained.
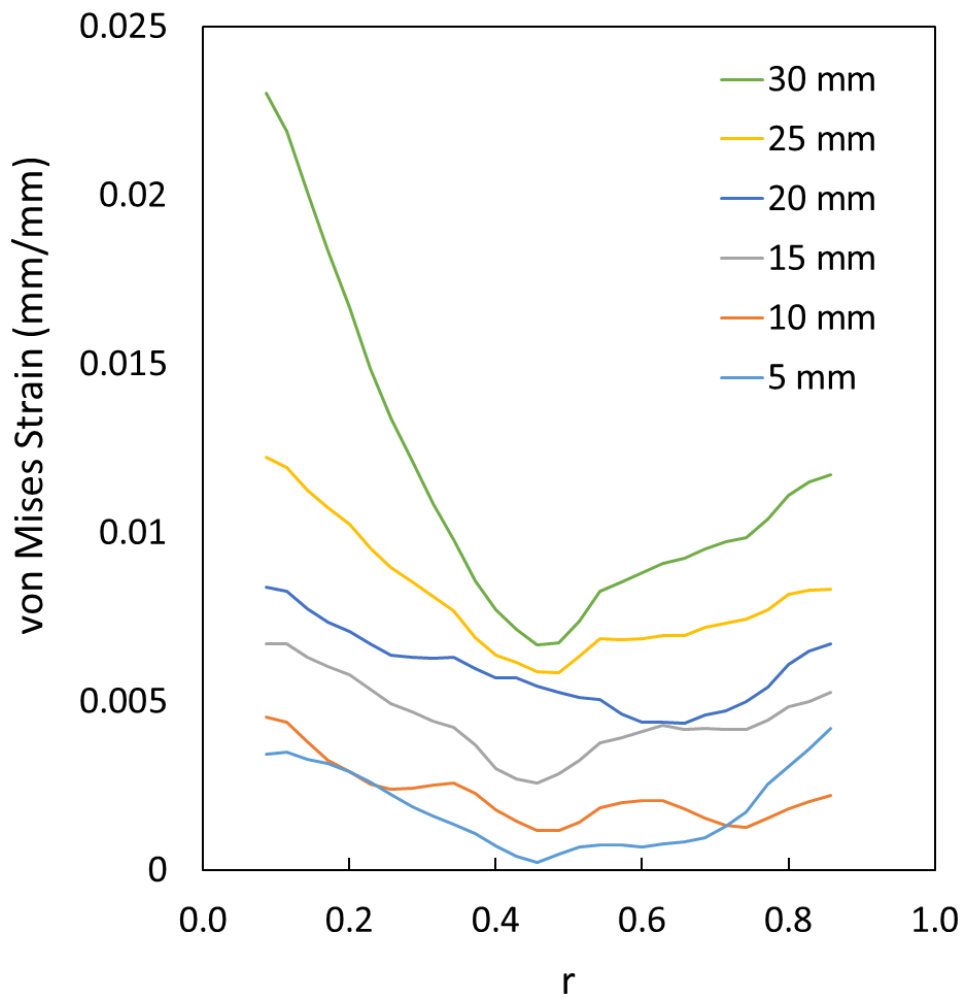
Figure 4.11. Through-the-thickness von Mises strain distribution obtained from digital image correlation method at six different displacement values.

4.1.3   Post-mortem Micrographs

The post-mortem micrograph taken from a tested cross-ply specimen is shown in Figure 4.12. The cracks are highlighted with a black marker to make them more visible. The original micrograph is also given in the APPENDIX B. In the first ninety-degree oriented ply, radial matrix cracks and delamination are observed. Delamination leads to splitting of the 1st and 2nd plies. This delamination, however, do not propagate at the interface so much. In the 2nd (3rd ply) and 3rd (5th ply) ninety-degree oriented plies, meandering matrix cracks are observed. In the 3rd ply, crack meanders in the region which is located between 30° and 52° counterclockwise relative to the transition line from curved region to horizontal arm. In the 5th ply, this meandering behavior occurs at the region between 22° and 57°. It is observed that the region where the meandering behavior occurs is closer to the horizontal arm than the vertical arm. After meandering, the cracks reach the upper 0/90 interface and propagates to the arms. The crack patterns observed in the 7th and 9th plies are also similar to each other. The crack did not propagate inside the ninety-degree oriented ply. It propagates at the lower 0/90 interface, then reaches upper 0/90 interface by making kinks. In addition to the major crack shown in the plies, secondary radial matrix cracks are observed in the ninety-degree-oriented plies. These radial cracks are tilted and approximately reach 60° as they get closer to the vertical arm.
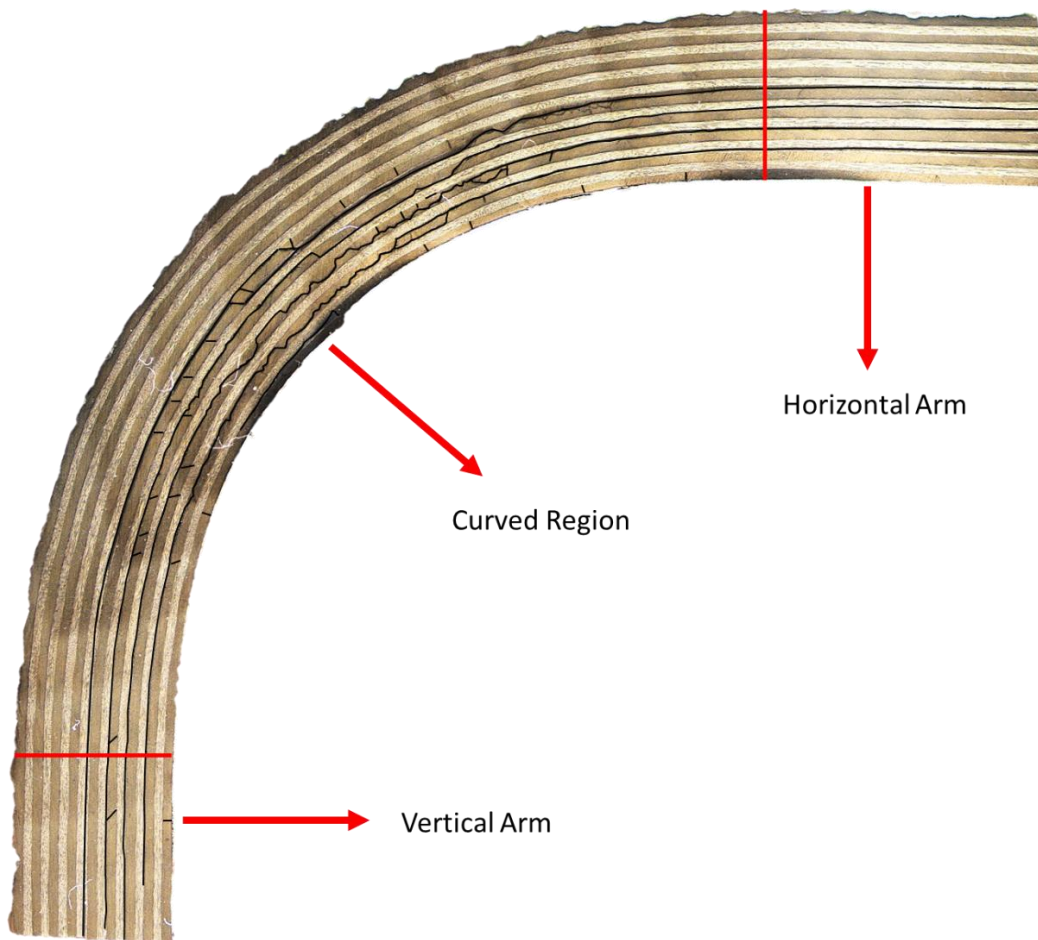
Figure 4.12. Micrograph taken from the specimen sample after the experiment

Figure 4.13 contains the post-mortem micrograph of the curved region of the specimen 90/0-6 and two close-up pictures of the damaged region. In the upper region close up picture, the cracks meander in the 90° oriented ply. In the bottom region close-up picture, it is seen that fiber breakage occurs in the 2nd ply having 0° orientation and the first ply splits from the adjacent 0/90 interface. Radial matrix cracks observed in the 1st ninety-degree oriented ply are also pointed by small orange circles. The radial cracks are not evenly spaced.
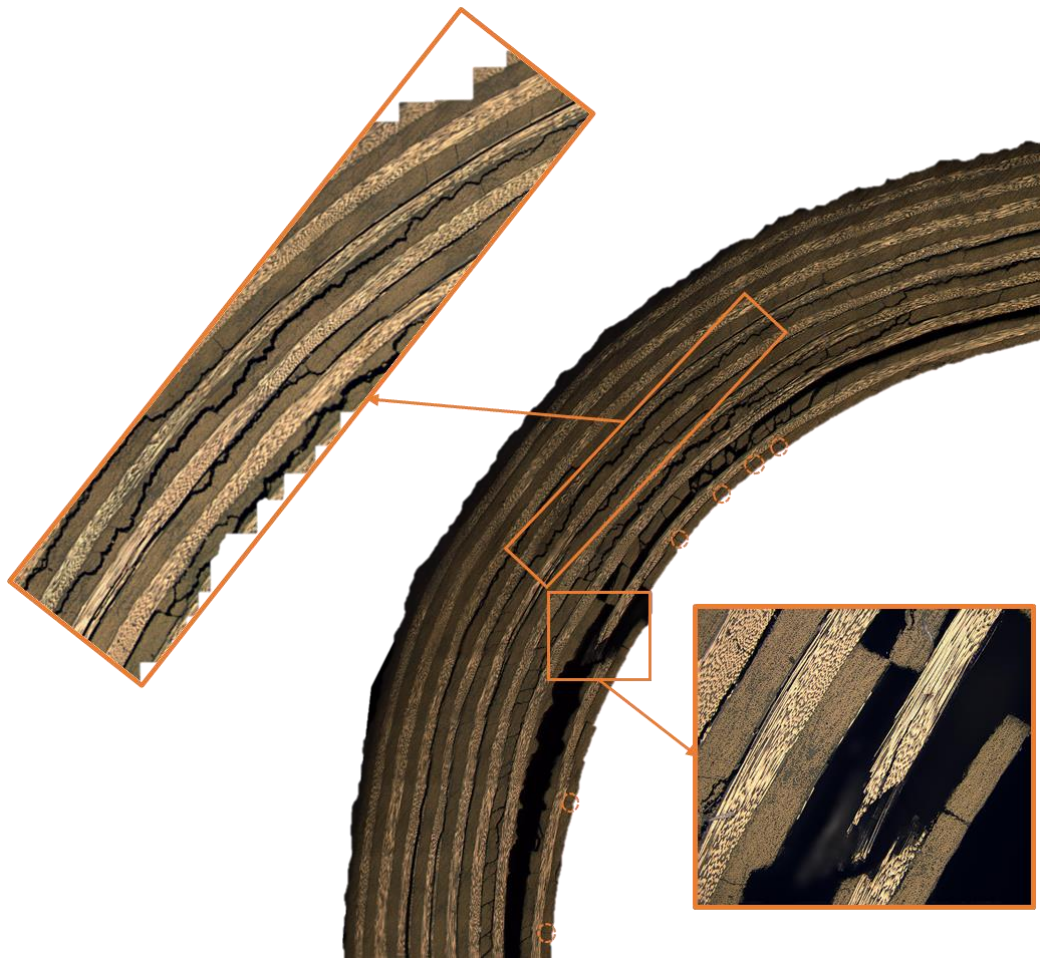
Figure 4.13. Post-mortem micrograph taken from the curved region of specimen 90/0-6

Figure 4.14 contains the post-mortem micrograph of the curved region of the specimen 90/0-8 and two close-up pictures of the damage. The damage occurs in the specimen is similar to the that observed in the specimen 90/0-6. In both close-up picture fiber breakage is shown. The 2nd and 3rd 90° oriented plies break into pieces. Radial matrix cracks observed in the 1st ninety-degree oriented ply also pointed by small orange circles.
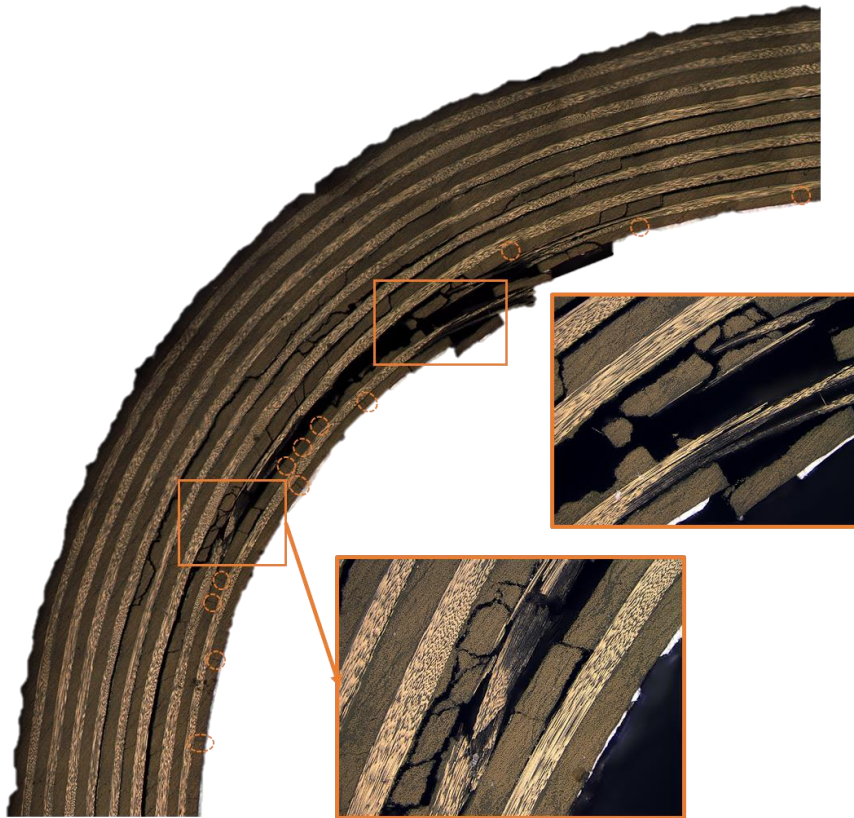
Figure 4.14. Post-mortem micrograph taken from the curved region of specimen 90/0-8

4.2   Finite Element Analysis Results

4.2.1   Elastic Analysis

After the experimental observations are done, stress field over the curved beam is obtained from finite element analysis (FEA) to elucidate failure mechanism of the cross-ply curved composite laminates. Tangential direction of the curved region is defined by θ as shown in Figure 4.15.
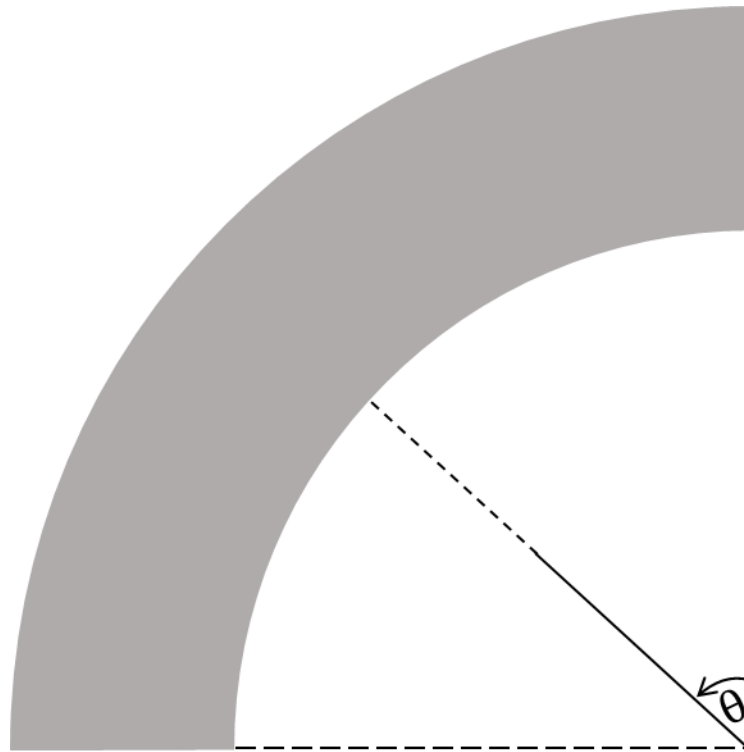
Figure 4.15. Tangential direction of curved beam defined by θ

Stress distribution, shown in Figure 4.16, is obtained at a displacement of 18 mm. Tangential stress is tensile in the inner region while it is compressive in the outer region due to the bending moment, that increases the angle of the curve. Maximum tangential tensile stress in 0° plies is 1084.49 MPa at the section of θ=80° while it is about 85 MPa, which is close to the material strength in the transverse direction, in 90° plies at the section of θ=87°. Radial stress is approximately zero at the arms and all over the inner and outer radii of the curved beam. It increases in the mid-thickness of the curved region and reaches the maximum stress of 34.57 MPa at the section of 72° in the 8th interface between 8th and 9th plies. In the shear stress field, four spot points are observed at the near the boundaries of the curved part and the arms. Maximum positive shear stress occurs at the red point as 17. 79 MPa while minimum shear stress occurs at the blue spot point as -13.66 MPa. Radial and shear stresses are approximately zero in the inner region while high tangential tensile stresses act on that region. Thus, one of the reason of the radial matrix cracks in the inner ninety-

degree oriented plies shown in the post-mortem micrographs might be the tangential stress.
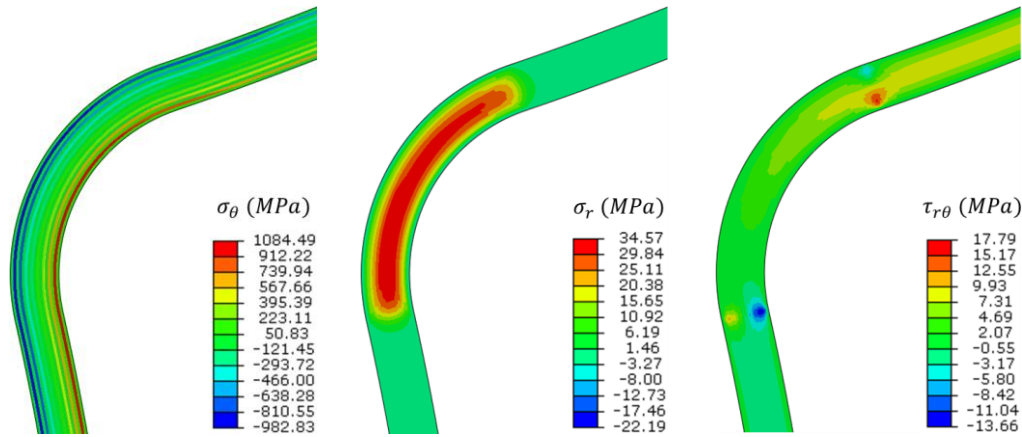
Figure 4.16. Stress field obtained for the cross-ply curved composite laminates: (a) Tangential Stress (b) Radial Stress (c) Shear Stress

Through-the-thickness stress distribution at the section of $\theta=45°$ is taken from finite element analyses and compared with analytic solution as shown in Figure 4.17. For the tangential stresses, σ_θ, there is a good agreement between the analytic solution and finite element (FE) model with analytic boundary conditions (BCs). Analytic solution gives higher tangential stress than the FE model with experimental BCs, and the maximum error is 16 %. Tangential stresses are much higher in 0° oriented plies than in the 90° oriented plies, and it decreases from inner region to the outer region linearly at the plies having the same orientation. For the radial stress, σ_r, analytic solution and FE model with analytic BC gives close results. The error is less than 6 %. The error between the analytic solution and FE with experimental BCs, however, is much higher and is approximately 17 %. Radial stress is low at the inner and outer region of the beam, and increases to the mid-thickness. The 7th, 8th and 9th plies have approximately same radial stresses. For the shear stress, $\tau_{r\theta}$, analytic solution and FE model with analytic BC are in good agreement. The error is less than 3%. The maximum error between the analytic solution and FE with experimental BCs is so high and is approximately 50 %. The trends of radial stress and shear stress distributions are the same. However, the shear stress values are significantly nearly 7 times lower in comparison.

As it was mentioned in the section of 3.1.4, plane stress elements are used in the analysis. The stress distribution for the plane stress and plain strain elements is approximately same. Through-the-thickness stress distributions for these elements are compared and given in APPENDIX C.

Von Mises strain field is obtained from the elastic analysis at a section of $\theta=45°$ for six displacement values and shown in Figure 4.18. von Mises strain increases as the displacement increases. The trend of the distribution is similar at all displacement values. In the inner side of the curved region, von mises strain reach its maximum. In the displacement of 5 mm, its maximum value is 0.0023 mm/mm, and it reaches 0.018 mm/mm in the displacement of 30 mm. Towards the mid-thickness, von Mises strain decreases, and in all displacement values, the minimum von mises strain occurs approximately at the same location where normalized through-the-thickness direction, r, equals 0.51. Toward the outer side of the curved region von Mises strain increases again.
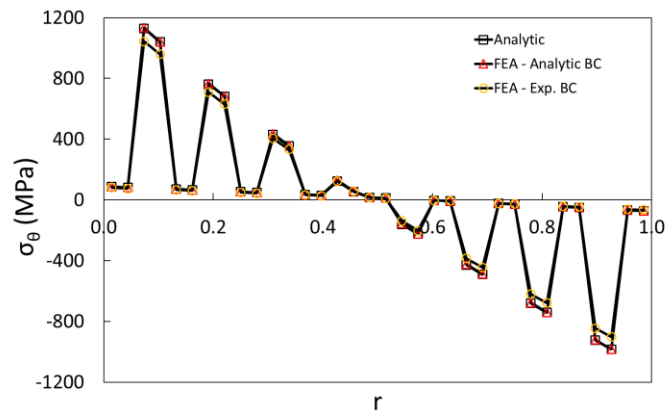
(a)
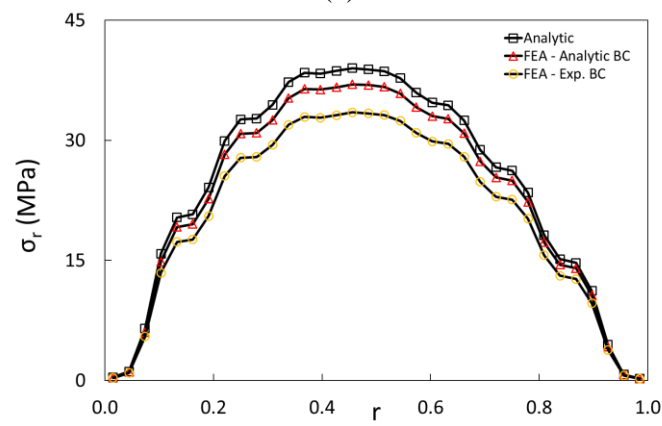
(b)
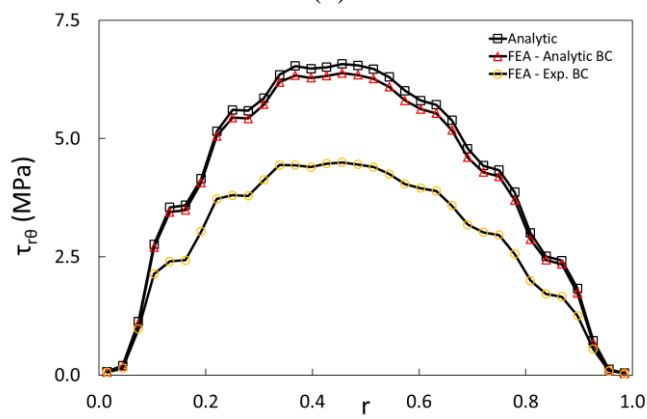
(c)

Figure 4.17. Through-the-thickness stress distribution at the section of θ=45° for cross-ply specimens: (a) Tangential Stress (b) Radial Stress (c) Shear Stress

76
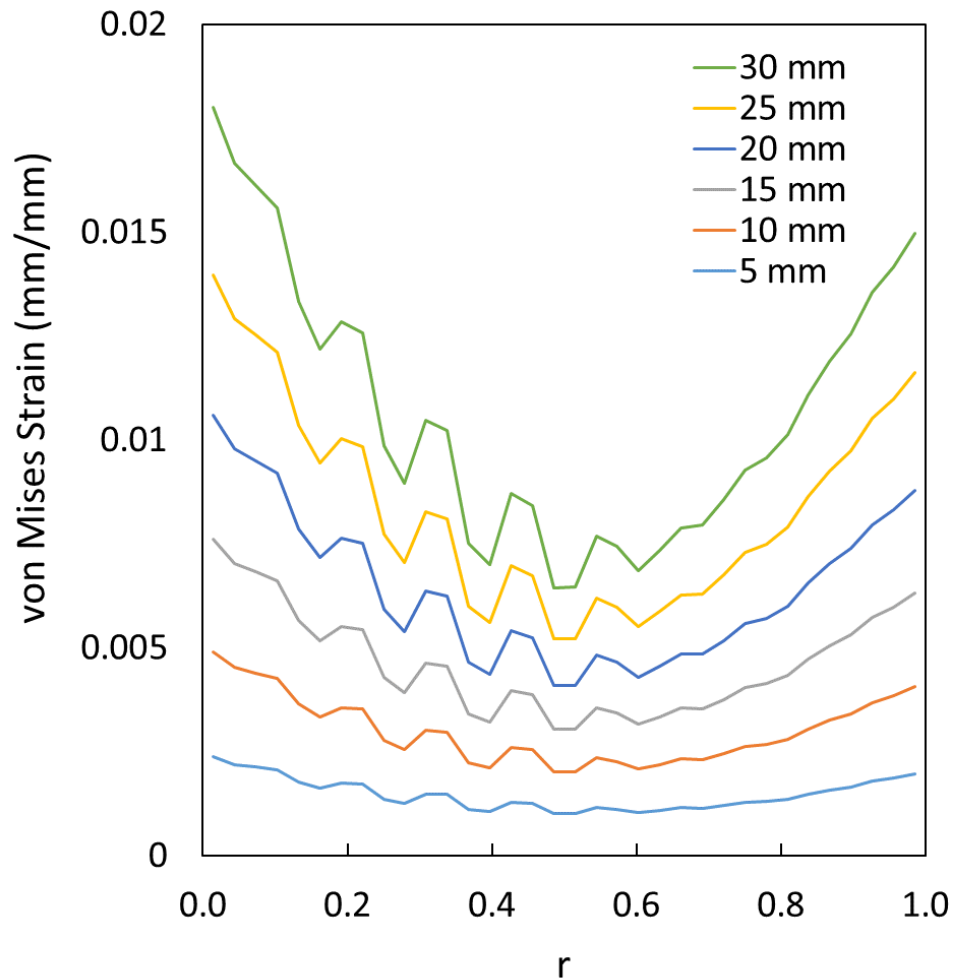
Figure 4.18. Through-the-thickness von Mises strain distribution obtained from finite element analysis at six different displacement values.

4.2.2 Elastic Analysis with Stiffness Reduction of Inner Plies

In Figure 4.19, the interfaces where the delamination occurs are shown. The 1st delamination occurs in the 3rd interface (between the 3rd and 4th plies), and the 1st three plies are separated from the specimen. Then the 2nd delamination occurs in the 4th interface, and two additional plies are separated from the specimens. The following delaminations occur in the next interfaces in order, and additional plies are also separated from the specimen. Delaminations propagate up to the location where

the specimen is clamped to the fixture in vertical arm or mounted to the loading fixture. In 90° oriented plies, radial cracks also occur, and in the arms the crack growth into the 0° oriented plies. Considering these experimental observations, it is assumed that the separated plies after the delamination occurs does not contribute to the stiffness (load carrying capacity) of the specimen.
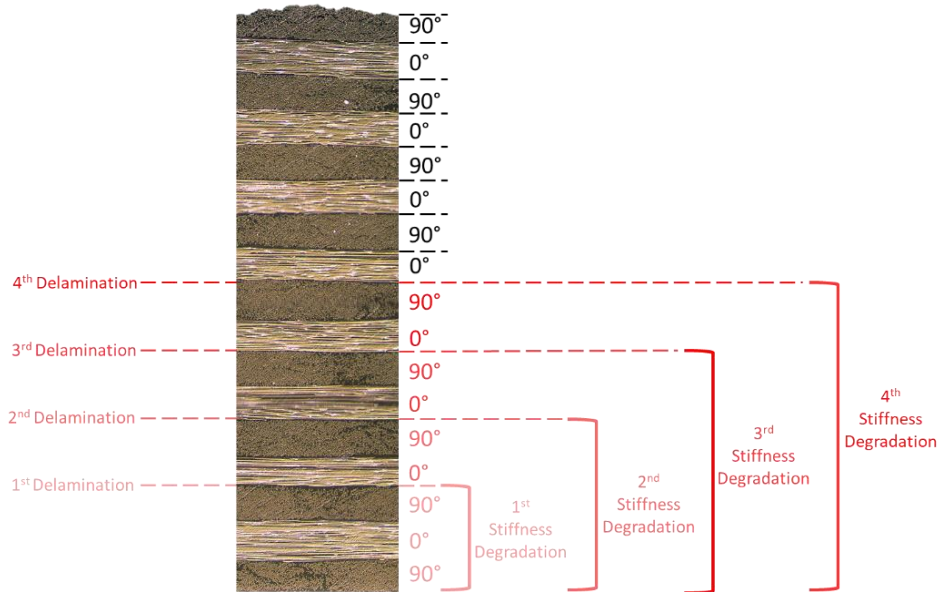
Figure 4.19. Interfaces where the delamination occurs and the plies whose stiffness are degraded.

To simulate the above situation in finite element analysis, additional models are created by degrading elastic modules of the all plies to 100 MPa in both directions. Additional material properties are defined for 0° and 90° oriented plies. Figure 4.20 shows the material definition in the finite element models created for each delamination. Dark and light grey represent the non-degraded 0° and 90° material properties, respectively. Dark and light red represent the degraded 0° and 90° material properties, respectively. The degraded material properties are defined for both curved region and arms. In the load-displacement curves obtained from the finite element analyses are given in Figure 4.21.

1st Stiffness Degradation   2nd Stiffness Degradation

3rd Stiffness Degradation   4th Stiffness Degradation
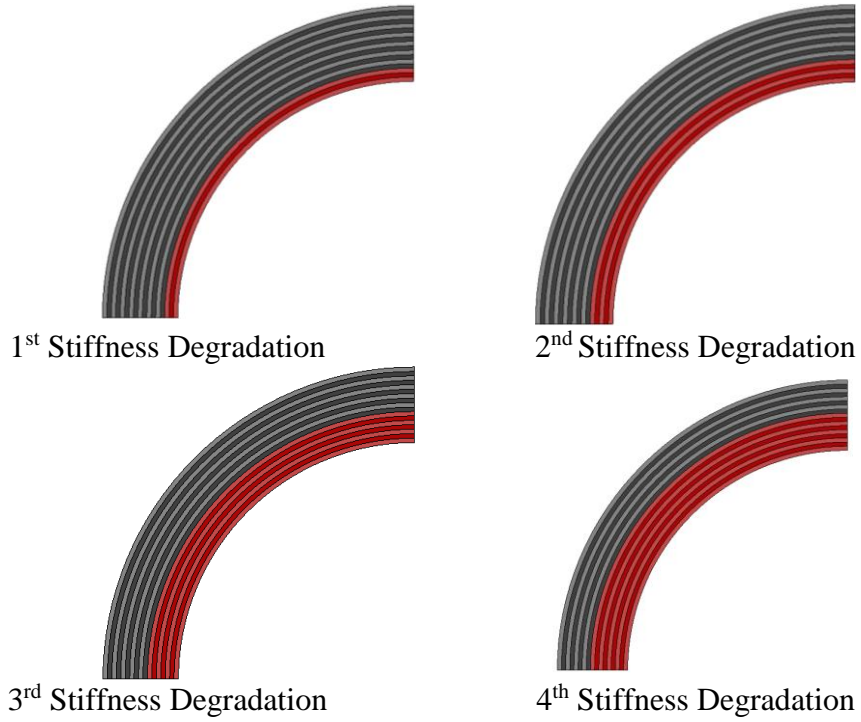
Figure 4.20. Material property map for the stiffness-degraded finite element

models.
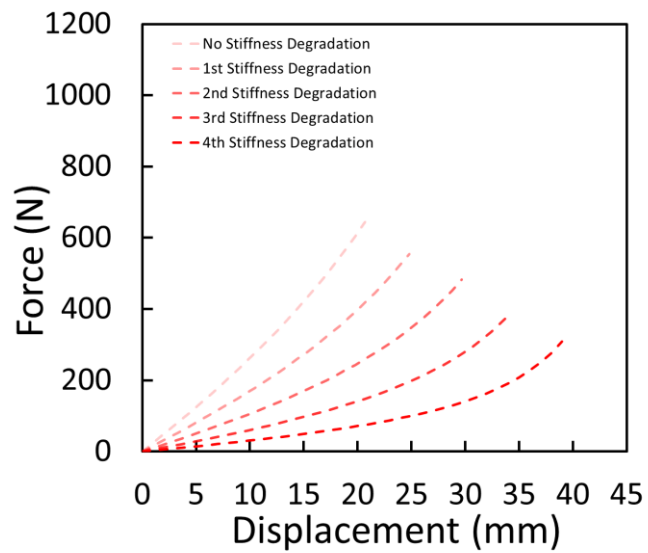
Figure 4.21. Load-displacement curves obtained from the finite element analysis

with degraded material property.

4.2.3   Matrix Damage Progression using Hashin Criteria

To predict the failure pattern observed in the micrograph of cross-ply specimens, Hashin criteria built-in ABAQUS is used. Hashin criteria is defined only 90° plies. Mesh refinement study is conducted. Finite element models are created with an element numbers of 2, 4, 6 and 8 in each ply. Figure 4.22 contains the initiation of the tensile matrix damage in 2-direction at these models. It is observed that matrix crack initiates at the section of $\theta=87°$ in the 1st ply having ninety-degree orientation. At this ply, radial and shear stress is nearly zero. Thus, it can be said that tangential stresses lead to initiation of these matrix cracks.

2 elements per ply

4 elements per ply

6 elements per ply

8 elements per ply
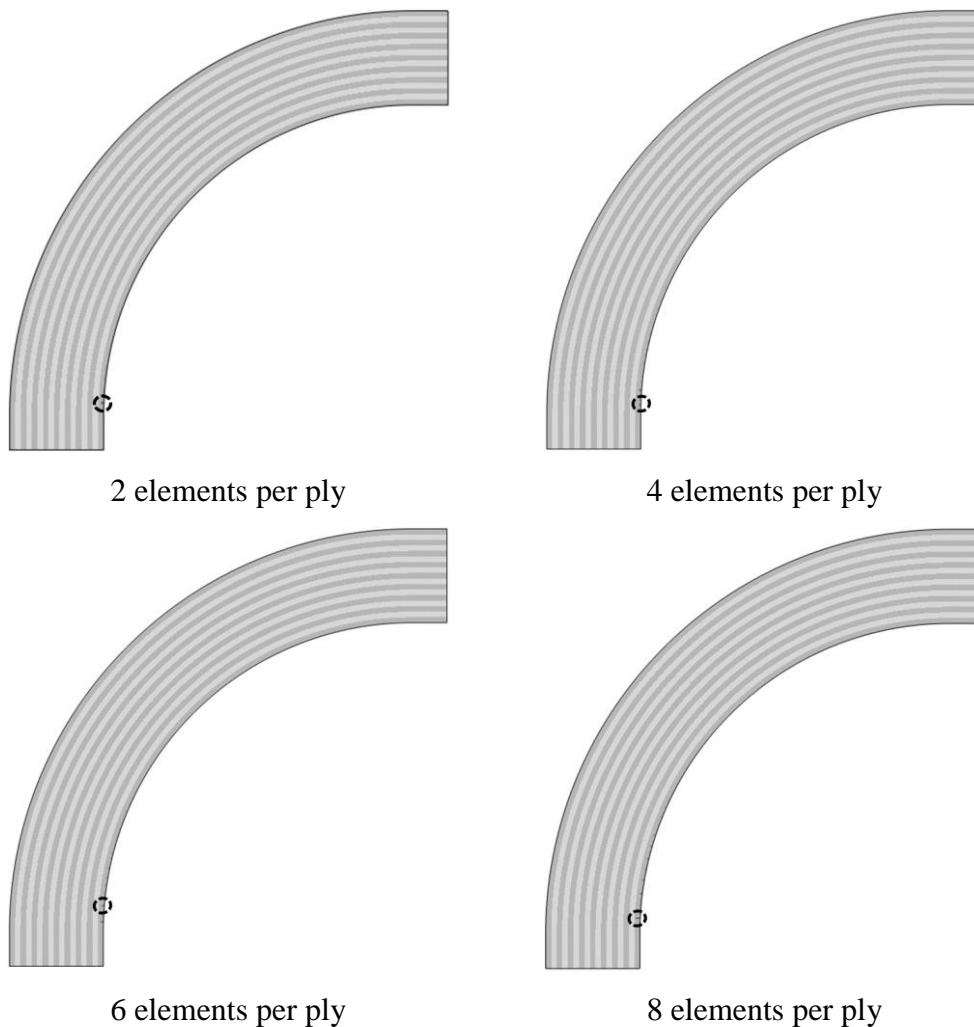
Figure 4.22. Initiation of tensile matrix damage at 2-direction for different mesh refinement

In Figure 4.23 and Figure 4.24, the progression of the matrix damage at these models is given for two different displacement values of 20 mm and 22 mm. It is observed that the matrix cracks are not in evenly spaced manners in all mesh sizes. The number of radial cracks and their through-the-curvature direction at the 1st ply change with mesh size.
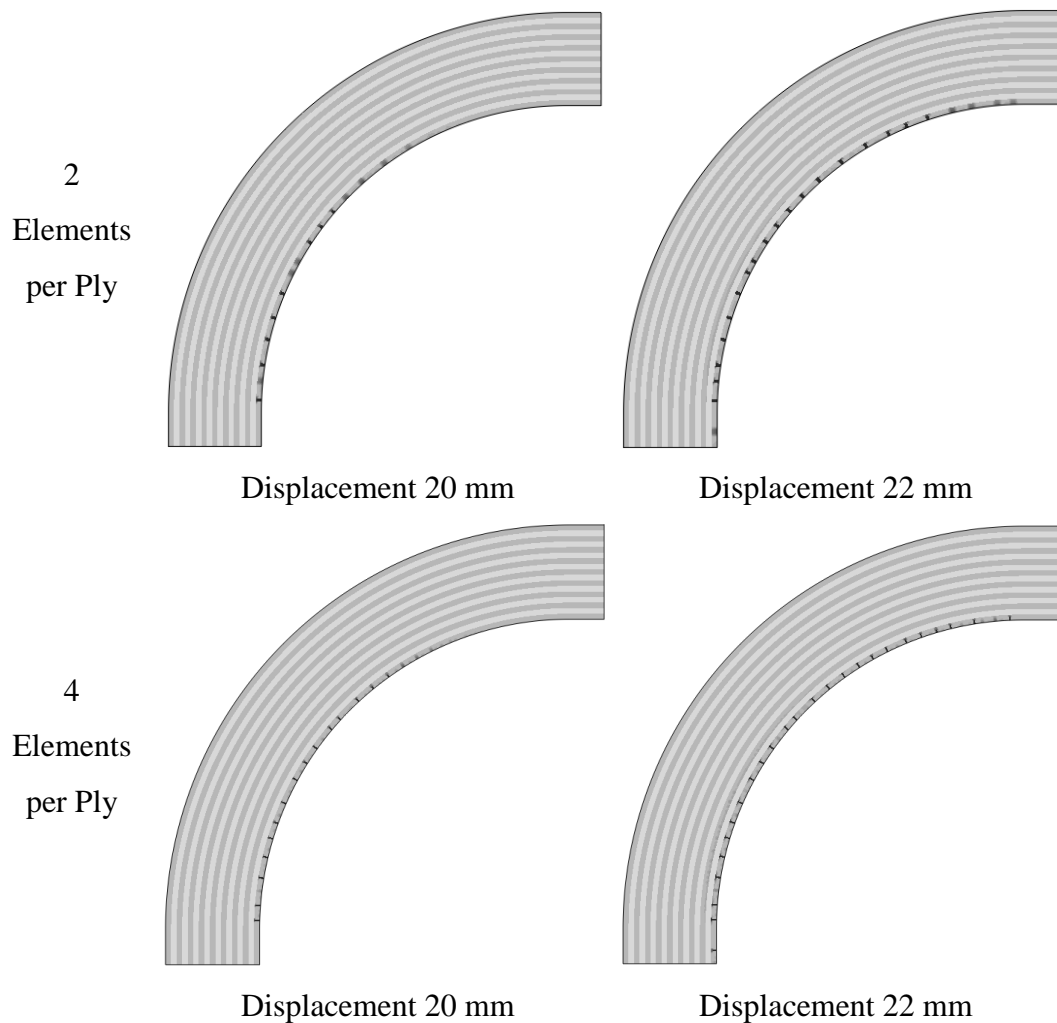
Figure 4.23. Progression of the tensile matrix damage at 2-direction for the mesh refinement of 2 elements per ply and 4 elements per ply
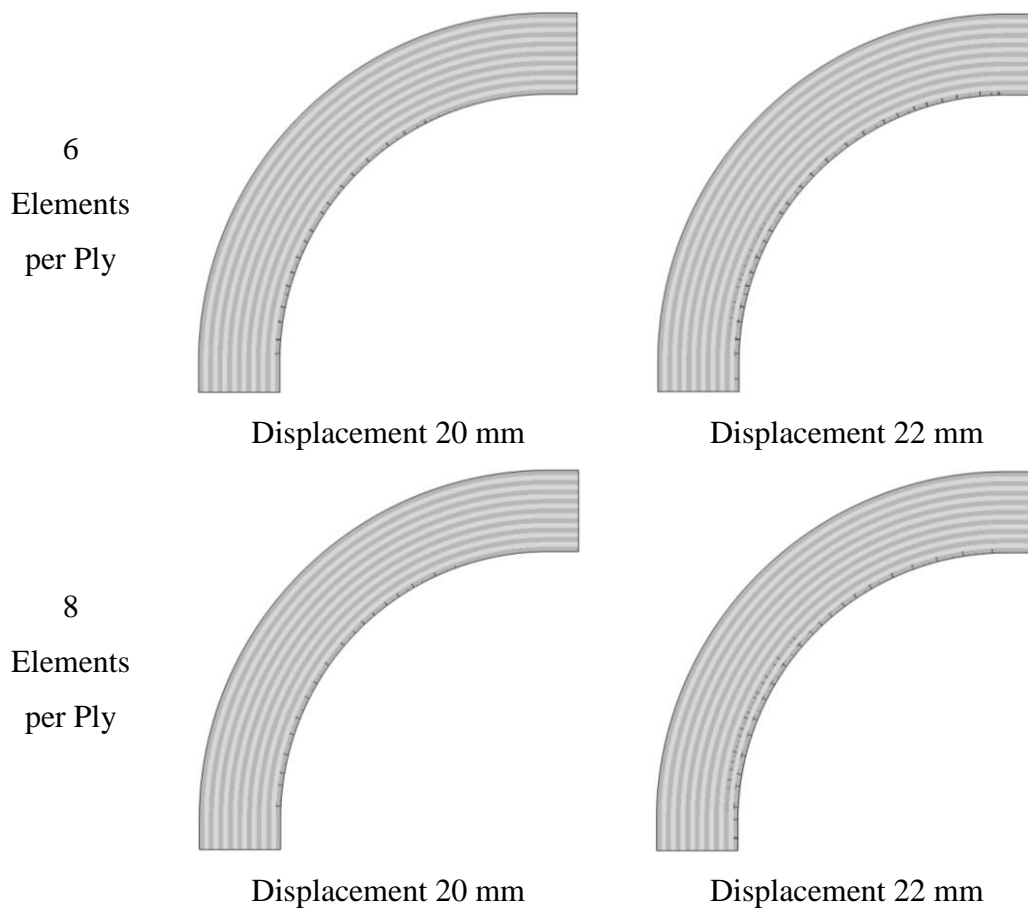
Figure 4.24. Progression of tensile matrix damage at 2-direction for the mesh refinement of 6 elements per ply and 8 elemetns per ply

To observe the crack path orientation in detail, the propagation of the matrix cracks from the model meshed with 8 elements in each ply   are presented for additional three displacement values of 24, 27 and 30 mm as shown in Figure 4.25. At a displacement value of 24 mm, damage in the 2nd 90° ply is also shown. As the displacement increases to 27 mm, matrix crack evolves all over the 2nd 90° ply, and matrix crack starts to initiate in the 3rd 90° ply. At the displacement value of 30 mm, in the first three 90° plies, radial matrix cracks are seen. At all these displacement values, the matrix crack in 3-direction does not occur.

(a)   (b)

(c)
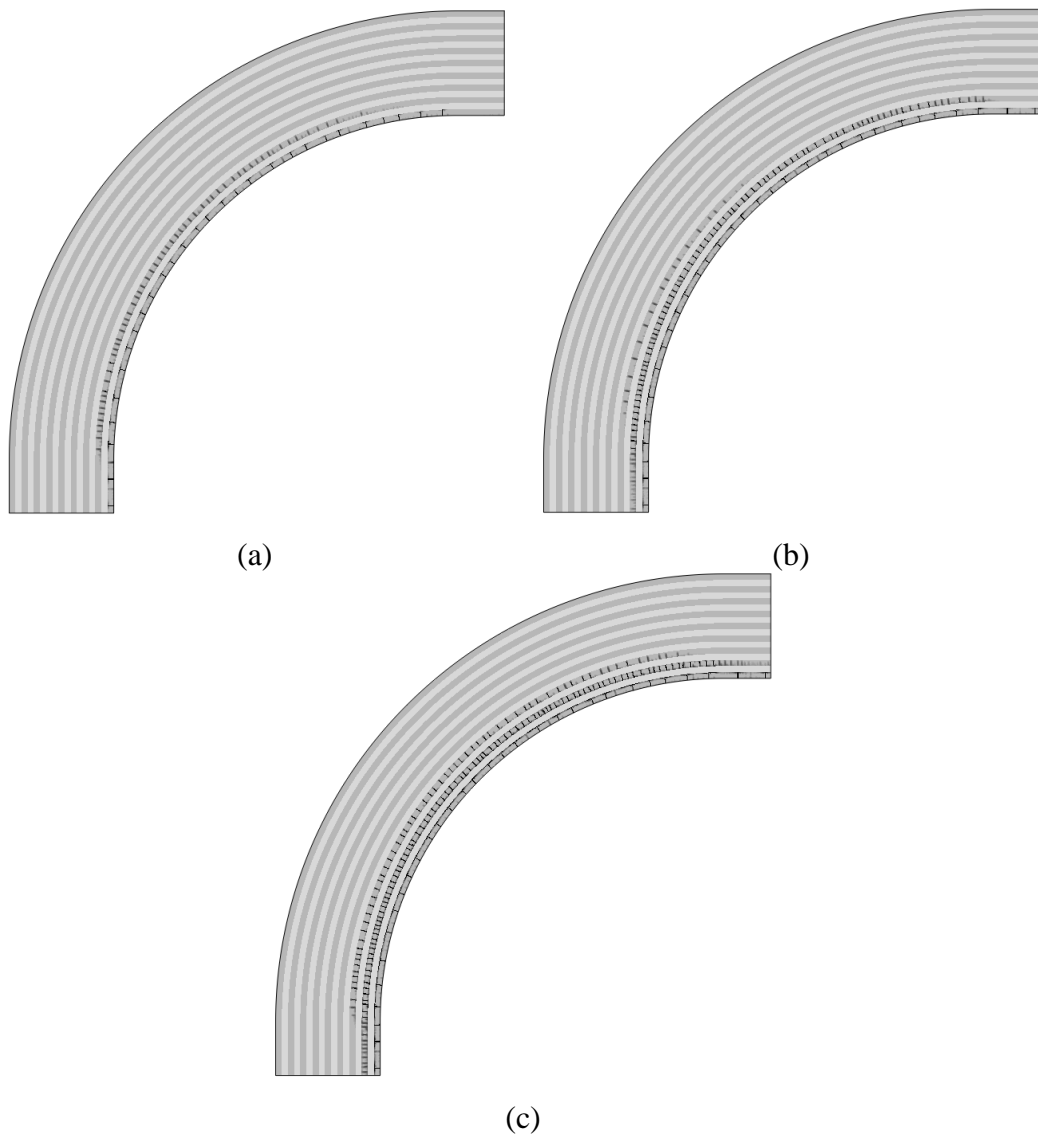
Figure 4.25. Progression of the tensile matrix damage at 2-direction for the mesh refinement of 8 element per ply at a displacement value of: (a) 24 mm, (b) 27 mm and (c) 30 mm

4.3   Discussion

The experimental and numerical results of the cross-ply curved composite laminates are compared in terms of sequential failure mechanism, damage pattern and von Mises strain field.

The comparison of the load-displacement curve obtained from specimen 90/0-1 and 90/0-9 with those obtained from the finite element analysis is shown in Figure 4.26. The stiffness of 90/0-1 after the 1st and 2nd load drop agrees well with the finite element results. In the experiment 90/0-1, a high load drop is seen during the 3rd load-drop since two delaminations occurred simultaneously. Thus, the load-displacement curve taken from the finite element analysis conducted with the 4th stiffness degradation model is consistent with the experimental stiffness after the 3rd load drop. In experiment 90/0-9, sequentially four load drops occurred during the course of the load-drop. Thus, the stiffness of this specimen is in good agreement with that obtained from the finite element analysis conducted with the 4th stiffness degradation model.
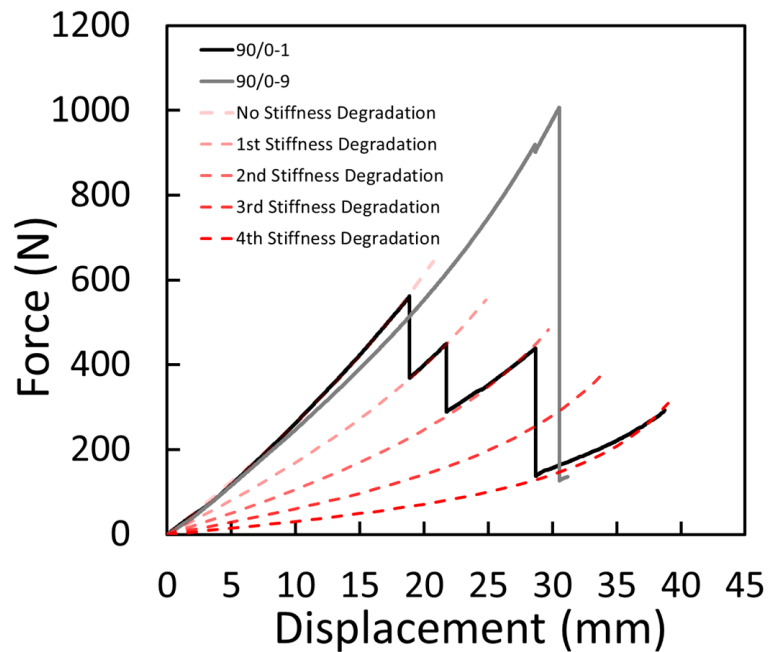
Figure 4.26. Comparison of the load-displacement curve obtained from the experiment and finite element analyses

By considering the good agreement of the load-displacement curves, the failure mechanism can be summarized.

i) In the 1st 90° ply, radial matrix cracks occur due to high tangential stress, but these cracks do not lead to any load drop,

ii) In multiple load drop case, the matrix cracks initiating in the 2nd 90° ply induce delamination, which propagates through the interface between 3nd and 4rd plies. This delamination leads to a reduction in the load-carrying capacity of the laminate since the first three plies do not contribute to the load-carrying capacity of the laminate, anymore. Note that radial stress is so low that it cannot lead to pure delamination. After delamination occurs, stresses are redistributed and the same process mentioned in number ii, occurs for the next 90° plies.

iii) In single load drop case, the first delamination occurs at so high loads that it creates an impact effect on the specimen. Thus, other delaminations occur within micro-seconds after the initiation of first delamination.

iv) In our stacking sequence of $[(90/0)_4, \overline{90}]_s$, the laminate loses its all load-carrying capacity after the delamination occurs in the interface between the 9th and 10th plies.

Damage patterns obtained from both experiment and finite element analysis are shown in Figure 4.27. Radial matrix cracks occurring in the 1st 90° ply shown in the post-mortem micrograph are predicted by Hashin Failure Criteria. The meandering crack path occurring in the 2nd and 3rd 90° plies shown in the post-mortem micrograph, however, is not predicted by Hashin Failure Criteria. To explain the meandering crack path, two studies are considered.
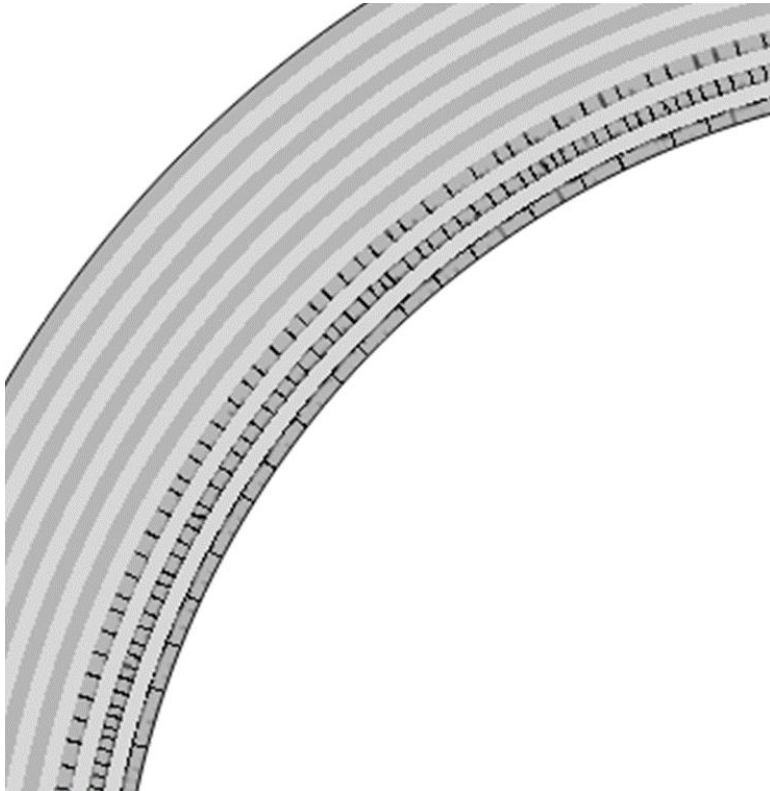
Figure 4.27. Damage pattern observed in the experiment and finite element analysis
for the cross-ply curved composite laminates

The first study investigates the possible crack path of a crack in a brittle adhesive layer between two solid layers, which is conducted by Fleck, Suo and Hutchinson [36]. Figure 4.28a shows the schematic for a crack in an adhesive layer which are constrained by the two solid layers. In our case, crack occurs in brittle matrix inside the 90° oriented ply and this ply is constrained by two 0° oriented plies as shown in Figure 4.28b which makes our case analogues with the problem investigated by Fleck etc. [36]. In Figure 4.28a, T^∞, K_I^∞ and K_{II}^∞ are the non-singular stress acting on the solid layers, mode I and mode II stress intensity factors, respectively. They depend on the loading and geometry. σ_0 is the residual thermal stress. As shown in Figure 4.29, the crack path depends on the local T-stress and the change of the local mode II stress intensity factor with respect to the distance between the crack and the adjacent lower interface, c, (dK$_{II}$/dc). Local T-stress is a function that depends on the T^∞ and σ_0. In our case, adjacent 0° plies are under tensile stress and tensile thermal stresses arise in the 90° due to the curing process. Thus, the local T-stress is positive. To find the sign of dK_{II}/dc the second study conducted by Lu, Xia and Hutchinson [37] is considered.

<table>
<tr><td>(a)</td><td>(b)</td></tr>
</table>
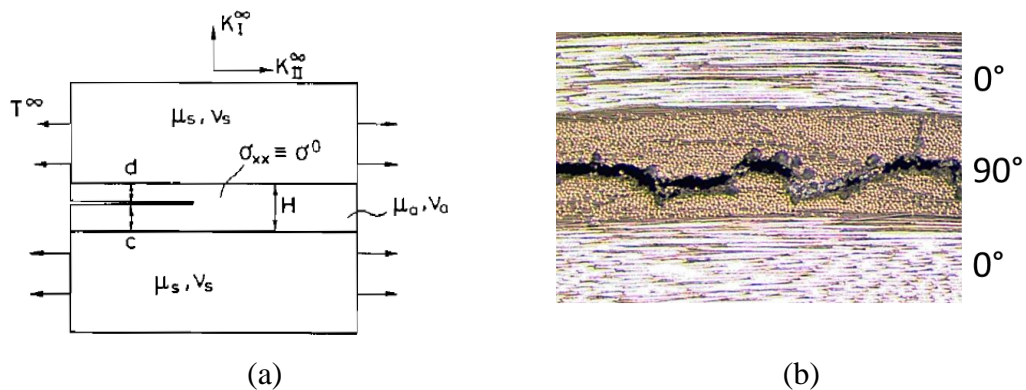
Figure 4.28. (a) Crack inside an adhesive layer constrained by solid layer and (b) Crack in brittle matrix inside the 90° ply constrained by the 0° plies
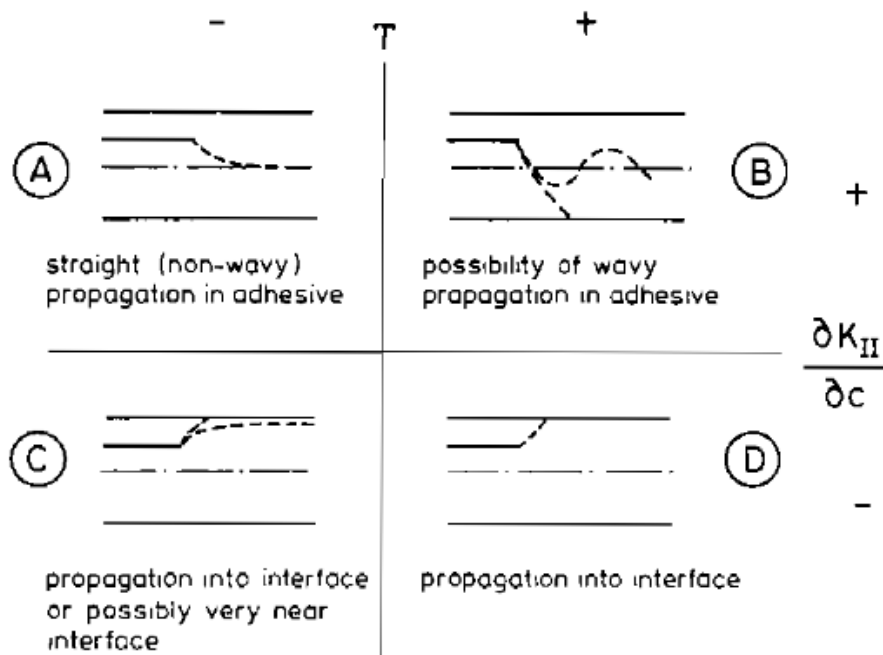
Figure 4.29. Possible crack paths in a brittle adhesive layer

In this study, the curved beam with an initial crack length under pure bending moment, shown in Figure 4.30, was investigated. h_1 and h_2 stands for through-the-thickness location of the crack. The crack length is represented by θ. The change of the strain energy release rate and mode mixity phase angle with the crack length were provided for different through-thickness locations of the crack. Strain energy release rate (SERR) and mode mixity phase angle (φ) depend on the local stress intensity factors K_I and K_{II}. By using the provided data for SERR and φ, stress intensity factors are calculated, separately. The change of mode II stress intensity factor with the crack length for different through-thickness crack locations is plotted as shown in Figure 4.31. The through-thickness location of the crack is defined by η, which is equal to h_1/h_2. As shown in Figure 4.31, the mode II stress intensity factor decreases as η increases, which means that the h_2 decreases, to a crack length of $\theta=37.5°$. Thus, dK_{II}/dh_2 is positive to the crack length of $\theta=37.5°$. After that crack length, it changes sign and will be negative. dK_{II}/dh_2 is analogous to dK_{II}/dc is given in Figure 4.28.
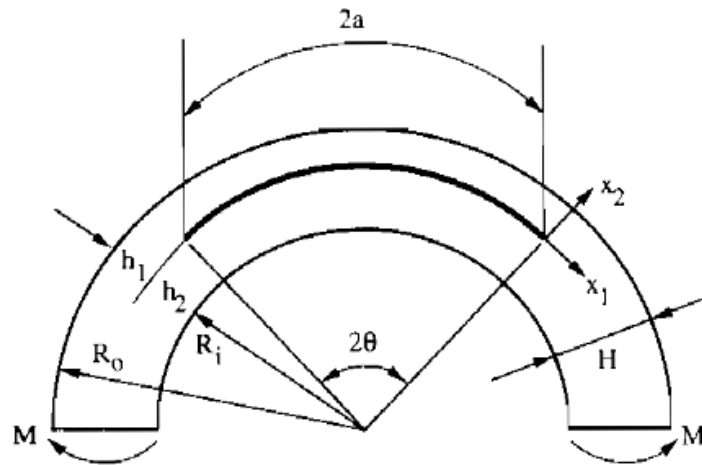
Figure 4.30. Curved beam with an initial crack length under pure bending moment
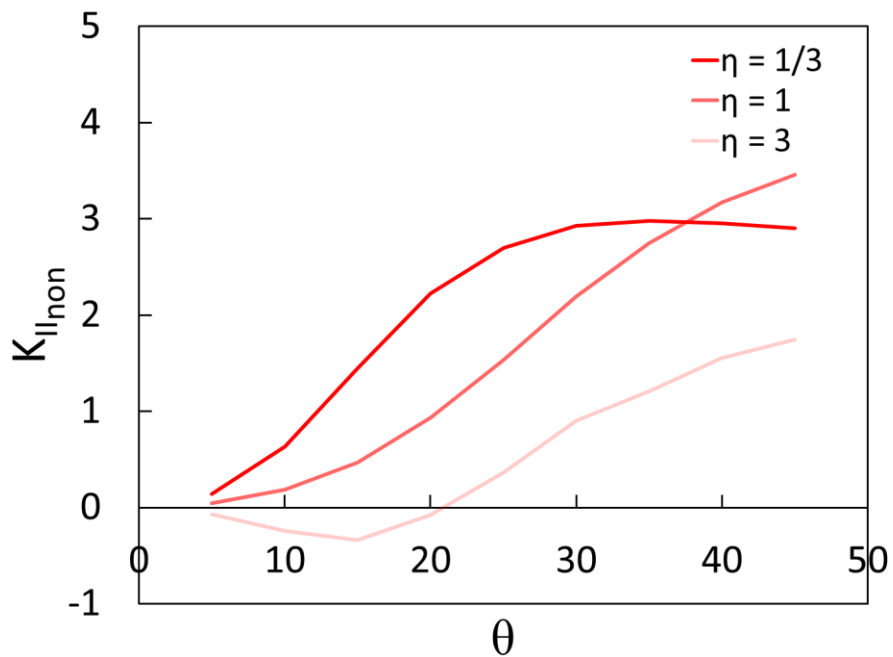
Figure 4.31. Mode II stress intensity factor versus crack length at different through-thickness locations of the crack

In our case, it is known that the T-stress is positive and dK_{II}/dc is positive up to a certain crack length, then it changes sign. Referring to Figure 4.29, for positive local T-stress, meandering crack path occurs when the sign of dK_{II}/dc is positive and crack tip reaches the upper interface when the sign of dK_{II}/dc is negative. This situation justifies the occurrence of the meandering crack path shown in the post-

mortem micrograph. In the finite element analysis, residual stress is not modelled. A recent study carried out by Fu and Wang [38] shows that the residual thermal stresses on the 90° ply constrained by the 0° plies lead to the change of the crack path. Thus, a possible reason for the absence of the meandering crack path in the finite element analysis can be lack of the residual stresses.

Von Mises strain distributions obtained from the specimen 90/0-9 and finite element analysis (FEA) at the same displacement values are compared and given in Figure 4.32. At the displacement of 5 mm (Figure 4.32a), there is a huge difference between von Mises strain distributions obtained from experiment and FEA. As it was mentioned in Section 4.1.2, the data taken from the digital image correlation method is misleading. As shown in Figure 4.32b-e, in the displacement values of 10 mm, 15 mm, 20 mm and 25 mm, von Mises strain distribution obtained from the experiment are in good experiment with FEA results. In the displacement value of 30 mm, there is a huge discrepancy between the experimental and finite element results. which is attributed to the effect of the matrix cracks on the strain field. The failure displacement of the specimen 90/0-5 is 30.9 mm, and this discrepancy is observed at which the specimen is close to failure displacement. Up to a displacement value of 25 mm, there is no marked difference between von Mises strain field distributions obtained from the experiment and FEA. As the specimen is loaded, the matrix cracks lead to the strain concentration as shown in the von Mises strain distribution observed in the experiment.
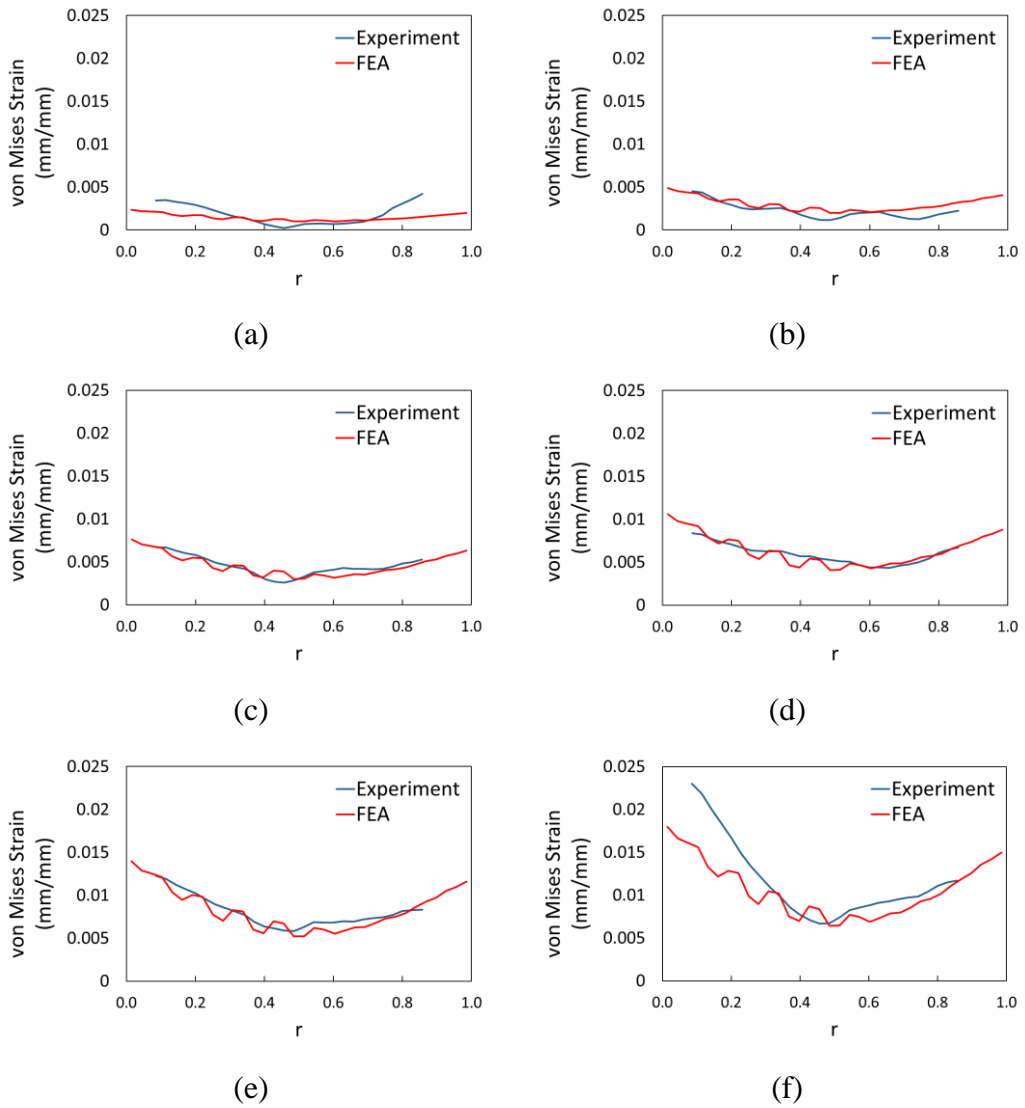
Figure 4.32. Comparison of the von Mises strain distribution obtained from the experiment and finite element analysis at different displacement values of : (a) 5mm, (b) 10 mm, (c) 15 mm, (d) 20 mm, (e) 25 mm and (f) 30 mm

CHAPTER 5

RESULTS FOR FABRIC CURVED COMPOSITE LAMINATES

5.1 Experimental Results

Three experiments are conducted with fabric curved composite laminates having a stacking sequence of $[(45/0)_7, 45/45/0/45]$. All experiments are recorded with a high-speed camera at 420000 fps with a resolution of 64×96 pixels. In the experiment of Fabric 2 and Fabric 3, the curved regions of the specimens are investigated with high speed camera whereas in the experiment of Fabric 1, the vertical arm is investigated. After the first failure occurred, the experiments of fabric 2 and fabric 3 are stopped to avoid from the 2nd failure. The experiment of Fabric 1 is continued after the failure happened to obtain stiffness of the failed specimen. Two surfaces of the specimens are grinded, and fractography of specimens is investigated with digital microscopy.

Load-displacement curves of the specimens are shown in Figure 5.1. The stiffness of Fabric 2 and Fabric 3 is approximately the same with value of 27.80±0.20 N/mm while that of Fabric 1 is lower than these specimens and 25.4 N/mm. In each experiment, sudden load drops are observed with delamination failure mode.
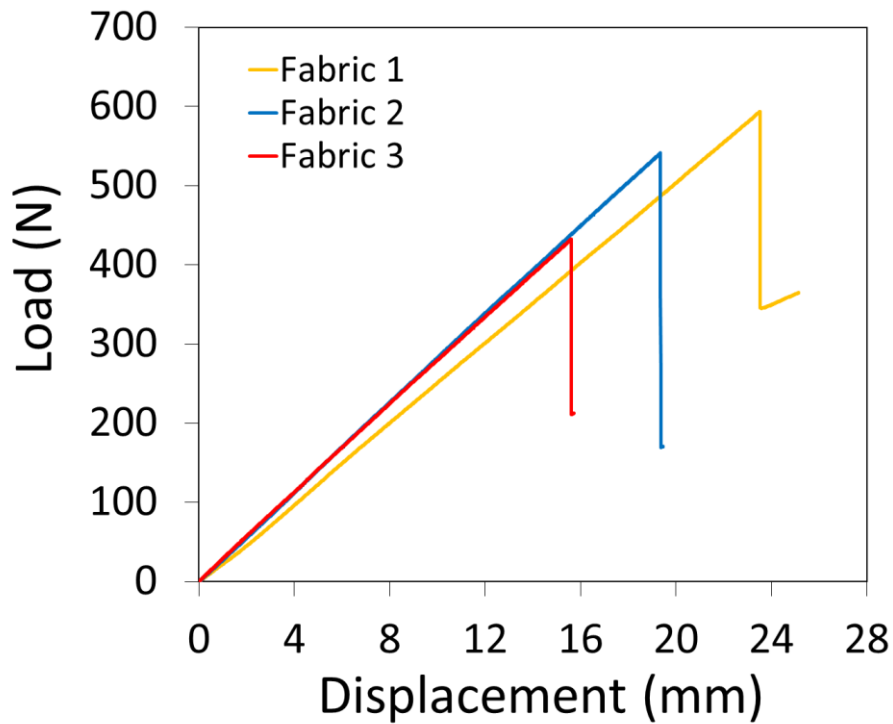
Figure 5.1. Load-displacement curves of fabric curved composite laminates.

5.1.1 In-situ High-speed Camera Images and The Crack Tip Speeds

Propagation of the crack tips to the horizontal and vertical arms in the specimen Fabric 2 is shown in Figure 5.2. Due to chosen frame rate, there is a 2.38 μs difference between each frame. Crack tips are pointed out with red arrows. The first image shows (t=0 μs) just before the failure occurs. As it was seen from the 2nd image (t=2.38 μs), the exact crack nucleation point could not be captured. Thus, to determine the crack nucleation point, the same method as it was done in high-speed camera images of cross-ply specimens is applied. As shown from the images, crack extends in the vertical arm more than in the horizontal arm. Crack initiates approximately at approximatley 31% of thickness at the curved region, which correspond to the inside of the 6th ply.
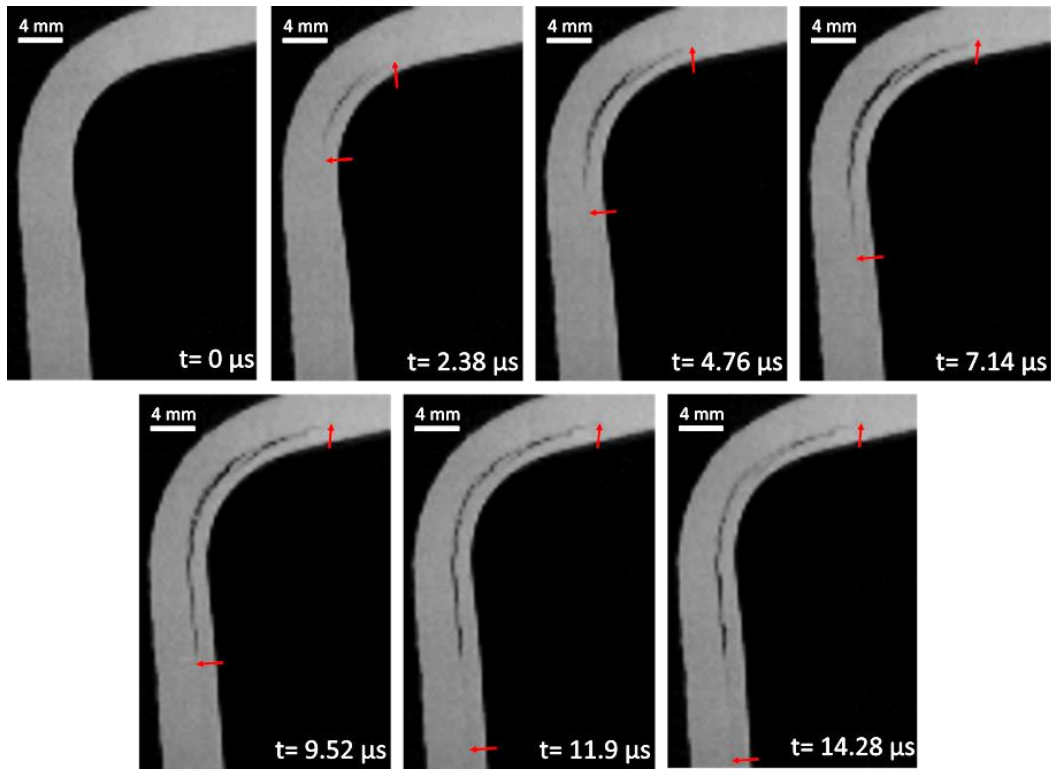
Figure 5.2. Propagation of the crack during the first load drop for the fabric specimen Fabric 2

187.71 µs after the initiation of 1st failure in the specimen Fabric 2, the secondary crack occurs as shown in Figure 5.4. Secondary crack initiates at the curved region at the outer side of 1st failure in the first load drop.
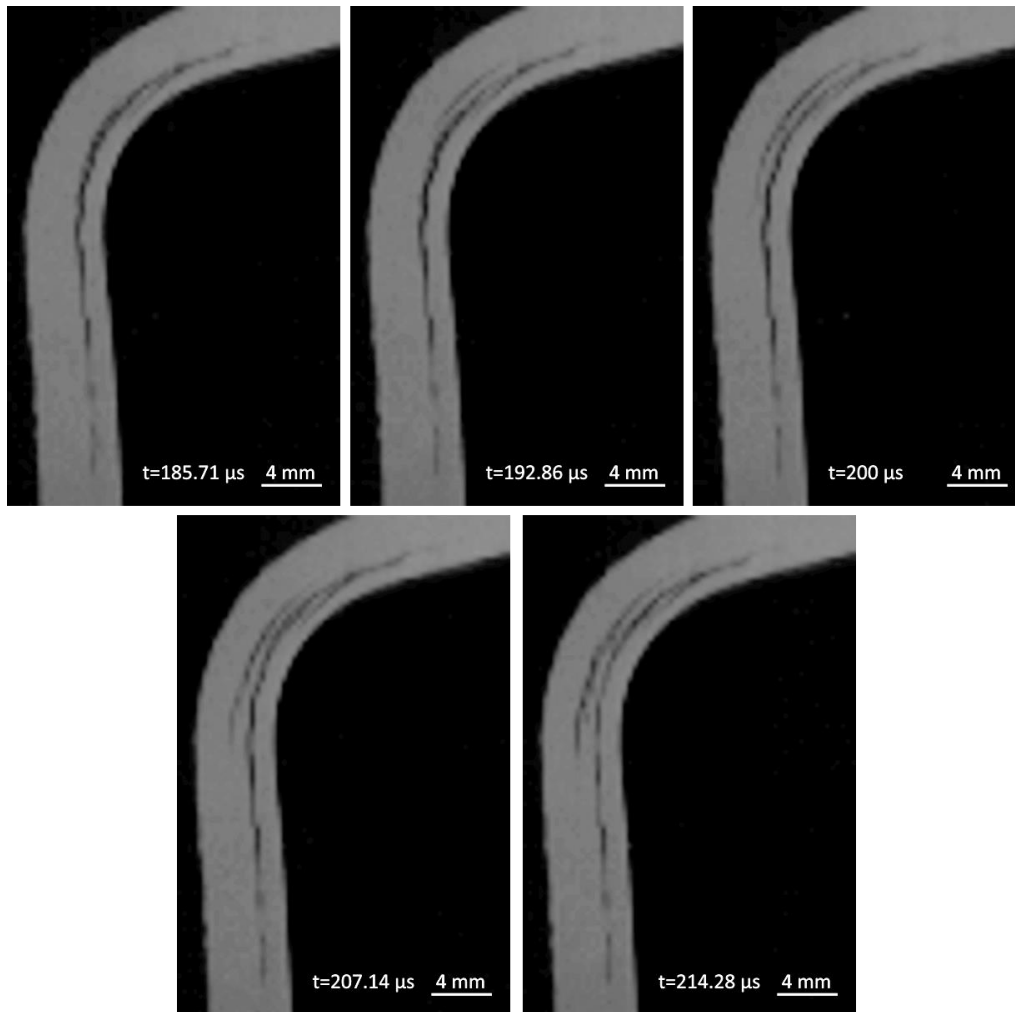
Figure 5.3. Secondary crack initiation 185.71 μs after the 1st failure occurs in the fabric specimen Fabric 2

The propagation of the crack in the specimen Fabric 1 over the vertical arm is shown in Figure 5.4. The 1st image shows that the crack enters the camera frame. Unlike the crack propagation observed in the specimen Fabric 2 and Fabric 3, the crack in specimen Fabric 1 propagates closer to the outer radii, and it is arrested in the vertical arm without extending further.
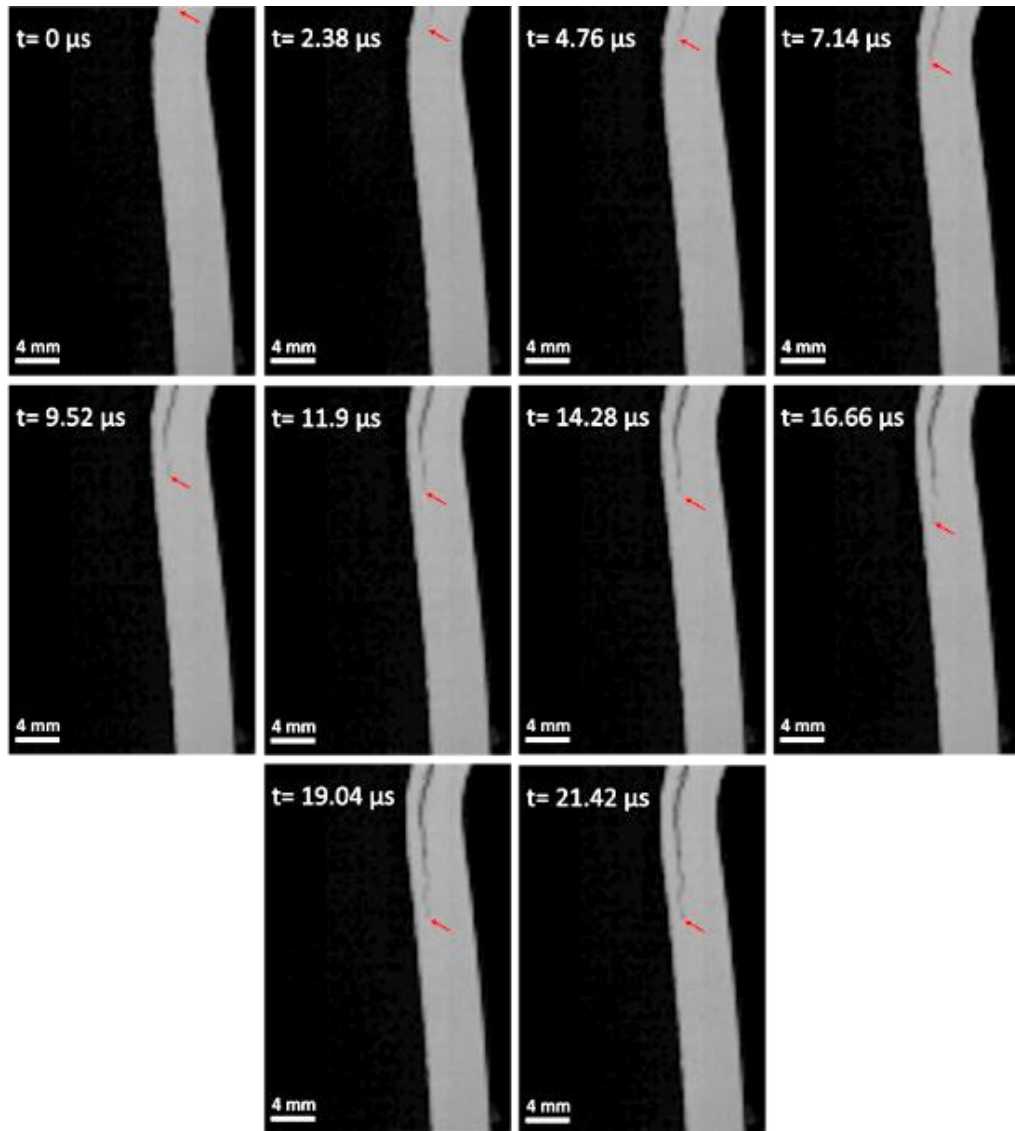
Figure 5.4. Propagation of the crack during the first load drop for the fabric specimen Fabric 1

The crack nucleation point and crack tip position/speed are calculated with the method mentioned in Section 4.1. Upper and lower crack tip position history are plotted in Figure 5.5a-b, respectively. In the experiment Fabric 1, the vertical arm of the specimen where the lower crack propagates is captured. Thus, only the lower crack tip speed could be obtained in that experiment. It is observed that the lower crack tip extends more than the upper crack tip. In the experiment Fabric 2 and Fabric

3, the lower crack tip extends over 24.88 mm and 17.64 mm, respectively. The upper crack, however, extends over 13.36 mm and 14.44 mm in the experiment Fabric 2 and Fabric 3, respectively. In experiment Fabric 3, the crack tip could not be located visually in some frames. Thus, there is a higher step time between certain position data points.

Upper and lower crack tip speed histories are plotted in Figure 5.5c-d, respectively. In the experiment Fabric 2, the upper crack tip gradually slows down from the speed of 1891.40 m/s, which is higher than the material shear wave speed, 1767 m/s, to the speed of 275.72 m/s. Contrary to the upper crack tip speed observed in the experiment Fabric 2, the crack tip speed fluctuates in the experiment Fabric 3. In that experiment, the upper crack initiates with a speed of 1313.95 m/s, then speeds up to the maximum speed of 1482.79 m/s. After this speed, crack tip speed decreases to 226.33 m/s by fluctuating. As for the lower crack tip, in experiment Fabric 3, it initiates with a speed of 1038.82 m/s, then speeds up to the maximum speed of 1383.51 m/s. After reaching the maximum speed, it gradually decreases to the speed of 525.95 m/s. In Fabric 1, lower crack tip speed fluctuates during its propagation through the vertical arm. The maximum speed it reaches during its propagation is 1133.2 m/s. It is arrested in the vertical arm before the crack tip goes beyond the capture region of the camera. Thus, the last speed data is 0 m/s. In the experiment Fabric 2, the crack initiates with a speed of 2173.80 m/s, which is beyond the material shear wave speed. The speed decreases to sub-Rayleigh speed 1206.78 m/, then increases to the intersonic speed of 1919 m/s. It propagates with about that speed for a while. Then it slows down to 483.65 m/s sharply.
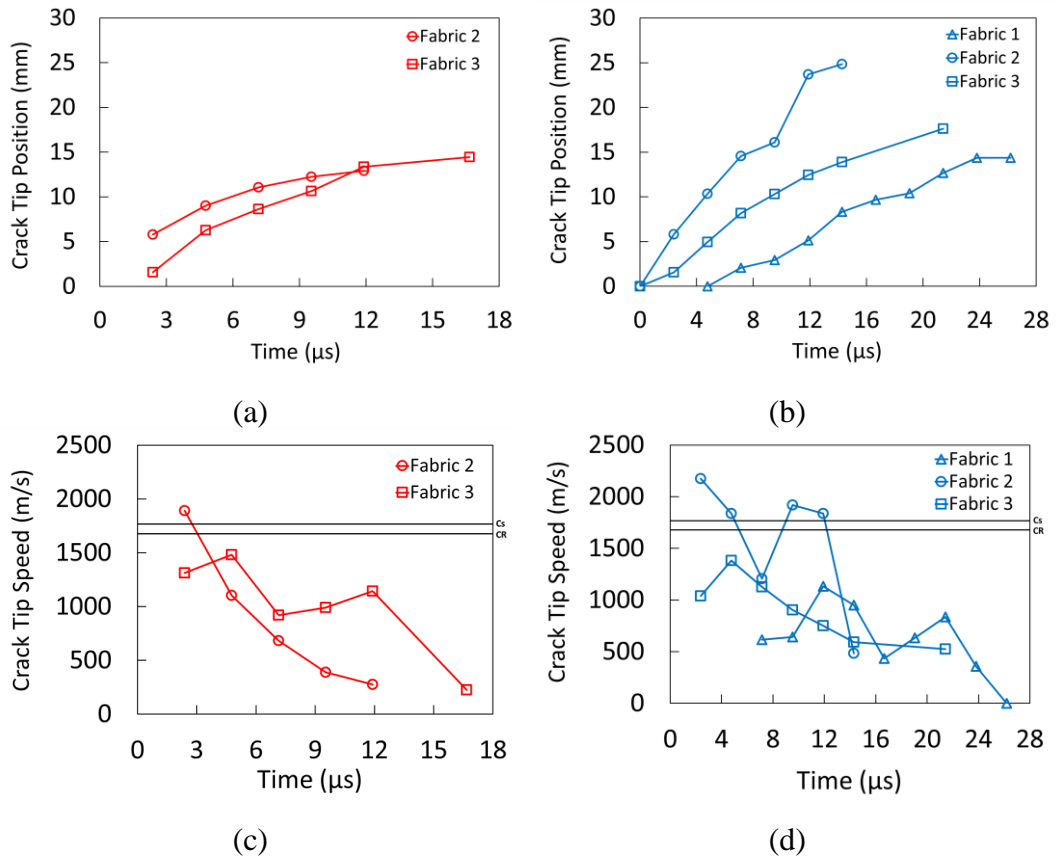
Figure 5.5. Crack tip position and speed history for fabric laminates: (a) upper crack tip position, (b) lower crack tip position, (c) upper crack tip speed, (d) lower crack tip speed.

5.1.2   Post-mortem Micrographs

Before mentioning about the failure mechanism of the fabric specimens with post-mortem micrographs, the microstructure of the specimen is explained with micrographs since the microstructure of fabric materials affects the failure mechanism.

In 5-harness satin weave style each warp passes over four fills then under one fill, and repeat that as shown in Figure 5.6. Stacking sequence of the fabric specimens consists of 0° and 45° oriented plies as shown in Figure 5.7. Resin-rich regions occurs on the interface between these plies, and that interface is called as "Inter-ply

interface". 0° and 45° oriented plies consist of 0/90 and +45/-45 interfaces, respectively. These interfaces are called as "Intra-ply interface"

Figure 5.6. 5-harness weave style.
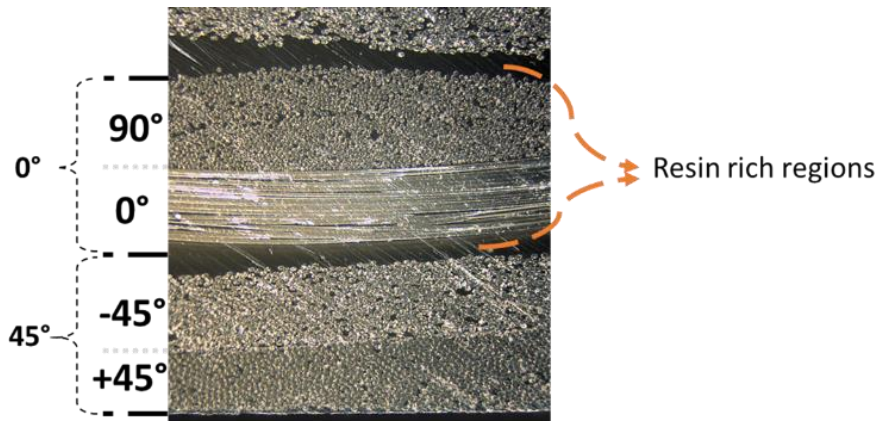
Figure 5.7. Resin rich regions and intra-ply interfaces.

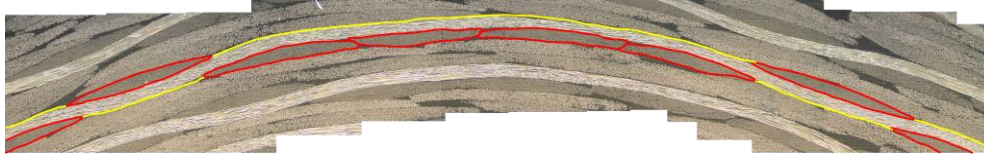The front face, which was captured from the thickness side in the experiment, is grinded, and detailed micrographs are taken. In Figure 5.8, micrographs taken from the curved region of the specimens at 50x magnification are shown. The main crack is defined as the crack which reaches the arms. In the specimen Fabric 1, the main crack propagates through 12th and 13th plies having 45° and 0°, respectively. Inner crack which propagates through the 11th ply having 0° orientation is arrested without reaching the arms. In the specimen Fabric 2, the main crack initiates in the 6th ply having 0° orientation. Secondary crack observed in the high-speed camera images propagates inside the 8th and 9th plies. That secondary crack is arrested without propagating inside the arms too much. The main crack observed in the specimen Fabric 3 initiates in the 6th and 7th ply. The crack which propagates through the horizontal arm is inside the 6th ply having 0° orientation while the crack propagating through the vertical arm is inside the 7th ply having 45° orientation.

(a)

(b)

(c)
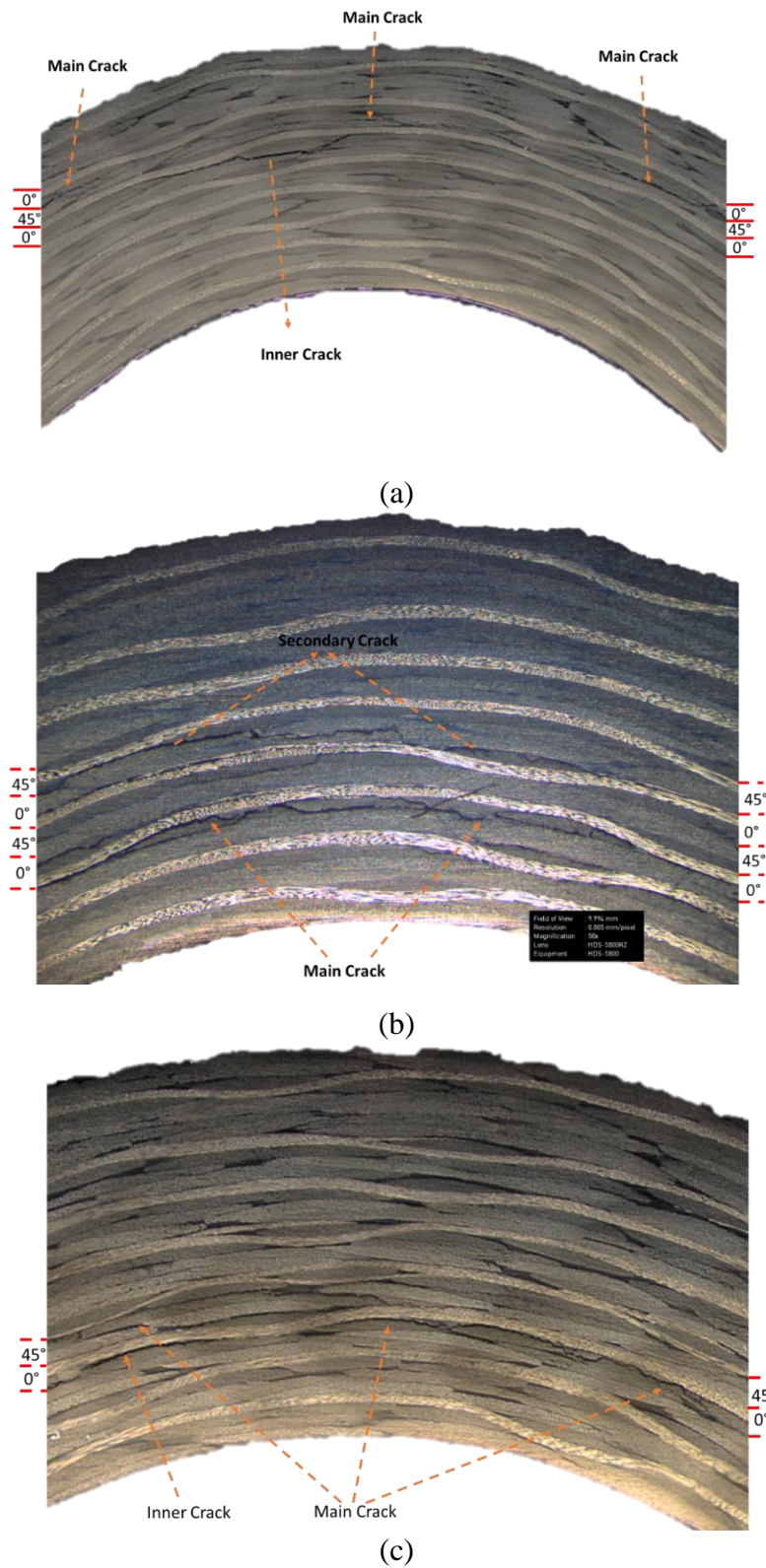
Figure 5.8. Micrographs taken at 50x magnification from the curved region of specimens: (a) Fabric 1, (b) Fabric 2 and (c) Fabric 3.

Post-mortem micrographs taken from the curved region and the arms of specimen Fabric 1:

Over the curved region of the tested specimen Fabric 1, five inner matrix cracks are observed in the micrograph. The location of the matrix cracks is shown with red ellipses in Figure 5.9., and the detailed micrographs of these inner matrix cracks are given in Figure 5.10. Inner crack 1 and inner crack 2 are taken at 500x magnification while other cracks are taken at 200x magnification.

Figure 5.9. The location of the matrix crack which occurs in the curved region.

(1)

(2)

(3)

(4)

(5)

Figure 5.10. Detailed micrographs of the matrix cracks observed in the Fabric 1.

From where the cracks propagate through the curved region to the arms of the specimen Fabric 1, tiled micrographs are taken at 200x magnification. The close-up pictures taken from the tiled micrograph were used to show the propagation of the crack in more detail.

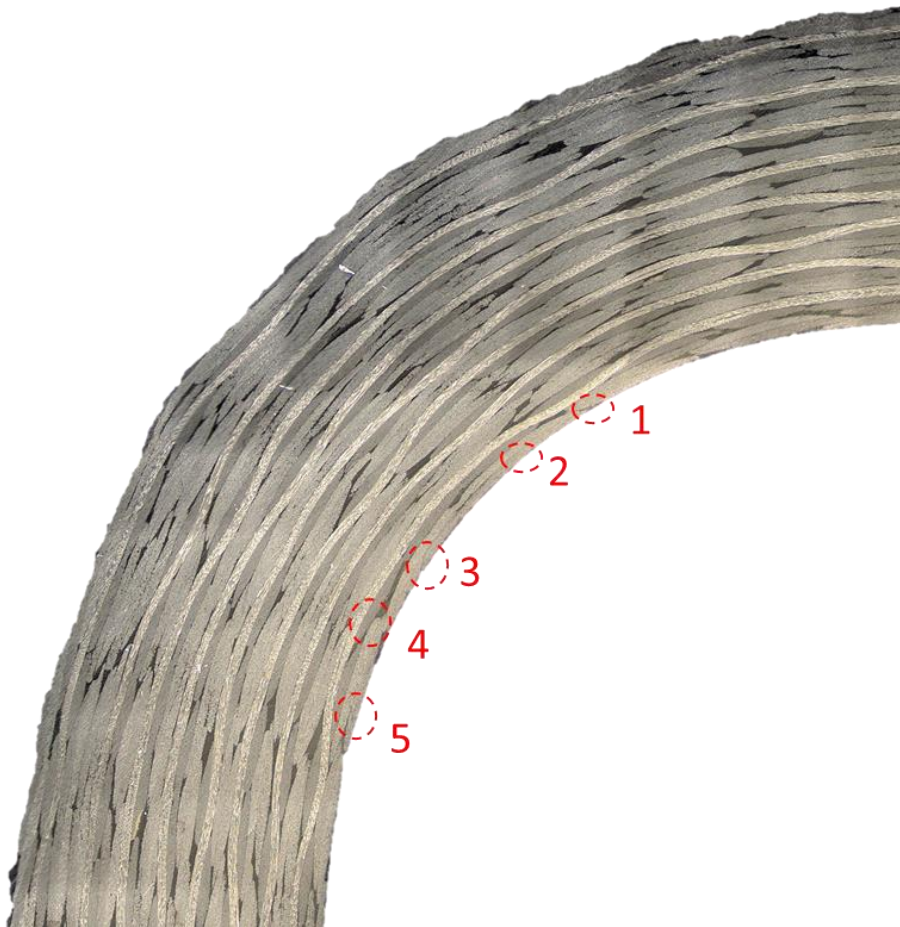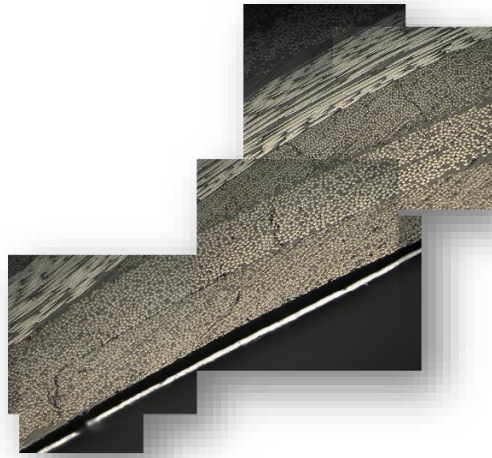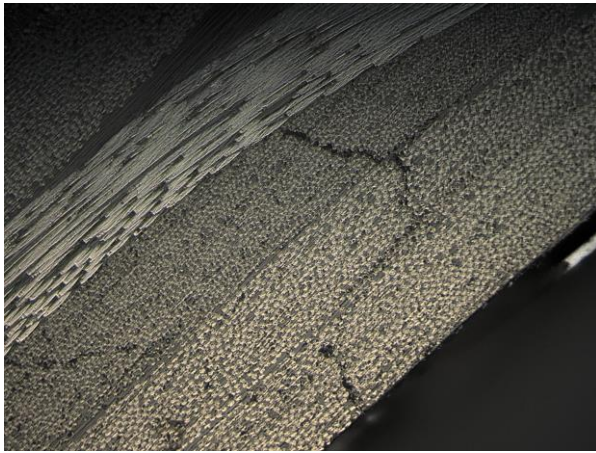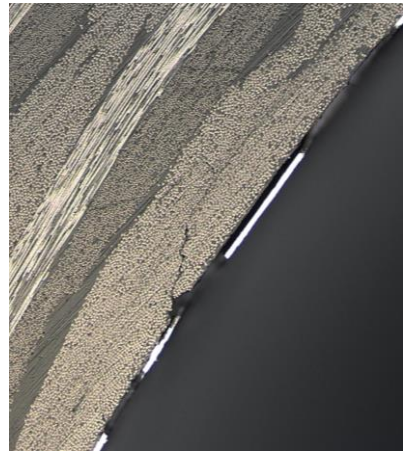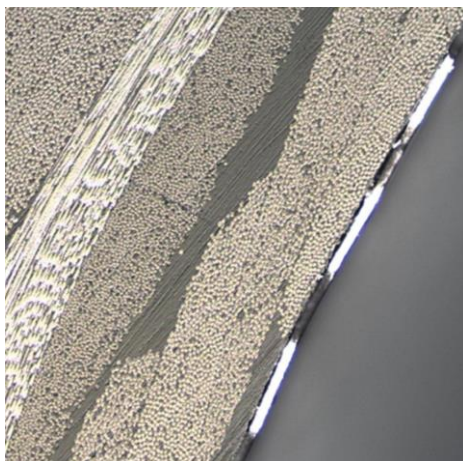Figure 5.11 contains the post-mortem micrograph of the curved region of the specimen Fabric 1 and two close-up pictures showing the propagation of the crack. In the close-up pictures, dashed red circles show the location of where the inner crack tip was arrested. Both close-up pictures also show the complex damage pattern which occurs in the fabric composite laminates: Matrix cracks in 45° ply, propagation of the crack in both interplay and intra-ply, crack bifurcation and resin crack. The close-up pictures of orange rectangular a and b shown in Figure 5.11 are given in Figure 5.12. In rectangular a, it is seen that cracks propagate through inter-ply 0/45, intra-ply +45/-45 and intar-ply 0/90 interfaces. Matrix and resin crack formation is observed when the crack reaches the intra-ply 0/90 interface. In rectangular b, the dashed white arrow represents the direction of propagation of the crack. It is seen that the crack propagates backward by following the harness.

Figure 5.13 contains the post-mortem micrograph of the vertical arm of the specimen Fabric 1 and two close-up pictures showing the propagation of the crack. In the top close-up picture, it is seen that the crack bifurcates along the three consecutive harnesses and surrounds them. In the bottom close-up picture, it is seen that crack penetrates into the warp having 0° fiber. Thus, it is arrested in the vertical arm without propagating further.

Figure 5.14 contains the post-mortem micrograph of the horizontal arm of the specimen Fabric 1 and the close-up picture showing the propagation of the crack. The crack propagates in the direction parallel to the warp having 0° fiber. First, the crack propagates through the inter-ply 0/45 interface, then intra-ply 0/90 interface, and the crack growth stops on the intra-ply 0/90 interface.
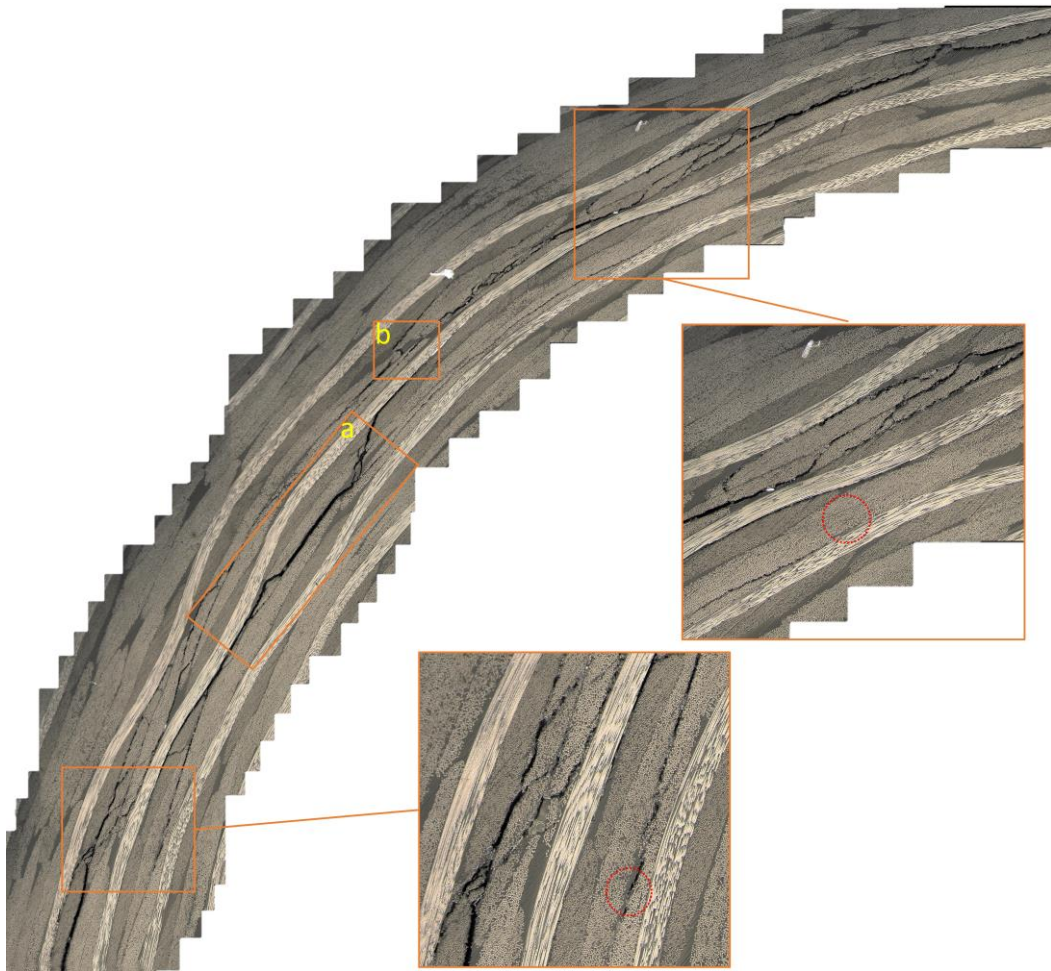
Figure 5.11. Post-mortem micrograph taken from the curved region of Fabric 1.

Intraply
0/90 Interface

Matrix & Resin
Cracks

Intraply
+45/-45 Interface

Interply
0/45 Interface

(a)   (b)

Figure 5.12. Close-up pictures of the curved region of Fabric 1.

Figure 5.13. Post-mortem micrograph taken from the vertical arm of Fabric 1.
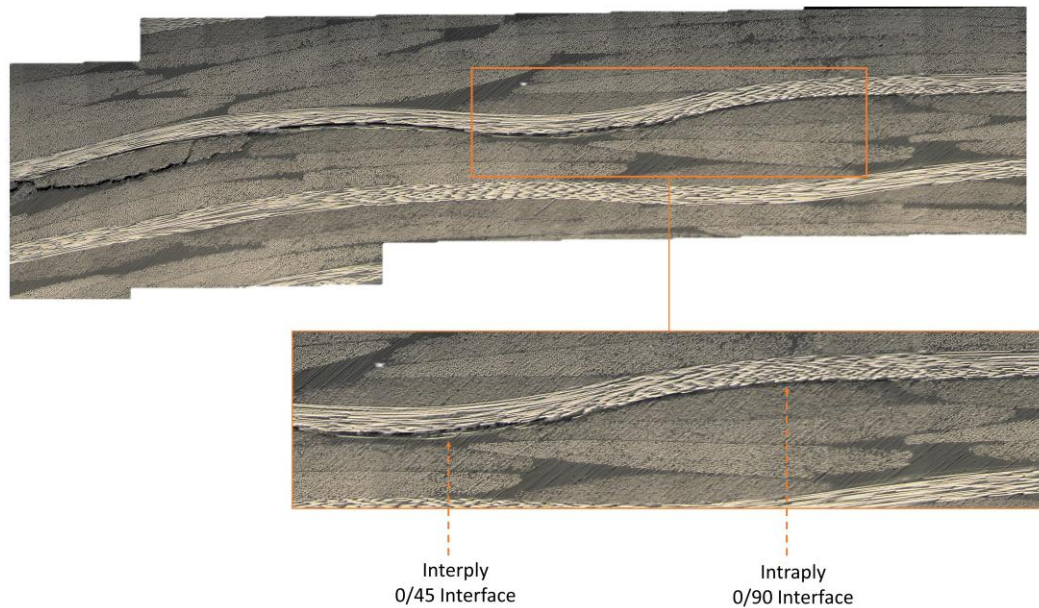
Figure 5.14. Post-mortem micrograph taken from the horizontal arm of Fabric 1.

Post-mortem micrographs taken from the curved region and the arms of specimen Fabric 3:

From the curved region and the arms of the specimen Fabric 3, post-mortem micrographs were taken at 90x magnification. Then these micrographs were tiled manually. The post-mortem micrographs taken at 200x magnification were used as close-up pictures to show the propagation of the crack in detail.

Figure 5.15 contains the post-mortem micrograph of the curved region of the specimen Fabric 3 and two close-up pictures showing the propagation of the crack. At the close-up picture taken from the region near the vertical arm, it is seen that the crack propagates through the inter-ply interface. When it comes to the beginning of the 45° harness, it jumps to the resin-rich region and propagates through there. Then it comes to the beginning of the 90° harness, and it bifurcates. The red dashed circle shows the location of where the crack propagating through the 6th ply arrests. In the other close-up picture, which shows the propagation of the crack in the middle of the curved region, it is seen that the crack propagates inside the 90° harnesses rather than the interfaces.
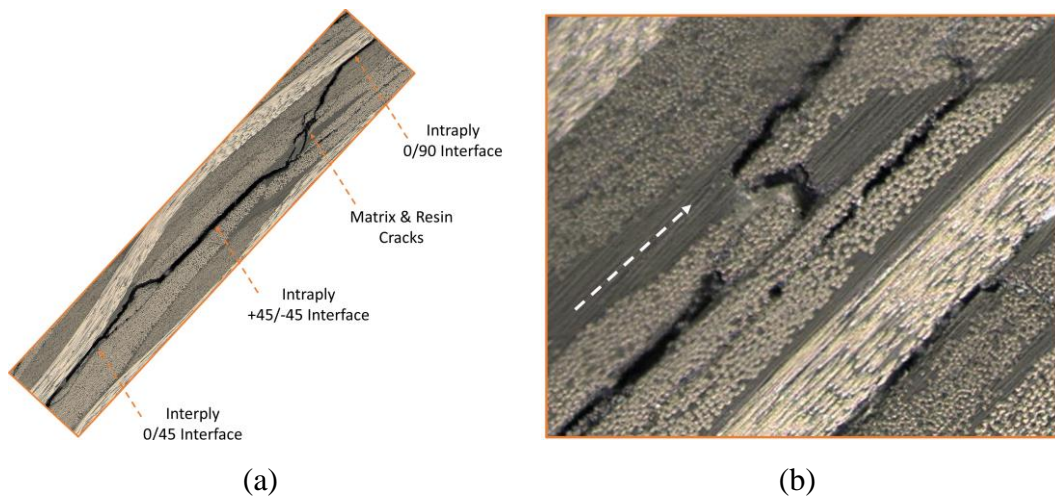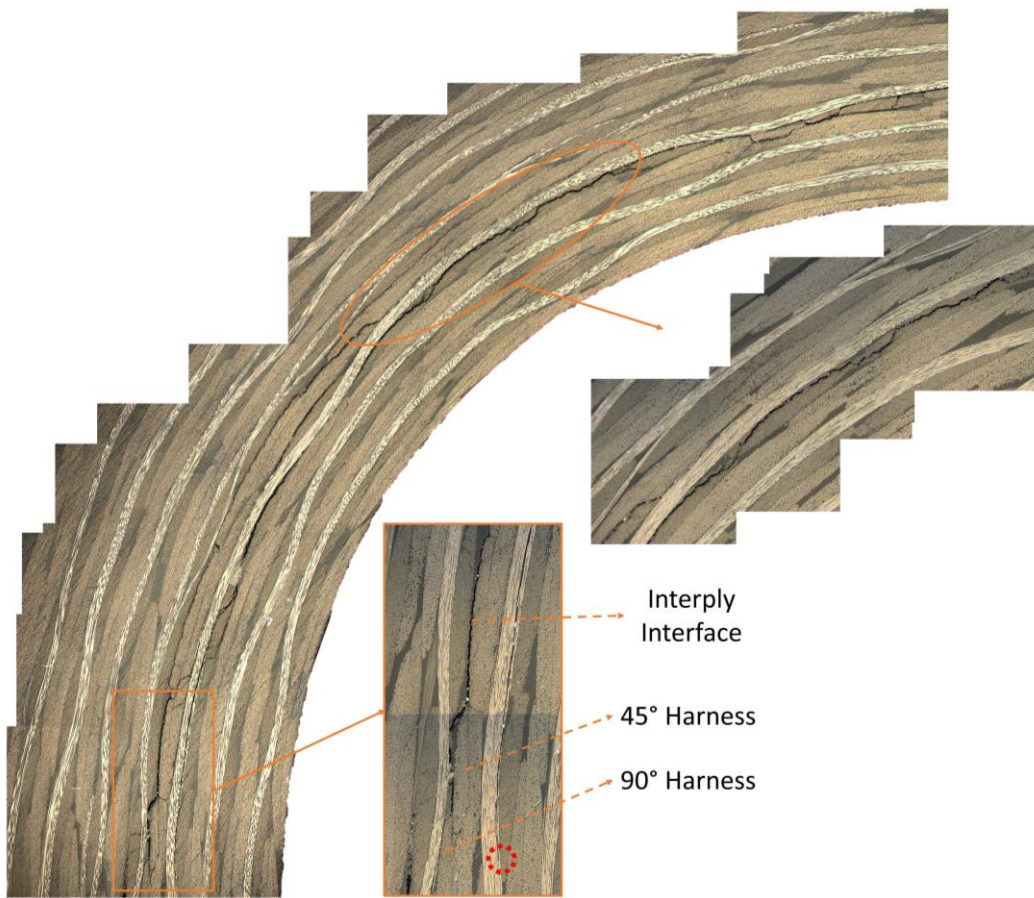
Figure 5.15. Post-mortem micrograph taken from the curved region of Fabric 3.

Figure 5.16 contains the post-mortem micrograph of the vertical arm of the specimen Fabric 3 and five close-up pictures showing the propagation of the crack. Two of them were taken at 500x magnification. In the first orange rectangular, it is seen that the crack propagates through the resin rich region and leads to resin debris formation. In the second orange rectangular, it is seen that the crack propagates through the interface between the resin rich region and the harness. In the third orange dashed rectangular frame, the penetration of the crack into the warp having 0° fibers is seen. The crack, however, does not arrest into 0° fibers and propagates at the left-hand side of that warp, as shown in the fourth orange rectangular.

Figure 5.17 contains the post-mortem micrograph of the horizontal arm of the specimen Fabric 3 and two close-up pictures showing the propagation of the crack. At the bottom close-up picture, it is seen that the crack bifurcates at the beginning of
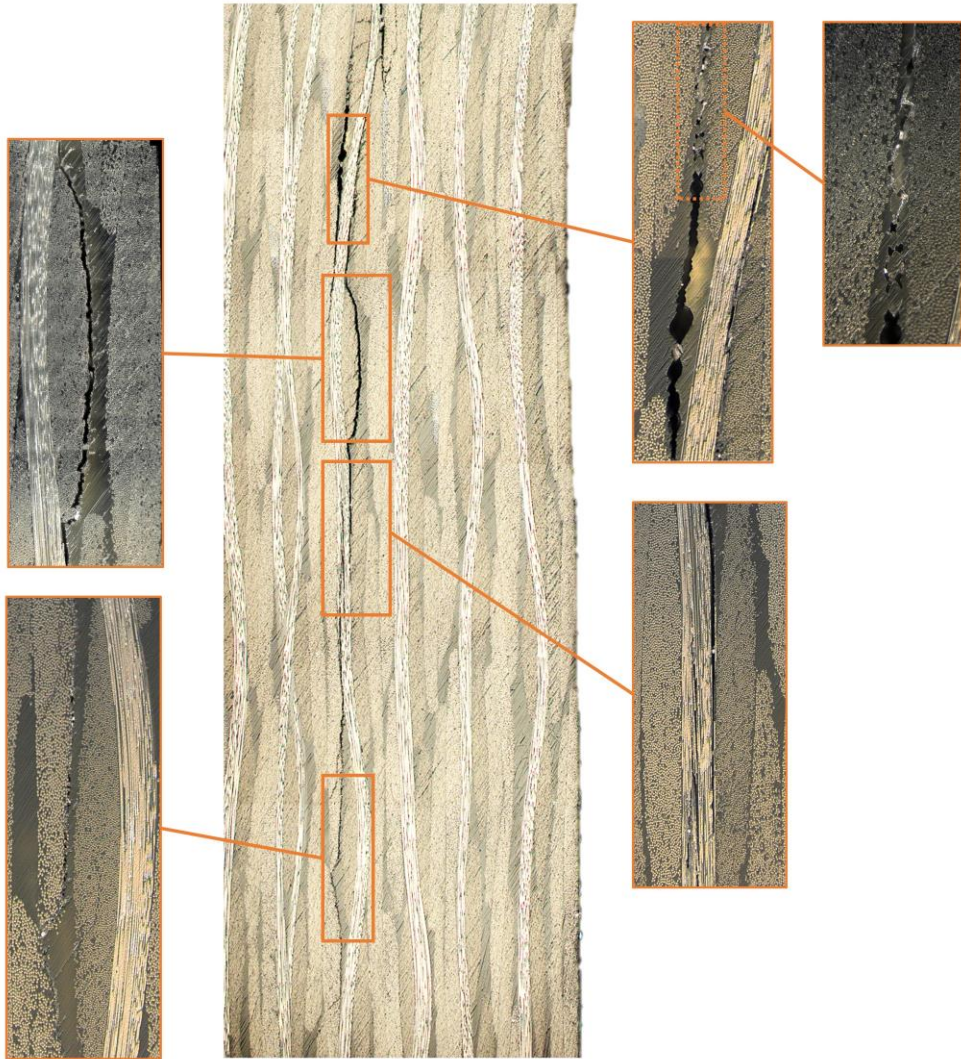
Figure 5.16. Post-mortem micrograph taken from the vertical arm of Fabric 3.

the horizontal arm and propagates by surrounding the harness. Matrix crack occurs inside that harness, too. At the end of the harness, the cracks coalesce and propagate through the intra-ply 0/90 interface. Then the crack bifurcates once again. As it is observed in the specimen Fabric 1, the growth of the crack stops after it penetrates into the warp having 0° fibers, as shown in the top close-up picture.

Figure 5.18 contains the post-mortem micrograph of the curved region taken from the back surface of the specimen Fabric 3 and the close-up picture showing the propagation of the crack. In the close-up picture, it is seen that crack propagates
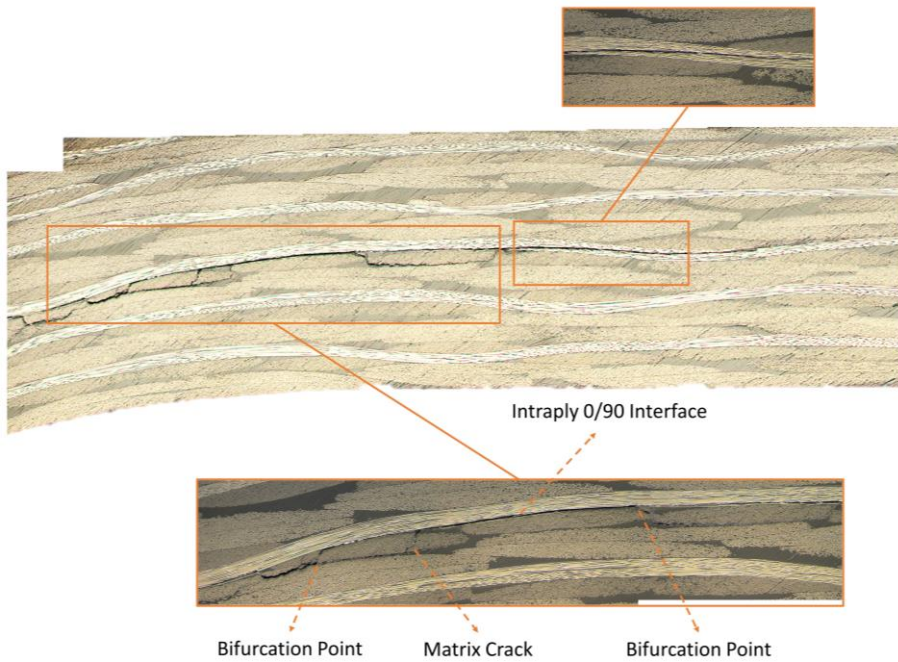
Figure 5.17. Post-mortem micrograph taken from the horizontal arm of Fabric 3.

through the intra-ply +45/-45 interface. When it comes to the end of the harness, it propagates backward by surrounding the harness. It jumps to the intra-ply 0/90 interface by causing to resin and matrix cracking.
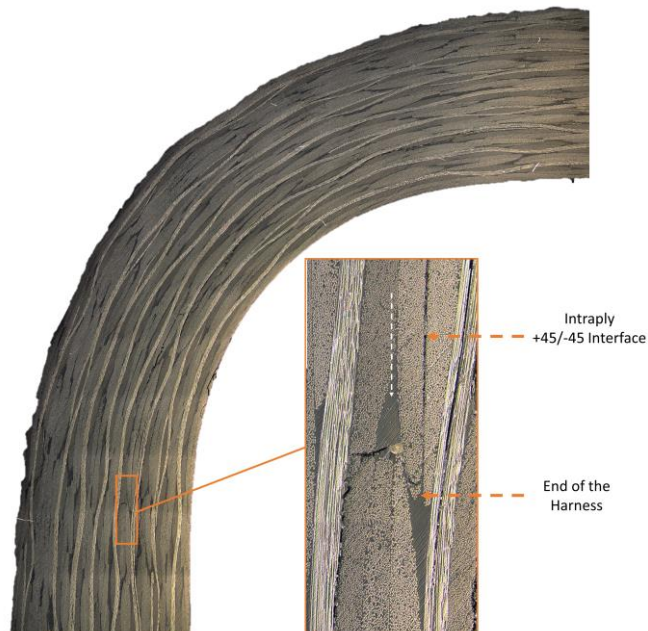

Figure 5.18. Post-mortem micrograph taken from the curved region of back surface of Fabric 3.

5.2   Elastic Finite Element Analysis Results

After the experimental observations are done, the stress field over the curved beam is obtained from finite element analysis (FEA) to elucidate failure mechanism of the fabric curved composite laminates. Tangential direction of the curved region is again defined by θ as shown in Figure 4.15.

The stress distribution over the curved beam obtained at the average failure displacement of experiments Fabric 2 and Fabric 3, 17.5 mm, is given in Figure 5.19. Tangential stress is tensile in the inner region while it is compressive in the outer region due to the bending moment, leads to an increase in the curved angle. Maximum tangential tensile stress in 0° plies occurs at a section of θ=73° as 466.3 MPa while that in 45° plies occurs at a section of θ=79° as 346.72 MPa. Radial stress is approximately zero at the arms and all over the inner and outer radii of the curved beam. Maximum radial stress is 43.45 MPa and occurs at a section of θ=63° in the interface between the 7th and 8th plies. As for the shear stress, four spot points are observed at the transition region from the curve region to the arms. Maximum positive shear stress occurs at the upper red spot point as 16. 55 MPa while minimum shear stress occurs at the lower blue spot point as -15.51 MPa. As it is mentioned in the post-mortem micrograph analysis of the specimen Fabric 2 and Fabric 3, the crack is initiated in the 6th and 7th plies where the radial stress is found to be high by FEM also. The failure of the fabric specimens might be related to the higher radial stresses.
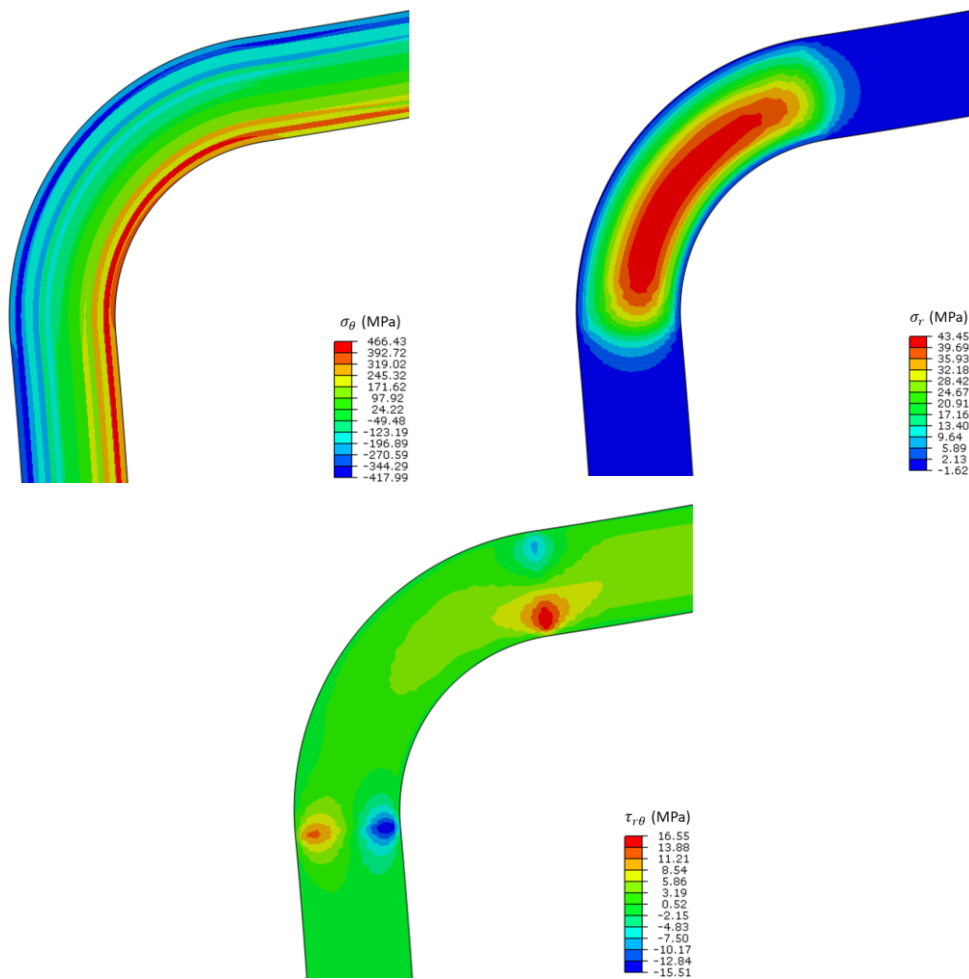
Figure 5.19. Stress field obtained for the fabric curved composite laminates:
(a) Tangential Stress (b) Radial Stress (c) Shear Stress.

The through-the-thickness stress distribution at the section of θ=45° is taken from the finite element analysis and compared with analytic solution as shown in Figure 5.20. For tangential stresses, both FEA and analytic solution gives approximately same result. However, there is a large discrepancy between the analytic and finite element results. Tangential stress again decreases from inner region to the outer region linearly at the plies having same orientation. As for the radial stress, analytic solution give close results to the finite element analyses. The trend of the- through-thickness radial stress is similar with that observed in the cross-ply laminates, and radial stress at the 7th, 8th, and 9th plies are approximately same. As for the shear stress, analytic solution and FE model with analytic BC gives close results. The error

is less than 6 %. The error between the analytic solution and FE model with experimental BC, however, is at a level that is beyond acceptable and is approximately 20 %.
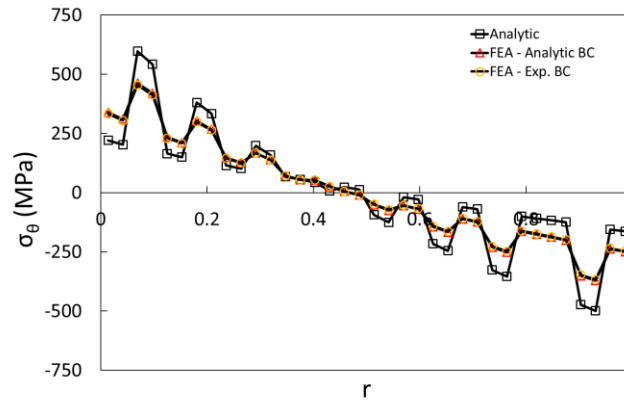
(a)
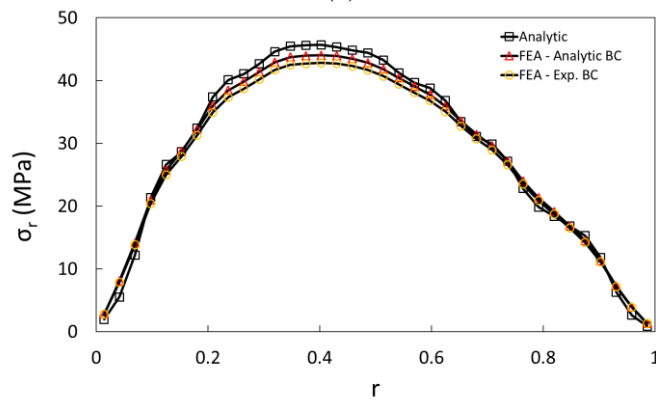
(b)

(c)

Figure 5.20. Through-the-thickness stress distribution at the section of θ=45° for fabric specimens: (a) Tangential Stress (b) Radial Stress (c) Shear Stress.

Analytic solution and FE model with analytic boundary conditions generally could give close results. However, as shown in Figure 5.20, the error between their results is so high. This is because the analytic solution is derived for plane stress case while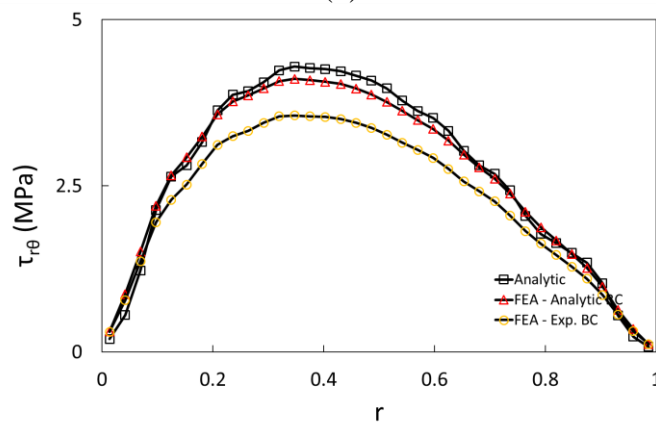 the finite element analyses are conducted with plane strain element. Thus, finite element analyses are also conducted with plane stress element. The results of these finite element analyses are compared with analytic solution, and it was seen that the result of the analytic solution and FE model with analytic boundary conditions are close to each other. These results can be found in the APPENDIX D.

5.3   Discussion

Unlike the crack tip speed history observed in cross-ply curved composite laminates, the speed of the crack tip in the fabric curved composite laminates fluctuates. The weave style of the fabric materials leads to these fluctuations of a crack tip speed. In Figure 5.21, the propagation of the crack tip through plain weave fabric laminates is shown. The fills, which are perpendicular to the direction of the propagation, impede the propagation like a crack arrester while the warps, which are parallel to the direction of the propagation, advance the propagation. The crack jump occurs at sudden load drops, and cracks arrest in the crossing region of warp and fill [39][40]. This mechanism leads crack tips to speed up and slow down.
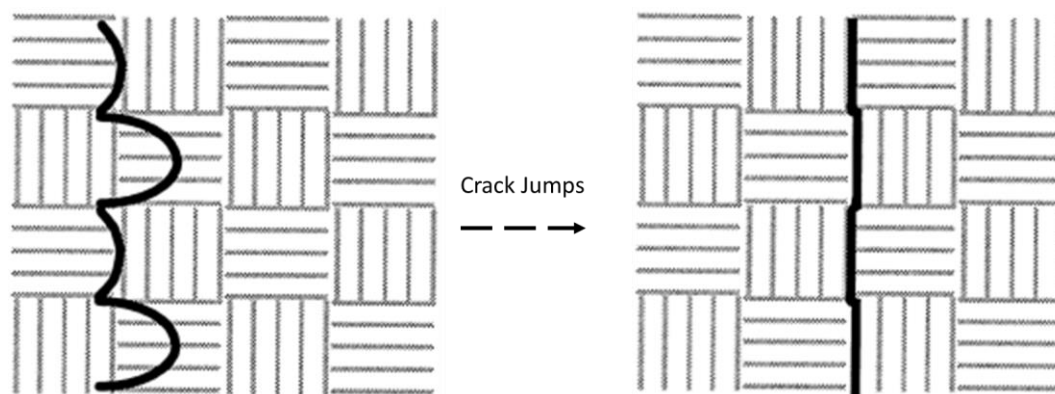
Figure 5.21. The effect of the weave pattern on the crack propagation and crack jumps occurs at a sudden load drop.

In the detailed fractography of fabric curved composite laminates, it is mentioned that the crack bifurcations and backward crack propagation occur. The reason of the bifurcations in UD laminates are attributed to the fiber orientation transverse to the crack propagation [41]. Observations made throughout this study are consistent with that statement. The main reason for bifurcations to be observed in the fabric curved composite laminate usually occur when the crack comes to the 90° fills, which lie in the perpendicular direction to the crack propagation. Figure 5.22 shows the formation of the crack bifurcation in woven glass composite. According to Figure 5.22b, the formation of the crack bifurcation results in the crack which propagated backward. Backward propagation of the crack observed in the specimens Fabric 1 and Fabric 3 is attributed to the formation of the bifurcation.

Figure 5.22. Two different ways of the formation of crack bifurcation [42].

CHAPTER 6

SUMMARY

In this thesis, failure mechanism of cross-ply and fabric curved composite laminates are investigated experimentally. The investigation is supported by both finite element and analytic method. In chapter 1, the importance of the composite material on the aerospace and wind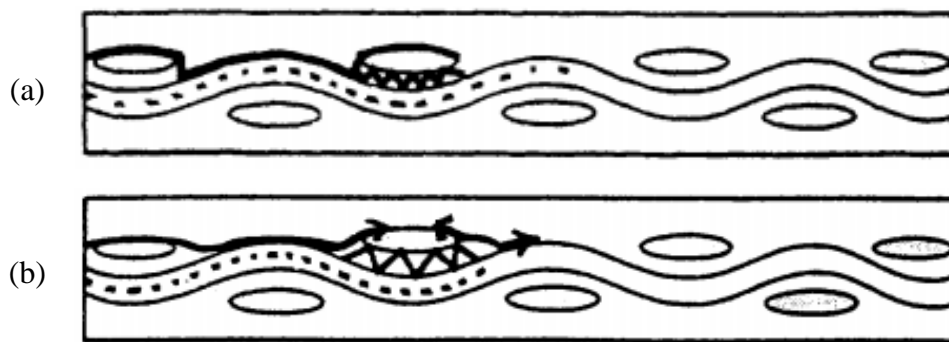 power industry is addresses. Then it is mentioned that the curved composite parts, used in primary load-carrying structures in aerospace and wind power industry, is prone to delamination failure mode. In chapter 2, a body of literature related to experimental and numerical study of the curved composite laminates is reviewed. In chapter 3, the experimental, numerical and analytical method used in the present study are explained in detail. The experiments are conducted with curved composite laminates having a stacking sequence of cross-ply $[(0/90)_4, \overline{90}]_s$ and fabric $[(45/0)_7, 45/45/0/45]_s$. The propagation of the dynamic failure in the curved composite laminates is captured with high-speed camera at 420k fps. Digital image correlation method is used to obtain in-situ strain field over the curved region in two experiments conducted with cross-ply composite laminates. Finite element analysis is carried out to obtain the stress and strain field over the curved beam. To elucidate the failure mechanism observed in the cross-ply laminates, 2D Hashin failure criteria is used. In the analytic method, stress field solution proposed by Ko and Jackson [32], Timoshenko [33] and Lekhnitskii [34], is explained in detail. In chapter 4, the experimental and finite element result of cross-ply curved composite laminates are presented. In three experiments, multiple load drops occur, and these load drops correspond to the one or two delaminations. On the other hand, in other experiments, one load drop where four or five delamination occurs sequentially are observed. The crack tip speed reaches its maximum at 1656 m/s which is slightly higher than Rayleigh wave speed. The change of the von Mises strain field, which is obtained from the digital image

correlation method, is presented with increasing loading. Through-the-thickness von Mises strain distribution is calculated, which is in good agreement with that obtained from finite element analysis. In-the post-mortem micrographs, fiber breakage is observed at the specimen in which the multiple delaminations occur during one load drop. Radial matrix crack and meandering crack path is also observed, and the reason of the meandering crack path is investigated. In chapter 5, the experimental and finite element results of fabric curved composite laminates are presented. High-speed camera observation shows that the crack initiates at the through-the-thickness region corresponding to the 6th and 7th plies. Intersonic crack tip speed which exceeds the material shear wave speed is observed, and the crack tip speed fluctuates during its travel. In the post-mortem micrographs, complex failure pattern, which consists of crack propagation through inter-ply & intra-ply interfaces and crack bifurcations around the harness, is observed. The stress distribution taken from the finite element analysis shows that crack initiates at which the radial stresses is dominant. Complex failure pattern observed in the post-mortem micrographs is attributed to the weave style of fabric composite laminates.

CHAPTER 7

CONCLUSION

In order to study failure of the cross-ply and fabric curved composite laminates, an in-house designed test fixture is used to conduct experiments. The propagation of dynamic delamination is recorded using high-speed camera, and crack tip position and speed history are calculated and plotted against time. In-situ strain field is obtained by using digital image correlation method in two experiments of cross-ply curved composite laminates. Detailed fractography of the specimens is provided and failure pattern of the specimens is examined. Finite element analysis is also carried out to obtain the stress field over the curved region to elucidate failure observed in the specimen. For the cross-ply curved composite laminates, progressive 2D Hashin failure criteria is used to model failure pattern observed in the post-mortem micrographs. Conclusions made from the experiment results are as follows:

- In the cross-ply laminates, crack tip speed reaches its maximum at 1676 m/s which is lower than the material shear wave speed while in fabric laminates, crack tip reaches intersonic speed of 2173 m/s.
- Unlike the crack tip speed observed in cross-ply laminates, the crack tip speed fluctuates in fabric laminates.
- In cross-ply laminates, crack reaches the upper inter-ply (interlaminar) interface and propagates through the arms while in the fabric laminate, crack propagates through the inter-ply & intra-ply interfaces and resin rich regions during its travel.
- Residual stress should be accounted to predict the meandering crack path.
- Crack tip speeds in the cross-ply laminates can be used to validate the interface parameters in finite element analysis simulating the delamination with cohesive zone modelling in conjunction with the Hashin failure criteria.

REFERENCES

[1]   Mallick, P. K. (2007). Fiber-reinforced composites: materials, manufacturing, and design. CRC press

[2]   Goodship, V. D., Middleton, B., & Cherrington, R. (2015). Design and manufacture of plastic components for multifunctionality: structural composites, injection molding, and 3D printing. William Andrew.

[3]   Rajak, D. K., Pagar, D. D., Menezes, P. L., & Linul, E. (2019). Fiber-reinforced polymer composites: Manufacturing, properties, and applications. Polymers, 11(10), 1667.

[4]   Hansen, J. Z., & Østergaard, R. (2013). The effects of fibre architecture on fatigue life-time of composite materials. DTU Wind Energy.

[5]   Wegst, U. G., Bai, H., Saiz, E., Tomsia, A. P., & Ritchie, R. O. (2015). Bioinspired structural materials. Nature materials, 14(1), 23-36.

[6]   Wisnom, M. R. (2012). The role of delamination in failure of fibre-reinforced composites. Philosophical Transactions of the Royal Society A: Mathematical, Physical and Engineering Sciences, 370(1965), 1850-1870.

[7]   Clyne, T. W., & Hull, D. (2019). An introduction to composite materials. Cambridge university press.

[8]   Matthews, F. L., & Rawlings, R. D. (1999). Composite materials: engineering and science. Elsevier.

[9]   Cao, Y., Cao, Z., Zhao, Y., Zuo, D., & Tay, T. E. (2020). Damage progression and failure of single-lap thin-ply laminated composite bolted joints under quasi-static loading. International Journal of Mechanical Sciences, 170, 105360.

[10]   Hu, Q., Zhang, Y., Mao, Y., Memon, H., Qiu, Y., Wei, Y., & Liu, W. (2019). A comparative study on interlaminar properties of l-shaped two-dimensional (2d) and three-dimensional (3d) woven composites. Applied Composite Materials, 26(3), 723-744.

[11] Chang, F. K., & Springer, G. S. (1986). The strengths of fiber reinforced composite bends. Journal of composite materials, 20(1), 30-45.

[12] Sun, C. T., & Kelly, S. R. (1988). Failure in composite angle structures part I: Initial failure. Journal of reinforced plastics and composites, 7(3), 220-232.

[13] Sun, C. T., & Kelly, S. R. (1988). Failure in composite angle structures Part II: Onset of delamination. Journal of reinforced plastics and composites, 7(3), 233-244.

[14] Martin, R. H. (1992). Delamination failure in a unidirectional curved composite laminate. In Composite Materials: Testing and Design (Tenth Volume). ASTM International.

[15] Martin, R. H., & Jackson, W. C. (1993). Damage prediction in cross-plied curved composite laminates. In Composite Materials: Fatigue and Fracture, Fourth Volume. ASTM International.

[16] Feih, S., & Shercliff, H. R. (2005). Composite failure prediction of single-L joint structures under bending. Composites Part A: Applied Science and Manufacturing, 36(3), 381-395.

[17] Wimmer, G., Kitzmüller, W., Pinter, G., Wettemann, T., & Pettermann, H. E. (2009). Computational and experimental investigation of delamination in L-shaped laminated composite components. Engineering Fracture Mechanics, 76(18), 2810-2820.

[18] Gozluklu, B. & Coker, D. (2012). Modeling of the dynamic delamination of L-shaped unidirectional laminated composites. Composite Structures, 94, 1430–1442.

[19] Gozluklu, B., Uyar, I., & Coker, D. (2015). Intersonic delamination in curved thick composite laminates under quasi-static loading. Mechanics of Materials, 80, 163-182.

[20] Tasdemir, B., & Coker, D. (2019). Comparison of damage mechanisms in curved composite laminates under static and fatigue loading. Composite Structures, 213, 190-203.

[21] Hexcel Corporation, 2016. HexPly 8552 Prod. Data Sheet, pp. 1–6.

[22]   Hexcel Corporation, 2016. HexTow AS4 Prod. Data Sheet, pp. 1–2.

[23]   Clarkson, E. Hexcel 8552 AS4 Unidirectional Prepreg Qualification Statistical Analysis Report.

[24]   Marlett, K., Ng, Y., & Tomblin, J. (2011). Hexcel 8552S AS4 plain weave fabric prepreg 193 gsm & 38% RC qualification material property data report. National Institute for Aviation Research, Wichita State University, CAM-RP-20110-006 April, 14.

[25]   Coker, D., & Rosakis, A. J. (2001). Experimental observations of intersonic crack growth in asymmetrically loaded unidirectional composite plates. Philosophical Magazine A, 81(3), 571-595.

[26]   Jones, R. M. (1998). Mechanics of composite materials. CRC press.

[27]   Ravi-Chandar, K. (2004). Dynamic fracture. Elsevier.

[28]   Uyar, İ. (2014). Experimental investigation of dynamic delamination in curved composite laminates (Master's thesis, Middle East Technical University).

[29]   Nettles, A. T. (1994). Basic mechanics of laminated composite plates.

[30]   Blaber, J., Adair, B., & Antoniou, A. (2015). Ncorr: open-source 2D digital image correlation matlab software. Experimental Mechanics, 55(6), 1105-1122.

[31]   ABAQUS (2019). Abaqus Analysis Guide. Dassault Systèmes, Providence, RI, USA.

[32]   Ko, W. L., & Jackson, R. H. (1989). Multilayer theory for delamination analysis of a composite curved bar subjected to end forces and end moments. In Composite Structures 5 (pp. 173-198). Springer, Dordrecht.

[33]   Timoshenko, S., & Goodier, J. N. (1970). Theory of elasticity: New York. London,: Ed Mc Graw-Hill.

[34]   Lekhnitskii, S. G. (1968). Anisotropic plates. Foreign Technology Div Wright-Patterson Afb Oh.

[35]   Sloot, J. H. Through-The-Thickness Stresses And Failure In The Corner Radius Of A Laminated Composite Section. ESDU Data Item, 94019.

[36] Fleck, N. A., Hutchinson, J. W., & Zhigang, S. (1991). Crack path selection in a brittle adhesive layer. International Journal of Solids and Structures, 27(13), 1683-1703.

[37] Lu, T. J., Xia, Z. C., & Hutchinson, J. W. (1994). Delamination of beams under transverse shear and bending. Materials Science and Engineering: A, 188(1-2), 103-112.

[38] Fu, C., & Wang, X. (2020). Micro-mechanical analysis of matrix crack-induced delamination in cross-ply laminates in tension. Composite Structures, 243, 112202.

[39] Saleh, M. N., Wang, Y., Yudhanto, A., Joesbury, A., Potluri, P., Lubineau, G., & Soutis, C. (2017). Investigating the potential of using off-Axis 3D woven composites in composite joints' applications. Applied Composite Materials, 24(2), 377-396.

[40] Kim, J. K., & Sham, M. L. (2000). Impact and delamination failure of woven-fabric composites. Composites Science and Technology, 60(5), 745-761.

[41] Lucas, J. P. (1992). Delamination fracture: effect of fiber orientation on fracture of a continuous fiber composite laminate. Engineering fracture mechanics, 42(3), 543-561.

[42] Ebeling, T., Hiltner, A., Baer, E., Fraser, I. M., & Orton, M. L. (1997). Delamination failure of a woven glass fiber composite. Journal of composite materials, 31(13), 1318-1333.

A. Validation of Matlab Code for The Analytic Stress Solution of Multilayer Curved Composite Laminates with Finite Element Results

Stress distribution obtained from the MATLAB Code is compared with that finite element stress distribution. Material properties is given in the table below. Inner radius is taken as 5 mm, and stacking sequence is chosen as $[-45/0/45/90/90/0/90/45/0/-45]$. Outer radius corresponding to this stacking sequence is 6.27 mm. Only the curved region is modelled in finite element analysis. In end shear and normal load case, one end of the curve region is clamped and other end is loaded. For pure bending moment case, bending moment is applied to each end.

Material Properties:

E_{11} (GPa)	$E_{22}=E_{33}$ (GPa)	$v_{12}=v_{13}$	v_{23}	$G_{12}=G_{13}$ (GPa)	G_{23} (GPa)	t_p (mm)
154	8.5	0.35	0.487	5.3	4.2	0.127

Comparison of the analytic soltion with finite element results pure bending moment case, end shear load case and end normal load case are given in Figure A.1, Figure A.2, Figure A.3, respectively.

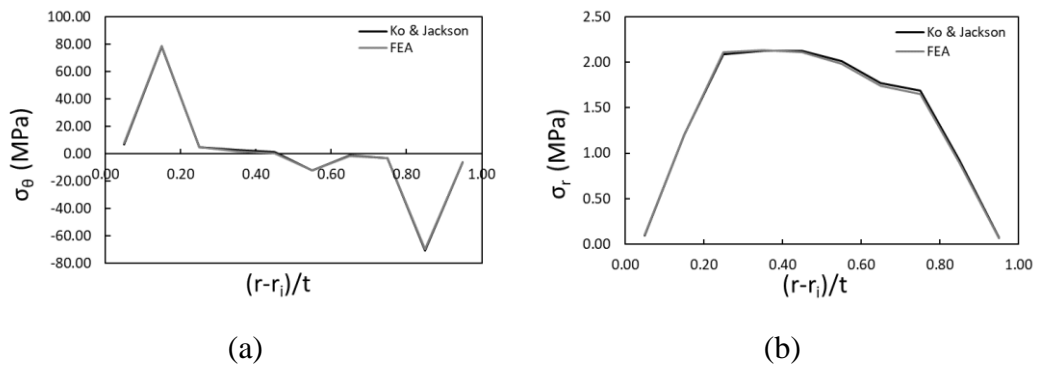(a)   (b)

Figure A.1. Comparison of the analytic solution with finite element results for pure bending case: (a) tangential stress, (b) radial stress.
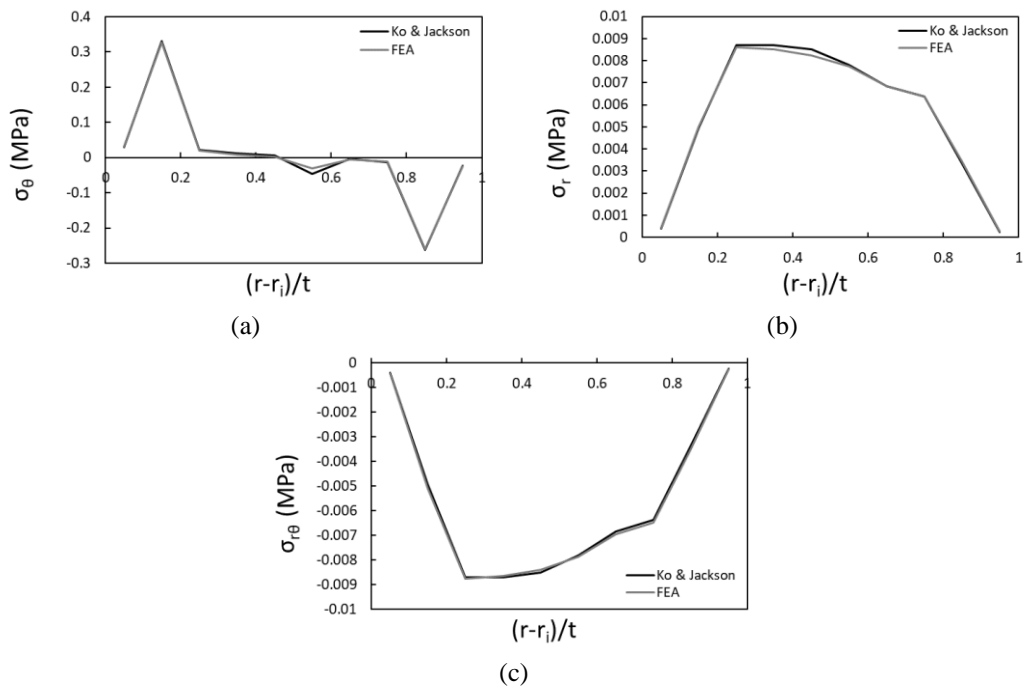
Figure A.2. Comparison of the analytic solution with finite element results for end shear load case: (a) tangential stress, (b) radial stress, (c) shear stress.
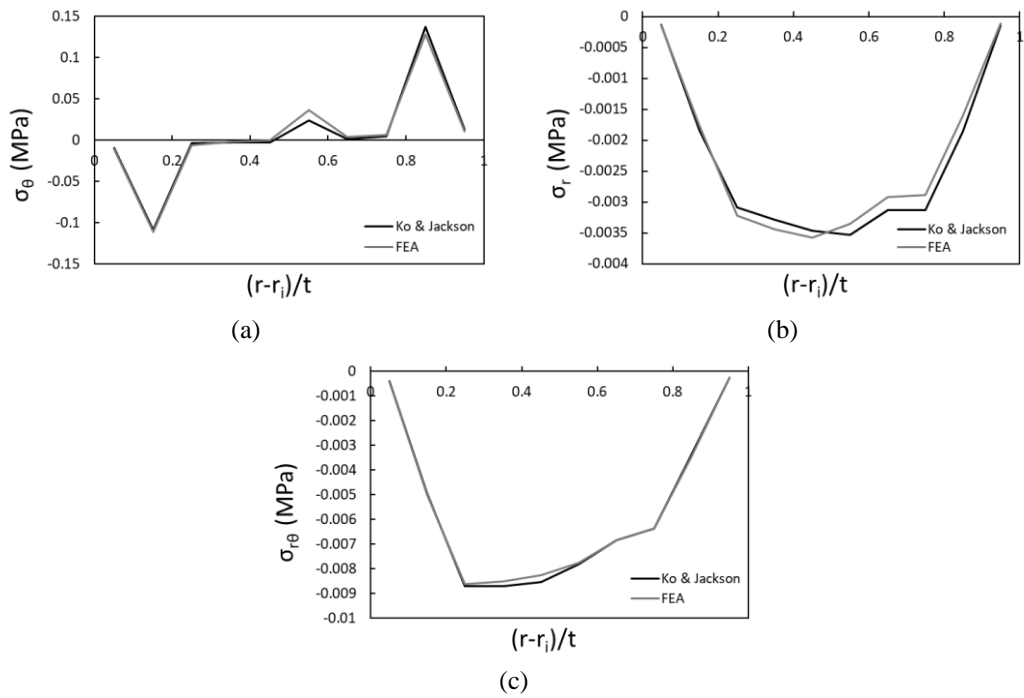

Figure A.3. Comparison of the analytic solution with finite element results for end normal load case: (a) tangential stress, (b) radial stress, (c) shear stress.

B. Original Micrograph of Cross-ply Specimen

Figure B. 1. Original micrograph of cross-ply specimen

C. Comparison of The Stress Distribution for The Plain Stress and Strain Case for Cross-ply Laminate
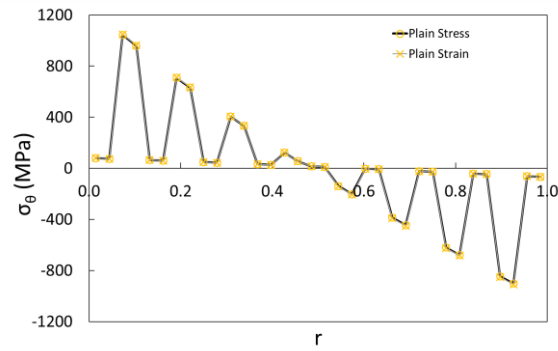
Figure C. 1. Tangential stress distribution for plane stress and plain case in cross-ply specimen
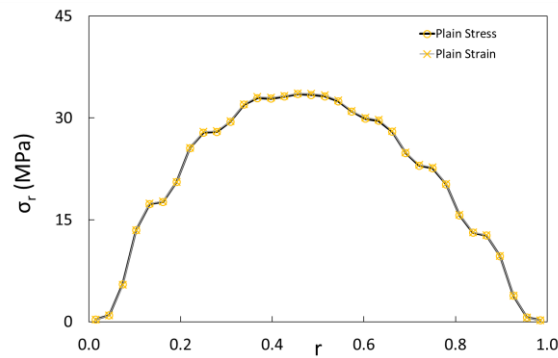

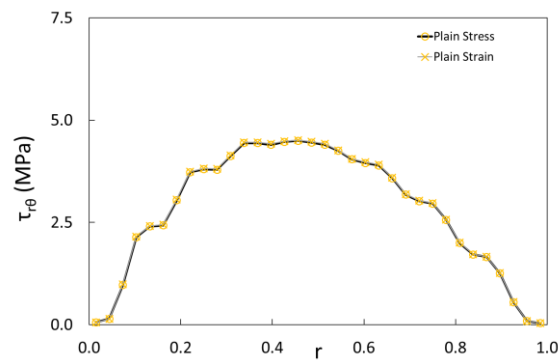Figure C. 2. Radial stress distribution for plane stress and plain case in cross-ply specimen

Figure C. 3. Shear stress distribution for plane stress and plain case in cross-ply specimen

D. Comparison of The Analytic Solution with The Finite Element Analysis Results for The Plain Stress Case
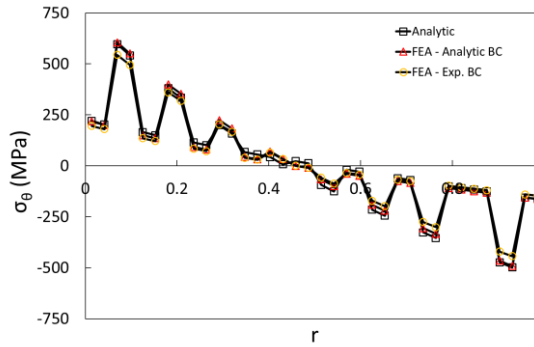

Figure D. 1. Tangential stress distribution obtained from analytic solution and finite element results for plane stress case
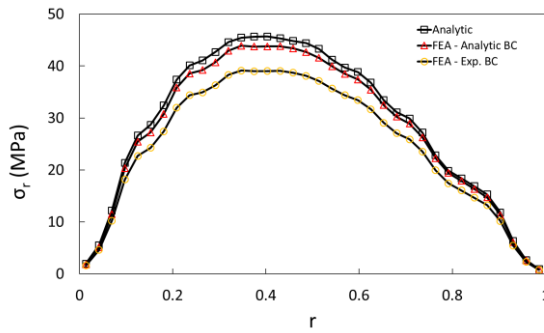

Figure D. 2. Radial stress distribution obtained from analytic solution and finite element results for plane stress case
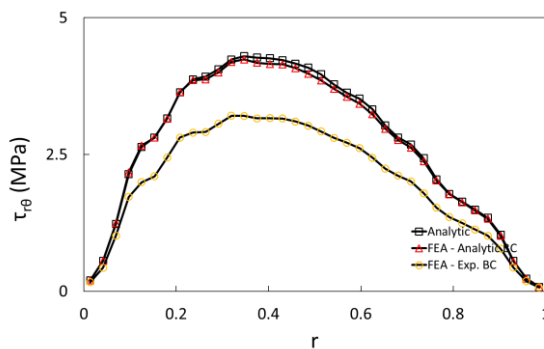

Figure D. 3. Shear stress distribution obtained from analytic solution and finite element results for plane stress case